NATIONAL TECHNICAL UNIVERSITY OF ATHENS

DIPLOMA THESIS

Nonlinear Rotordynamic Design of Turbine-Generator Shaft Trains Applying Numerical Continuation

---

Author:
Ioannis Gavalas

Supervisor:
Athanasios Chasalevris

A thesis submitted in fulfillment of the requirements
for the degree of Diploma in Mechanical Engineering

February 22, 2022

Declaration of Authorship

I, Ioannis Gavalas, declare that this thesis titled, "Nonlinear Rotordynamic Design of Turbine-Generator Shaft Trains Applying Numerical Continuation" and the work presented in it are my own. I confirm that:

- This work was done wholly or mainly while in candidature for a degree at this University.
- Where any part of this thesis has previously been submitted for a degree or any other qualification at this University or any other institution, this has been clearly stated.
- Where I have consulted the published work of others, this is always clearly attributed.
- Where I have quoted from the work of others, the source is always given. With the exception of such quotations, this thesis is entirely my own work.
- I have acknowledged all main sources of help.
- Where the thesis is based on work done by myself jointly with others, I have made clear exactly what was done by others and what I have contributed myself.

Signed: _____

Date: _____

"Each celestial body, in fact each and every atom, produces a particular sound on account of its movement, its rhythm or vibration. All these sounds and vibrations form a universal harmony in which each element, while having its own function and character, contributes to the whole"

Pythagoras (570 495 BC)

NATIONAL TECHNICAL UNIVERSITY OF ATHENS

Abstract

Faculty Name
School of Mechanical Engineering

Diploma in Mechanical Engineering

Nonlinear Rotordynamic Design of Turbine-Generator Shaft Trains Applying Numerical Continuation

by Ioannis Gavalas

The nonlinear dynamics of turbine generator shaft trains for power generation are investigated in this thesis. Realistic models of rotors, pedestals, and nonlinear bearings of partial arc and lemon bore configuration are implemented to compose a nonlinear set of differential equations for autonomous (balanced) and non-autonomous (unbalanced - per ISO) cases. The solution branches of the dynamic system are evaluated with the pseudo arc length continuation programmed by the author, and the respective limit cycles are evaluated by an orthogonal collocation method, and investigated on their stability properties and quality of motion for the respective key design parameters for the rotor dynamic design of such systems, namely: bearing profile and respective pad length, preload and offset, pedestal stiffness and elevation (misalignment), and rotor slenderness. Model order reduction is applied to the finite element rotor model and the reduced system is validated in terms of unbalance response and stability characteristics. The main conclusion of this thesis is that the system has the potential to develop instabilities in rotating speeds lower than the threshold speed of instability (evaluated by the linear approach) for specific unbalance magnitude and design properties. Unbalance response (with stable and unstable branches) is evaluated in severely reduced time compared to this applying time integration methods, enabling nonlinear rotor dynamic design of such systems as a standard procedure, and revealing the complete potential of motions (not only local).

Acknowledgements

This thesis is a result of 12 months of work in the Rotordynamics Group at the NTUA School of Mechanical Engineering. During this time I was supported and influenced by several people to whom I want to express my sincere thanks.

This work would not be possible without my supervisor, Asst. Prof. Athanasios Chasalevris. His insights, guidance and support in every step of this work has been invaluable. His mentoring made for an excellent basis for a future career in the field of Rotordynamics for which I am grateful.

I also want to extend my gratitude to the fellow students who also worked on their theses in the Rotordynamics Group for their contributions and quality discussions of technical and non-technical nature in the lab.

I am also grateful to my friends for their support and all the experiences we shared during those past twelve months which helped maintain balance and bring happiness during an otherwise pandemic-stricken and work-intensive period.

Last but certainly not least, I want to express my appreciation and gratitude to my parents for their continuing support and love and for their efforts to help me progress in all aspects of life. This work is dedicated to them as a small gift for their unwavering support during my studies and beyond.

Dedicated to my parents...

Contents

List of Figures

List of Tables

Nomenclature

Hellenic Letters

α	Bearing arc length
β	Bearing offset
δ	Logarithmic decrement
δ_i	Elevation of bearing i
λ	Eigenvalue
μ	Lubricant Dynamic Viscocity
μ_i	Floquet multipliers
ω	Natural frequency
Ω	Rotating speed
ω_d	Damped natural frequency
Ω_r	Rated operating speed
Φ	Monodromy matrix
ρ	Density
ρ_i	Density of material of shaft segment
θ_E	Bearing ending angle
θ_S	Bearing starting angle
$\boldsymbol{\phi}$	Eigenvector

Latin Letters

$\boldsymbol{A}_c$	Amplitude of cosine component of harmonic response
$\boldsymbol{A}_s$	Amplitude of sine component of harmonic response
$\boldsymbol{f}$	Force vector
$\boldsymbol{f}_i^B$	Unbalance forces
$\boldsymbol{f}_{r,i}^B$	Reduced bearing forces vector

$\boldsymbol{f}_{r,i}^{G}$ Reduced gravity force vector

$\boldsymbol{f}_{r,i}^{U}$ Reduced unbalance vector

$\boldsymbol{q}$ Degree of Freedom vector

$\boldsymbol{q}_r$ Reduced Degree of Freedom vector

$\boldsymbol{x}$ Unknown vector in 1st order ODE

$\boldsymbol{X}_c$ Amplitude of cosine component of harmonic excitation

$\boldsymbol{X}_s$ Amplitude of sine component of harmonic excitation

$\mathbf{C}$ Damping matrix

$\mathbf{C}_p$ Pedestal damping matrix

$\mathbf{C}_r$ Reduced damping matrix

$\mathbf{G}$ Gyroscopic matrix

$\mathbf{G}_p$ Pedestal gyroscopic matrix

$\mathbf{G}_r$ Reduced gyroscopic matrix

$\mathbf{K}_p$ Pedestal stiffness matrix

$\mathbf{K}_r$ Reduced stiffness matrix

$\mathbf{M}$ Mass matrix

$\mathbf{M}_p$ Pedestal mass matrix

$\mathbf{M}_r$ Reduced mass matrix

$A_{AM,i}$ Area of cross section of additional mass in segment

$A_{M,i}$ Area of cross section of shaft segment, considering mass

$A_{S,i}$ Area of cross section of shaft segment, considering stiffness

c_p Pad clearance

c_r Radial clearance

C_{ij} Damping coefficient

$D_{AM,i}$ Diameter of gyration of additional mass in segment

$D_{AMI,i}$ Inner diameter of additional mass in segment

$D_{AMO,i}$ Outer diameter of additional mass in segment

$D_{IM,i}$ Inner mass diameter of segment

$D_{IS,i}$ Inner stiffness diameter of segment

$D_{OM,i}$ Outer mass diameter of segment

$D_{OS,i}$ Outer stiffness diameter of segment

E_i	Young's modulus of shaft segment
e_u	Unbalance eccentricity
f	Frequency
F_X^B	Fluid film force in horizontal direction
F_Y^B	Fluid film force in vertical direction
G_i	Shear modulus of segment
h	Lubricant film thickness
$I_{S,i}$	Area moment of inertia of the shaft segment (around bending axis)
$J_{AD,i}$	Mass moment of inertia (diametric) of the additional mass in segment
$J_{AP,i}$	Mass moment of inertia (polar) of the additional mass in segment
$J_{SD,i}$	Mass moment of inertia (diametric) of the shaft segment
$J_{SP,i}$	Mass moment of inertia (polar) of the shaft segment
k_x	Turbulence coefficient in circumferential direction
k_z	Turbulence coefficient in axial direction
K_{ij}	Stiffness coefficient
L	Bearing width
$L_{S,i}$	Length of segment
m	Bearing geometric preload
M_k	total mass of rotor k
$M_{P,i}$	Mass of pedestal
$M_{S,i}$	Total additional mass in segment
n	Size of autonomous ODE system
N_r	Number of reduced rotor DOFs
N_x	Number of mesh intervals in circumeferential direction
N_z	Number of mesh intervals in axial direction
p	Pressure
R_b	Journal Radius
Re_h	Local Reynolds Number
s	Arclength parameter
sf_i	Shear factor of shaft segment
T	Period

t	time
T_i	Temperature of segment
v	Stability factor
v_i	Poisson's ratio of shaft segment
x_j	Horizontal journal displacement
x_p	Horizontal pedestal displacement
y_j	Vertical journal displacement
y_p	Vertical pedestal displacement

Chapter 1

Introduction

1.1 Steam Turbine-Generator operating fundamentals

A steam turbine is a machine that utilizes thermal energy from pressurized steam to do mechanical work on a rotating shaft which in turn drives the electrical generator. The invention of the modern steam turbine is attributed to Sir Charles Parsons [1, 2]. Steam turbine-generator shaft trains are the dominant method of power generation, about 85% of all electricity generation in the United States in the year 2014 was by use of steam turbines [3]. The global steam turbine market size was estimated at USD 27.93 billion in 2021 and is expected to hit over USD 36.2 billion by 2030 and poised to grow at a CAGR (Compound Annual Growth Rate) of 2.9% from 2021 to 2030 [4].

FIGURE 1.1: Alstom's "ultra-super-critical" steam turbine at the Boxberg power plant in Germany can produce 600MW (credit:GE).

As of 2021, among the largest steam turbines in the world is the Arabelle nuclear steam turbine manufactured by GE based on an original design by Alstom [5]. An Arabelle turbine is 7m in diameter, weighs 4000 tons, spins at 1500 rpm and can produce up to 1900 MW. In a typical nuclear installation, over 4000 tons of supporting steel structure is required, as well as 1000 tons of pumps, valves, and pipes [5].

Continued advances on the design and manufacturing technology of steam turbines and turbo generators in the 20th and 21st century remain core to the energy economy. The first commercial steam turbines in the US were rated at 1.5 MW. From 1910 to around 1920, 30 to 70 MW units were common. By 1945, the median size unit sold in the US was still only 100 MW, but by 1967 the median size unit had increased to 700 MW. Today, the average size is somewhat smaller, but the decrease is the result of non-technical factors, mostly the prevalence of cogeneration and independent power units. Efficiency and reliability have continued to improve until today and supercritical steam conditions on the order of 240 bar and 540 $^{\circ}C$ are common, while having a working life of 30 years or more and more than 42% shaft efficiency. Design of the steam turbine generator system can be divided into the Thermodynamics of the steam cycle, the turbine blade design, the turbine and generator casings and the structural integrity of the rotating shaft and the supporting structures which includes the shaft train rotors, couplings, bearings, pedestals and turning gear.

In Fig. 1.2 a three stage turbine electricity generation powerplant is illustrated. The high pressure steam comes from the boiler and is fed into the high pressure turbine in which steam pressure drops and the kinetic energy of the steam increases. The moving steam impacts on the rotational blades and transfers part of its kinetic energy to these blades. The steam from the outlet is fed into the mid (or intermediate) and low pressure turbines, repeating the process and further dropping the temperature and pressure of the steam. The outlet steam from the low pressure turbine goes into the condenser, in which the temperature of steam drops below its boiling point. The feed water is then reheated using waste heat from the turbines before it is recycled to the boiler.

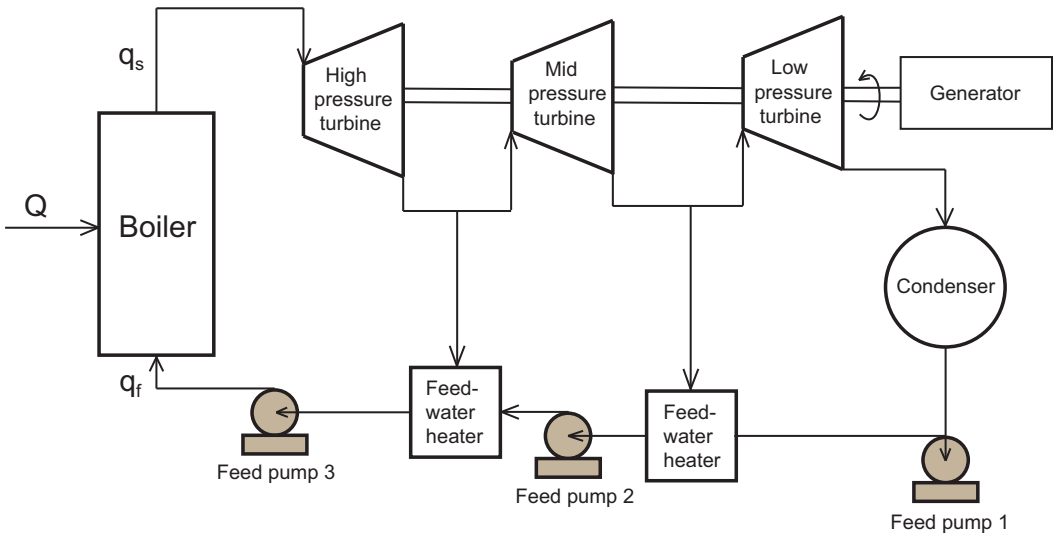

FIGURE 1.2: Schematic illustration of steam turbine power generation [6].

The boiler uses an heat source such as the burning of fossil fuels (coal, natural gas etc.), nuclear fission or renewable sources (renewable natural gas, concentrated solar power) in order to convert the feed water to steam of certain properties. In Fig. 1.3 the percentage of market share in thermal power plants by fuel type in 2018 is shown. Under normal atmospheric pressure (1.01 bar), water boils at 100$^{\circ}C$. When pressure is increased to 221.2 bar, and at a temperature of 374$^{\circ}C$, water does

not boil but is directly converted into steam. This is called the critical point and the pressure above this critical point is called supercritical pressure. Supercritical pressure with a temperature equal or more than $593^{\circ}C$ is called ultra-supercritical pressure. Latest advancements have led to advanced ultra-supercritical technology with temperatures in the range of around $700 - 760^{\circ}C$ and pressure of 350 bar that targets operating efficiency greater than 50%.

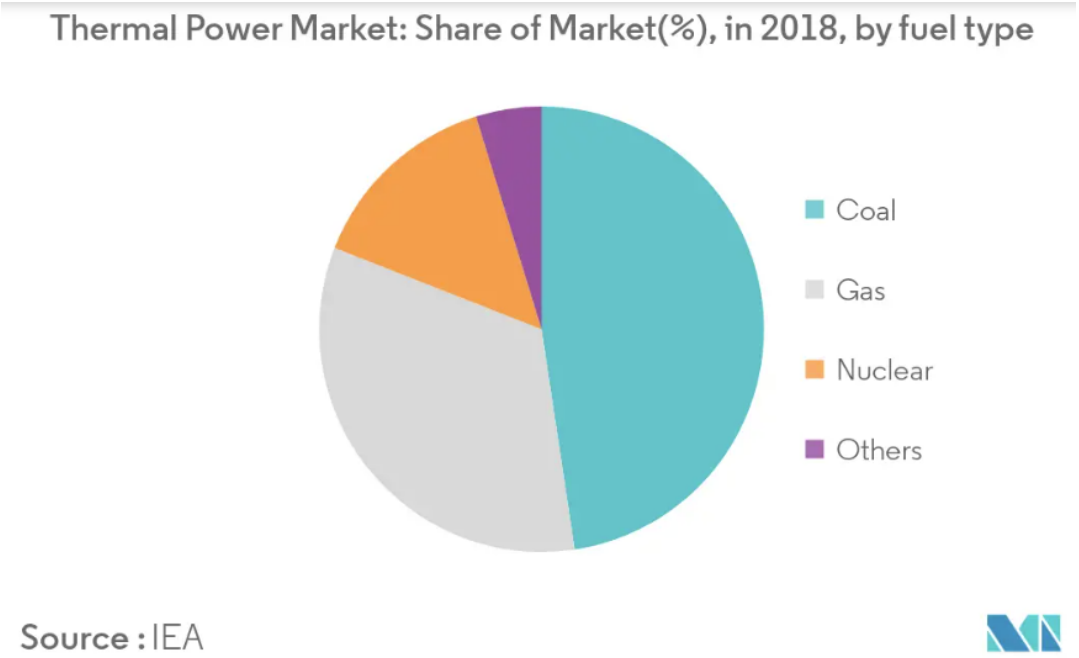

FIGURE 1.3: Percentage of various fuels used in boilers for power generation.

In Fig. 1.4, a cut-out of a three stage steam turbine generator shaft train is illustrated with some of its core parts annotated. There are several technical concerns concerning the structural integrity of a shaft train and its supporting structure including rotor imbalance, vibration, bearing wear and uneven expansion (thermal shock) among others.

Rotordynamics of the shaft train regarding the assessment of bending (lateral) and torsional vibrations and the simulating methodology are of major importance. Turbine applications for power generation implement rotor-bearing systems of medium speed range, mostly from 3000RPM up to 10000RPM or even higher. Depending on the geometrical configuration, steam turbines for power generation are designed to achieve higher or lower speeds of continuous operation. At steady state (at rated speed) such systems should not develop high amplitude vibrations and have a smooth and safe operation that is limited from various standards defined at most cases from the International Standard Organization (ISO) and the American Petroleum Institute (API, see Fig. 1.5). Furthermore, the run-up procedure considers transient rotor vibrations passing through critical speeds and other resonances such as pedestal resonances. The run-up procedure may take considerable time duration till achieved depending on the hot/cold conditions of the rotor-bearing system and of the configuration/type of the machine. The rotordynamic assessment during the run-up of a large turbine-generator shaft line should be precise enough to estimate dynamic parameters of major importance such as critical speeds, critical speed amplitudes, amplification factors in resonances and stability margins, see Fig. 1.5.

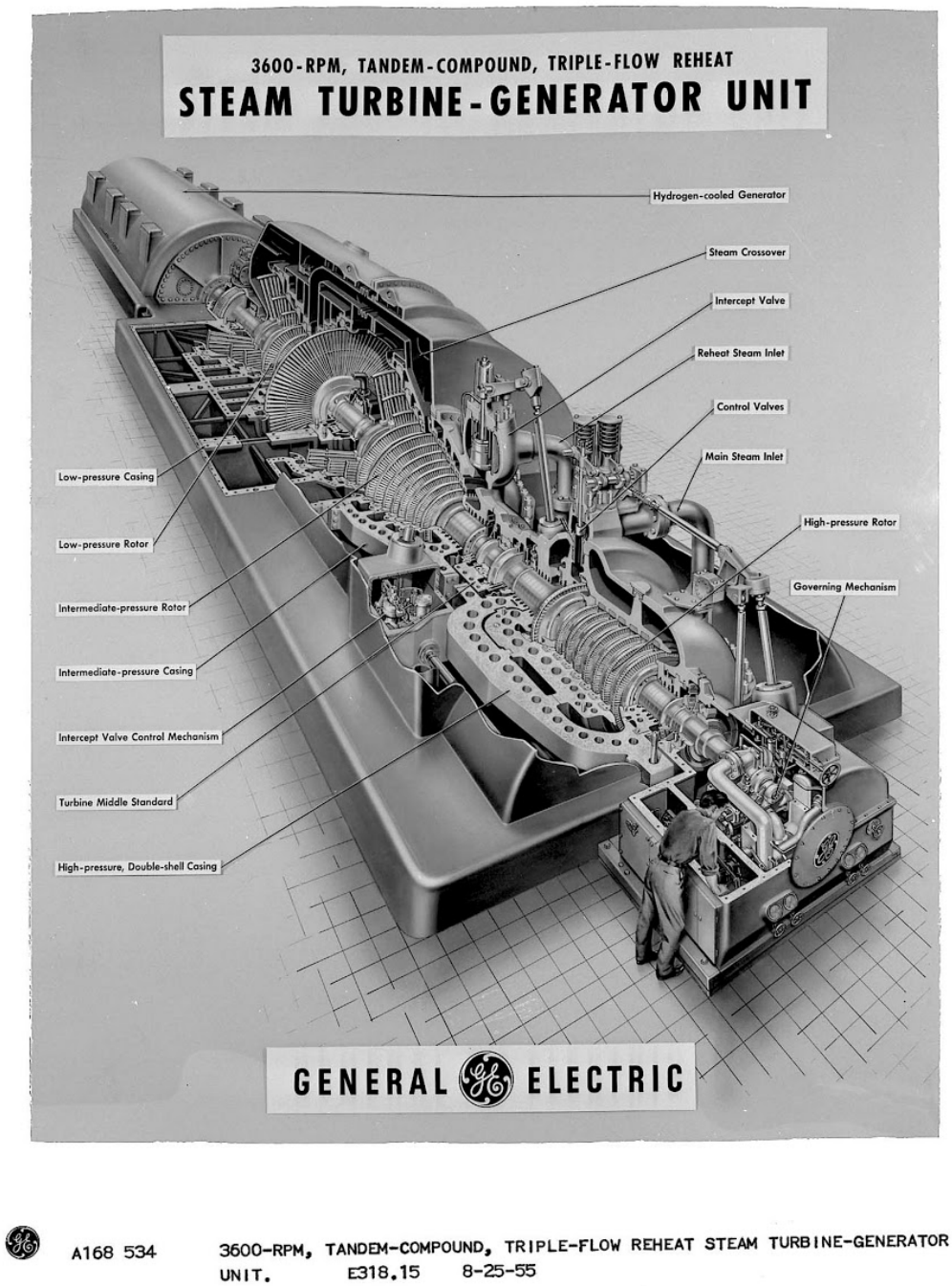

FIGURE 1.4: Illustration of steam turbine generator [6].

Rotor-bearing systems of industrial turbine-generator shaft lines consider slender rotors concerning their elastic deformation due to the static and dynamic loads. At an initial study, the source of the static loads is the gravity forces acting in all major components of the machine (rotor, bearing supports/pedestals, turbine casing), see Fig. 1.8, and the source of the dynamic loads may consider unbalance forces and inertia forces. As a further assessment (if demanded), various dynamic loads may be implemented such as steam flow excitation or other.

A preliminary rotordynamic study of linear rotor and linear bearing properties (see Fig. 1.7) may be enough to give to experienced designers a confident view

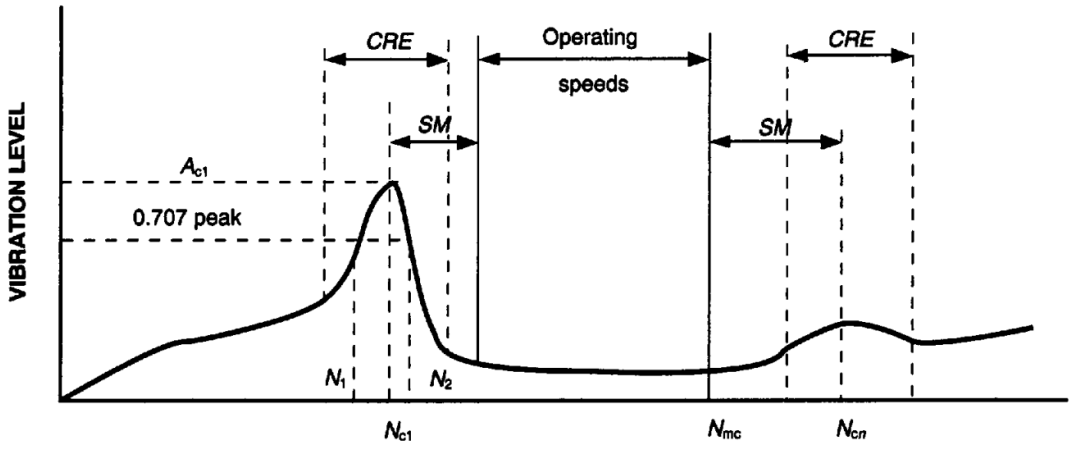

N_{c1} = Rotor first critical, center frequency, cycles per minute.
N_{cn} = Critical speed, nth.
N_{mc} = Maximum continuous speed, 105 percent.
N_1 = Initial (lesser) speed at 0.707 × peak amplitude (critical).
N_2 = Final (greater) speed at 0.707 × peak amplitude (critical).
$N_2 - N_1$ = Peak width at the half-power point.
AF = Amplification factor.

$$= \frac{N_{c1}}{N_2 - N_1}$$

SM = Separation margin.
CRE = Critical response envelope.
A_{c1} = Amplitude at N_{c1}.
A_{cn} = Amplitude at N_{cn}.

Note: The shape of the curve is for illustration only and does not necessarily represent any actual rotor response plot.

FIGURE 1.5: Representation of Rotor Response Plot [7]

.

regarding the mechanical integrity and the performance of the machine. In other words, a harmonic vibration analysis should be enough to render revision or acceptance of a design. However, the demands for even greater performance and more precise rotordynamics initiate the demand for the study of nonlinear phenomena and transient nonlinear response analysis. The main reason is that recent machines have been built with more tight clearances than in the past to improve the thermodynamic performance. Various phenomena may be implemented in a nonlinear transient analysis of a turbine-generator shaft-line. A significant source of nonlinearity that considerably influences dynamic parameters of the machine (such as critical speeds and amplitudes) is the nonlinear oil film forces of the journal bearings. Although the oil-film forces behave linearly enough in the greater range of operating speed, there are ranges of operating speeds close to the critical speeds that would raise considerably higher amplitudes of rotor vibrations and therefore change the oil film forces to behave non-linearly.

1.2 Oil-film Bearings

Oil-film operation is determined by the principle of hydrodynamic lubrication which first requires an always sufficient quantity of oil to fill the clearance between the rotor shaft and the bearing, and second the formation of the oil-film wedge (see Fig.

1.6) and the establishment of the conditions for hydrodynamic lubrication depending on the type of bearing, the relative velocity, the viscosity of the oil and the load. If the load is acting perpendicularly to the shaft axis, then the bearing derives its name from the neck of the shaft and is defined as a "journal bearing". If the load is acting in the direction of the shaft axis, then the bearing is defined as a "thrust bearing" (see Fig.1.10).Journal bearings are classified on the type of the sliding surfaces. If the journal bearing has fixed sliding surfaces, then it is defined as a "sleeve bearing" (Fig. 1.9 (A,B)), otherwise the bearing has one or more pivoted pads, which can tilt freely in which case it is defined as a "tilting pad journal bearing" (TPJB) (Fig. 1.9 (C)).

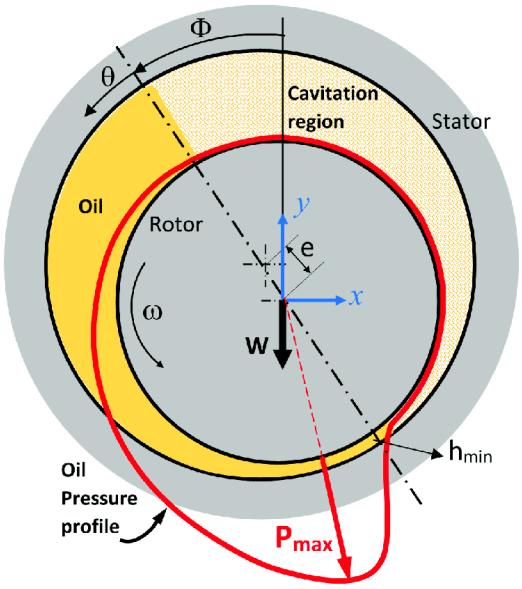

FIGURE 1.6: Illustration of cylindrical journal bearing pressure distribution.

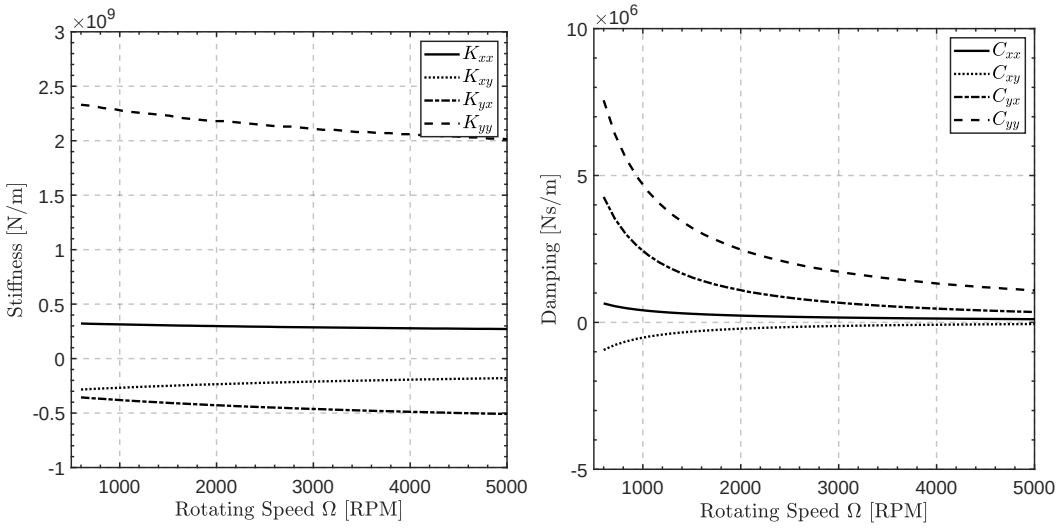

(A) (B)

FIGURE 1.7: Speed depended linearized coefficients of stiffness (A) and damping (B) of the oil film of a partial-arc bearing.

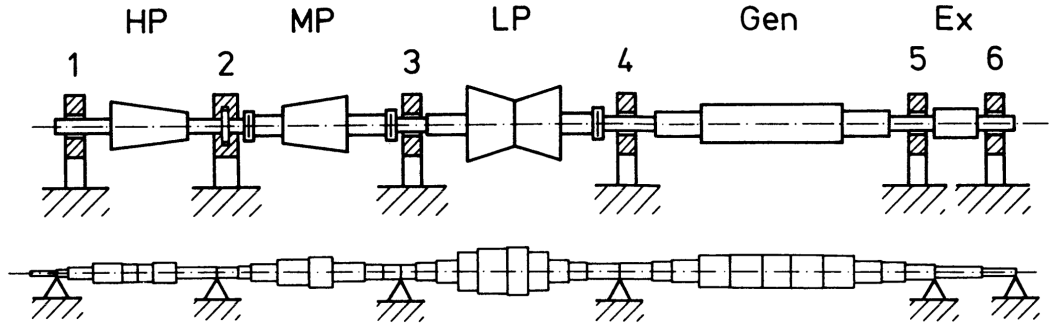

FIGURE 1.8: Schematic of steam turbine generator shaft train with bearings and pedestals. [8].

The basic shape of sleeve bearings is the cylindrical bearing, in which the cross-section of the bearing surface is a circle. However, this kind of bearing is not used in steam turbines, since it is prone to causing instability, in particular oil-whip [9], and has been replaced for a long time by other designs, i.e. by multilobe bearings or by TPJBs. Multilobe bearings have a cross-section composed of two to four circular arcs, forming the so-called "lobes". In the case of two lobes, the bearing is sometimes dubbed as "lemon-bore". Two-lobe bearings may have a pocket machined in the upper half, called the pressure-dam, whose aim is to impose an additional downward load on the shaft, which contributes to stabilizing the rotor (and to increasing the bearing dynamic stiffness).

Tilting pad journal bearings (TPJBs) have several pads, around both the halves of the bearing shell or only in the lower one. Moreover, the pads may have the same or different geometry. Equal pads are the most common case, while, for instance, asymmetric three-pad TPJBs have been used in large steam turbines employed in nuclear power plants while they are ubiquitous in high speed steam turbines (in general small turbines around 20-30 MW or less can run up from 8000 to 15000 RPM). TPJBs were not employed for this work and the reader is referred to [10].

Thrust bearings used in steam turbines are generally of the tilting-pad type. The possibility of the angle of tilt to vary with load improves the load capacity of the bearing. Generally, two thrust bearings are installed in a front-to-front or in a back-to-back configuration in order to balance the axial rotor thrust in both directions(Fig. 1.10).

1.3 Linear bearing & support model

The bearing characteristics concern the linearized coefficients of stiffness and damping that the oil film of the bearing develops at a certain rotating speed of the shaft. The evaluation of these coefficients has been a subject of research from the pioneers in rotordynamics and bearing performance during the latest decades. The bearing shell of each bearing is supposed to be rigidly mounted in the bearing housing. The bearing housing is the surrounding structure of the bearing shell that holds the bearing shell in a fixed position within the extended bearing housing structure, here called pedestal (or bearing support). Each bearing pedestal is a complex structure (see Fig. 1.11) and its properties of stiffness and damping are mostly evaluated using Finite Element Analysis (FEA). The scope of pedestal structural analysis using FEA is to approximate the bearing center displacement for a given static or dynamic load that is supposed to be applied in the non-deformable bearing shell, see Fig.

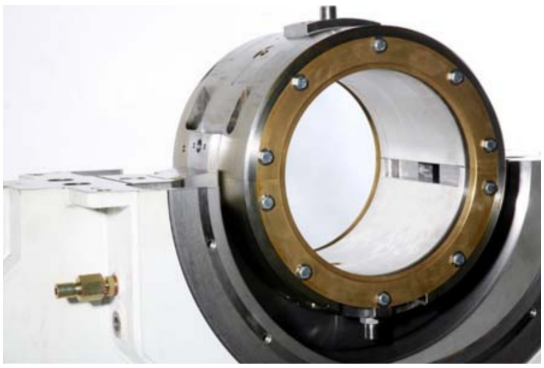

(A)

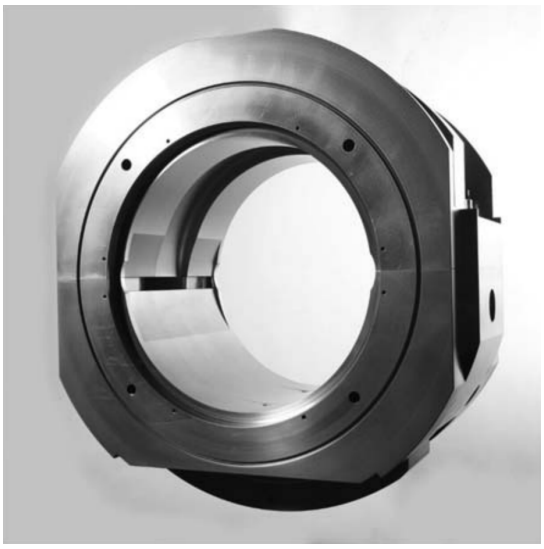

(B)

(C)

FIGURE 1.9: Photos of (A) Cylindrical bearing, (B) two lobe (lemon bore) journal bearing, (C) Tilting pad journal bearing. (Credit: Eurobearings Srl).

1.12. For a given load transmitted from the shaft to the bearing shell (in horizontal and vertical direction), the respective displacement of the bearing shell is evaluated with respect to the rigid foundation. For a static load the static stiffness and damping characteristics are evaluated as $K_{P,X}, C_{P,X}$ in horizontal and $K_{P,Y}, C_{P,Y}$ in vertical direction. For linearly varying load frequency (and constant load amplitude), the dynamic stiffness and damping characteristics can be evaluated as $K_{P,X}(\Omega), C_{P,X}(\Omega)$ in horizontal and $K_{P,Y}(\Omega), C_{P,Y}(\Omega)$ in vertical direction. It should be highlighted that

(A)

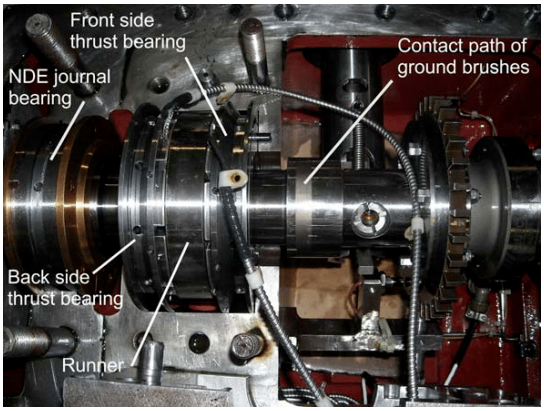

(B)

FIGURE 1.10: Photos of tilting pad thrust bearings (A) and example of front-to-front installation (B). [10]

the only excitation frequency in the pedestal structure is the rotating frequency of the rotor. The pedestal inertia is supposed to be separated regarding its action in horizontal and vertical plane. This simplification aims to enable the good approximation of dynamic stiffness/damping resonant peaks with a 2DOF model per direction, see Fig. 1.13. As shown in Fig. 1.12, there are definitions of "horizontal mass" $M_{P,X}$ and of "vertical mass" $M_{P,Y}$. Typical dynamic stiffness/damping function of a pedestal is presented in Fig. 1.14.

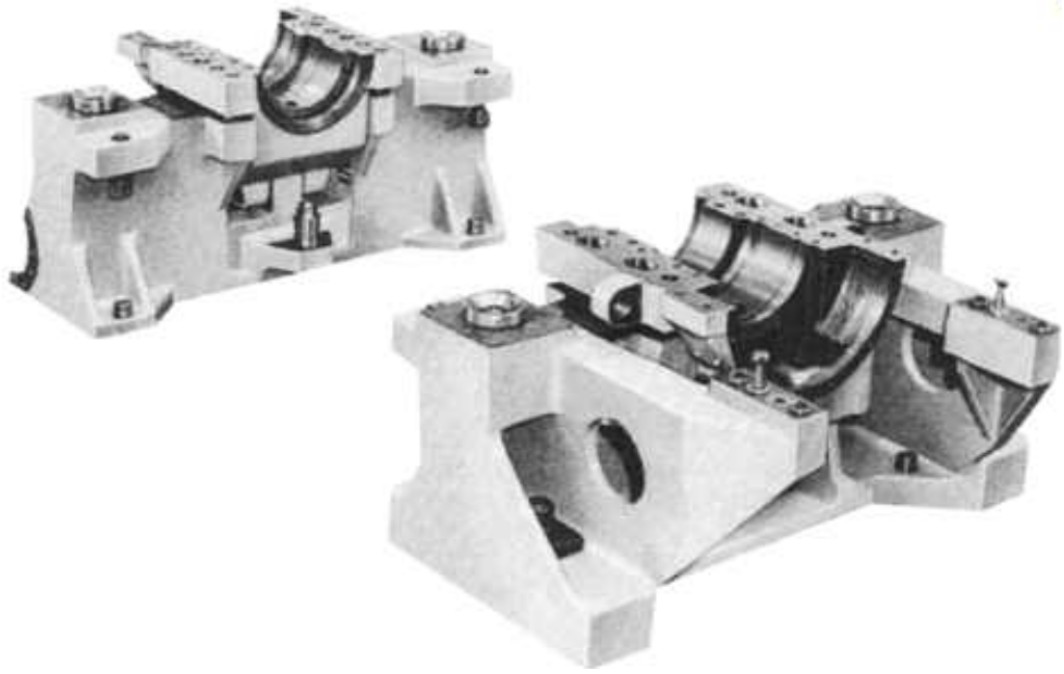

FIGURE 1.11: Pedestals for steam turbine journal bearings (Credit:Siemens).

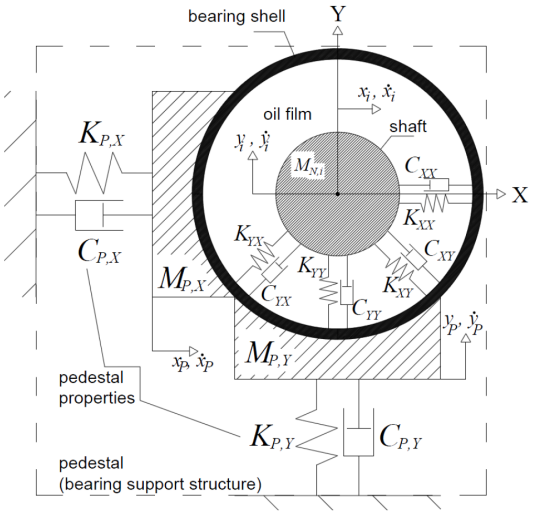

FIGURE 1.12: Configuration of the linear bearing and the linear support structure (pedestal).

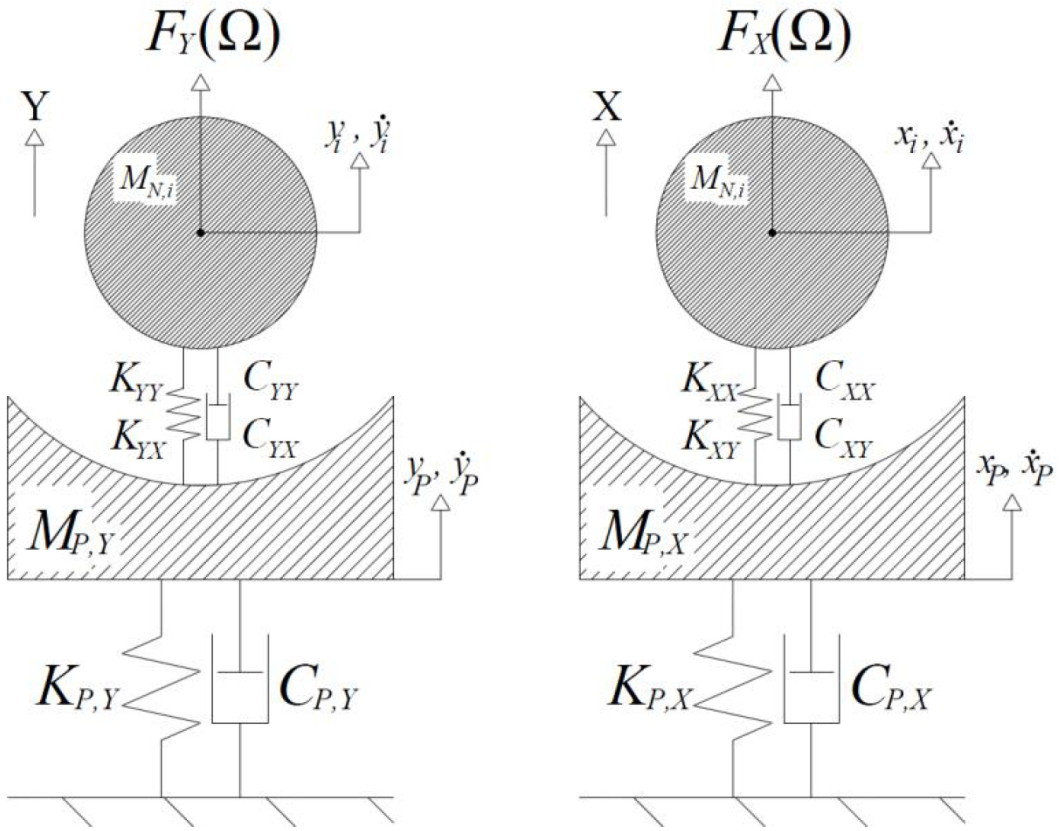

FIGURE 1.13: Simplified layout of the shaft nodal mass (journal) and the bearing support structure (pedestal), in vertical (left) and horizontal plane (right). The coupled (due to oil film cross coupling coefficients) has 2 DoF per plane.

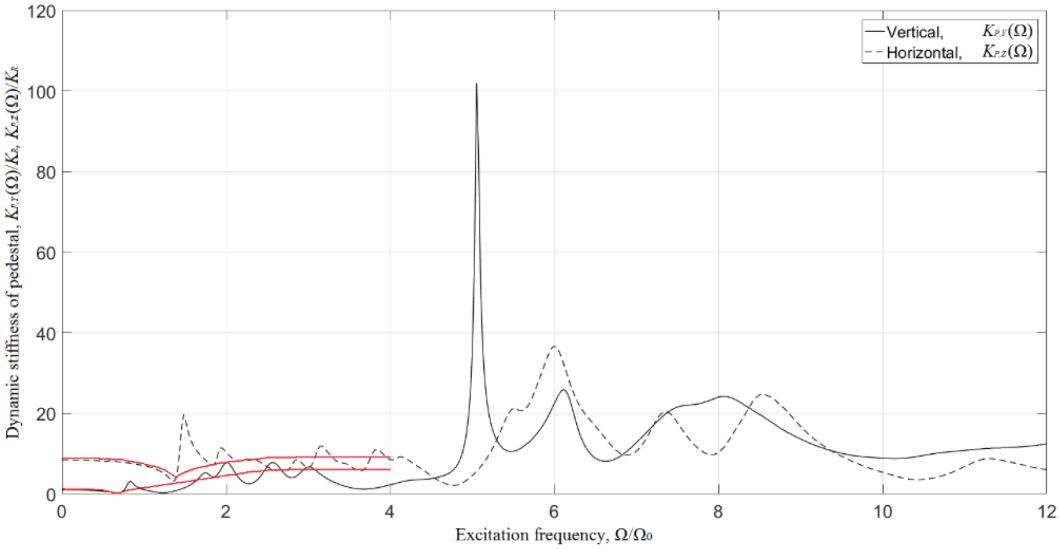

FIGURE 1.14: Typical dynamic stiffness function of a bearing support (pedestal) structure.K_R is the effective bending stiffness of the rotor and Ω_0 is the 1^{st} rigid support natural frequency of the HP turbine rotor.

In Fig. 1.14 is seen that in the frequency range of interest (e.g. $0 < \Omega/\Omega_0 < 4$) the

function $K_{P,X}(\Omega)$ or $K_{P,Y}(\Omega)$ can be approximated in its single peak with an 1DOF per plane model as shown in Fig. 1.13.

1.4 Nonlinear Dynamics of Rotor-Fluid Bearing Systems

Nonlinear phenomena in rotor-bearing systems due to fluid film bearing forces have been observed and studied since the latter half of the twentieth century. In 1965 Tondl [11] and in 1966 Ehrich [12] studied nonlinear resonances due to fluid film forces in journal bearings and squeeze-film damper bearings respectively (see Fig. 1.16). In 1988 and 1991 Ehrich [13, 14] also studied subharmonic resonances of high order and chaotic vibrations in high speed rotor systems. Other nonlinear phenomena arising mainly from oil whirl/whip, such as quasi-periodic, aperiodic motions, Andronov-Hopf and Neimark-Sacker bifurcations were also observed and studied by DiPrima [15], Mayers [16], Hollis and Taylor [17], Muszynska [18], Crooijmans, Brouwers, and D. H. van Campen [19], Ehrich [20], Noah and Sundararajan [21], Chen, Natsiavas, and Nelson [22], Theodossiades and Natsiavas [23], Wang and Khonsari [24, 25], Miraskari, Hemmati, and Gadala [26], Shoyama [27], Chasalevris [28], and Runeng et al. [29]. These works mainly consider simplified rotor systems (Jeffcott rotors of a few DOFs, see Fig. 1.15) and apply mostly perturbation methods like harmonic balance method and multiple scales. For more information on these methods, the reader can refer to Nayfeh and Mook [30] .

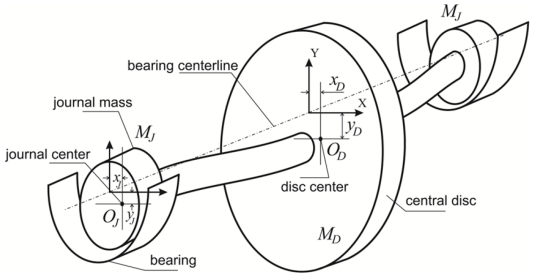

FIGURE 1.15: Representation of a Jeffcott rotor mounted on two identical journal bearings, carrying a disc at the bearing mid-span, and two identical journal masses at its ends [31]

In practical medium speed rotor systems such as those for industrial power generation, the rotor dynamic design is performed by linear harmonic analysis where the fluid film forces are linearized around the static equilibrium point. These linearized stiffness and damping coefficients have been successfully implemented in the stability assessment for various bearing designs (partial arc, lobed, tilting pad, squeeze film damper, floating ring, pressure dam bearings etc.) and for various assumptions in the oil film flow ((heat dependence, turbulence, inertia of the lubricant, boundary conditions for the lubricant flow, cavitation, and others), and operating

[11] A. Tondl. *Some Problems of Rotor Dynamics*. Czechoslovak Academy of Sciences, Prague, 1965
[12] F.F. Ehrich. *Subharmonic Vibration of Rotors in Bearing Clearance*. American Society of Mechanical Engineers. ASME, 1966
[13] F. F. Ehrich. "High Order Subharmonic Response of High Speed Rotors in Bearing Clearance". In: *Journal of Vibration, Acoustics, Stress, and Reliability in Design* 110.1 (Jan. 1988), pp. 9–16
[14] F.F. Ehrich. "Some Observations of Chaotic Vibration Phenomena in High-Speed Rotordynamics". In: *Journal of Vibration and Acoustics* 113 (1991), pp. 50–57
[30] A. H. Nayfeh and D. Mook. *Nonlinear Oscillations*. John Wiley & Sons, 1979

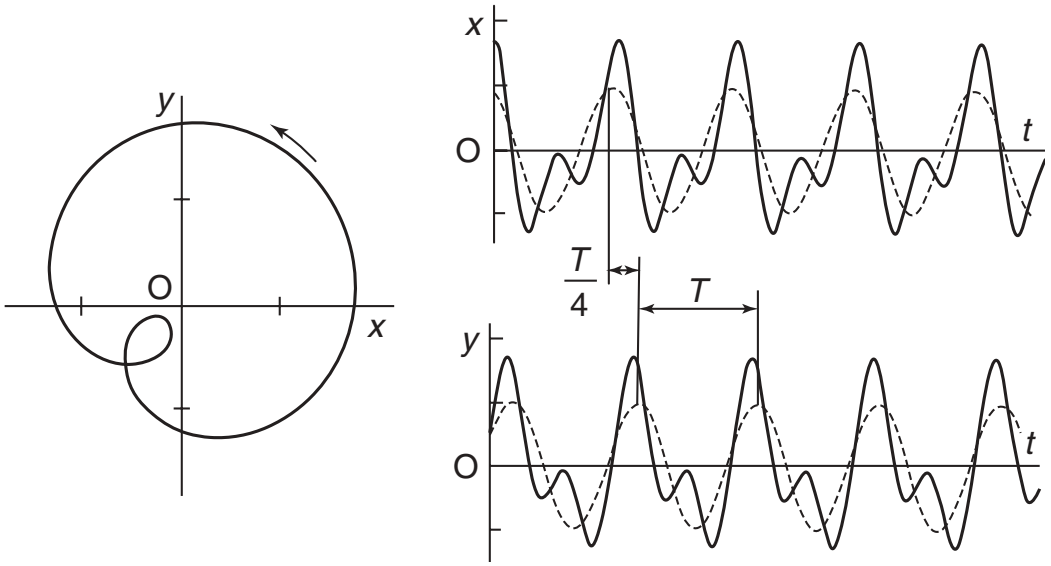

FIGURE 1.16: Time histories and orbit of a subharmonic resonance of order 1/2 [14].

conditions (rotating speed, load)) [9, 32, 33] . It is apparent that linear harmonic analysis can only produce elliptic orbital motions and cannot be used to predict nonlinearities of any kind. In practical high speed rotor systems where the nonlinear behavior cannot be ignored, direct numerical integration of the equations of motion is most commonly employed, however this comes at a large computational cost which makes system design or optimization impractical, particularly for large order systems. Other limitations of direct numerical integration are the inability to compute unstable (repelling) steady state solutions (limit cycles) of the equations of motion and difficulty in computing coexisting stable (attracting) solutions both of which are required to reveal the complete potential of motions and bifurcations.

1.5 Methods of limit cycle calculation

Numerical tools formerly used on the study of dynamic systems, are lately engaged in the study of the quality of motion and of the global stability of nonlinear dynamic rotor bearing systems, still considering simplified rotor models. The method of numerical continuation [34, 35, 36, 37] is a well-known method for finding solution branches in mechanical (and not only) systems even with strong nonlinearities as one (or more) design (or operating) parameters change (as bifurcation parameter).

[9] Y. Hori. *Hydrodynamic Lubrication*. Springer-Verlag, 2006
[32] M. Khonsari and E.Booser. *Applied Tribology: Bearing Design and Lubrication, 3rd Edition*. Wiley online Library, 2010
[33] D. Childs. *Turbomachinery Rotordynamics - Phenomena, Modeling, and Analysis*. John Wiley & Sons, 1993
[34] K. Georg E. L. Allgower. *Introduction to Numerical Continuation Methods*. Society for Industrial and Applied Mathematics, 2003
[35] H. Meijer, F. Dercole, and B. Olderman. *Numerical bifurcation analysis*. Encyclopedia of Complexity and Systems Science, R. A. Meyers Ed. Springer New Yorks, pp. 6329–6352
[36] Y. A. Kuznetsov. *Elements of applied bifurcation theory 2nd ed.* Applied mathematical sciences. Springer New York, 1998
[37] A. H. Nayfeh and B. Balachandran. *Applied nonlinear dynamics*. Wiley series in nonlinear science. J. Wiley & Sons, 1995

The numerical continuation method, in one of its most popular versions (pseudo arc length continuation) has the primary advance to study MDOF systems where the nonlinear motion equations can be many [38]. In the current work, the author programmed the pseudo arc length continuation of limit cycles directly from the notes [34, 37, 39] . Numerical continuation has been lately applied in the study of nonlinear rotor bearing systems, and the potential of the applicability of the respective methodology in rotor bearing systems appears to rise in the literature. Among the various contributions, in [40, 41, 42] simplified models of high speed rotors on floating ring bearings are studied, while in [43, 44, 45, 46] Jeffcott rotor models in simple oil film bearings are studied on their bifurcation sets. In [31] complex bearing profiles and bearing pedestal models are included. Recently, the bifurcation sets of simple rotor models on adjustable bearings [47] and on [48] gas-foil bearings where extensively studied. The works hereby referred do not consider complex rotor models but simplistic models of few DOFs, as most of the effort was on the respective bearing models. In [49, 50, 51] the deflation method is applied to evaluate solution branches (fixed points and limit cycles) in simple and in MDOF rotor systems of high speed. The current work primarily aims to reveal the potential of a realistic turbine-generator shaft train model to produce motions of different quality (further to the well-known and widely studied linear elliptic orbits) which may lie close to the linearly predicted stable whirling. Secondary, the well-known method of numerical continuation for analyzing the motions and the global stability of MDOF nonlinear systems, is applied in a large scale system whose nonlinear motions may be rather different than those predicted by the simplified rotor models. Furthermore, unbalance response is evaluated for the non-autonomous (unbalanced rotor) investigating the potential of unstable motions in speeds lower than the service speed. Further to that, realistic bearing models (of partial arc and lemon bore configuration) are engaged in the analysis, while simplified pedestal models (1 DOF per direction) is included in the analysis to investigate the influence of the foundation properties in the bifurcation set. Case studies conclude the influence of misalignment, of partial arc and lemon bore bearing key design parameters (arc length, preload, offset), of pedestal properties (stiffness and damping), and of rotor properties (slenderness ratio - flexibility) on the bifurcation set of fixed points and of limit cycles for the autonomous (balanced) and the non-autonomous (unbalanced) shaft train.

[34] E. J. Doedel, H.B. Keller, and J.P. Kernevez. "Nonlinear dynamic analysis of supercritical and subcritical Hopf bifurcations in gas foil bearing-rotor systems". In: *International Journal of Bifurcation and Chaos* 1.3 (1991), pp. 745–772

[34] K. Georg E. L. Allgower. *Introduction to Numerical Continuation Methods*. Society for Industrial and Applied Mathematics, 2003

[37] A. H. Nayfeh and B. Balachandran. *Applied nonlinear dynamics*. Wiley series in nonlinear science. J. Wiley & Sons, 1995

[39] E. J. Doedel. "Lecture Notes on Numerical Analysis of Nonlinear Equations". In: *Department of Computer Science, Concordia University, Montreal, Canada* ()

TABLE 1.1: Timeline of application of numerical continuation in rotor bearing systems

Year	Author and Details	Illustrations
2009	Boyaci et al. [40]- Symmetric and balanced rigid rotor with floating ring bearings. Center manifold reduction and comparison with AUTO bifurcation diagrams.	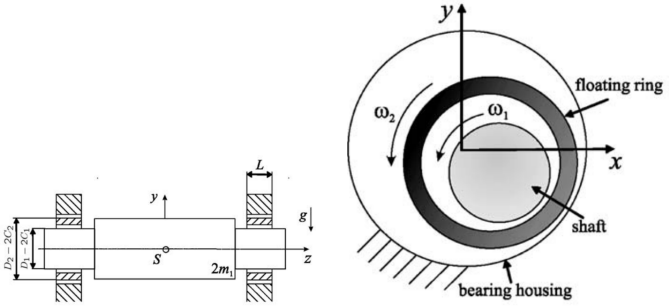
	Rubel [43]-MDOF (turbocharger) systems, Plain Journal Bearings, Evaluation of periodic and quasiperiodic limit cycles with using AUTO and TORCONT.	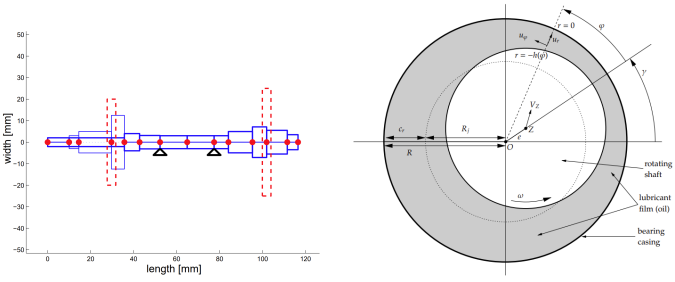
2011	Amamou and Chouchane [44]- Symmetric rigid Jeffcott rotor, Short bearing approximation, Evaluation of periodic limit cycles using MATCONT.	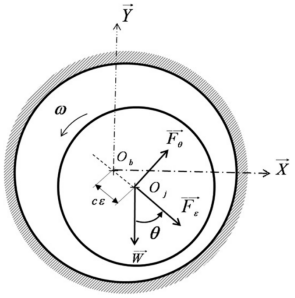
2015	Sghir and Chouchane [45]-Symmetric rigid Jeffcott rotor, Short bearing approximation, Evaluation of periodic limit cycles using MATCONT.	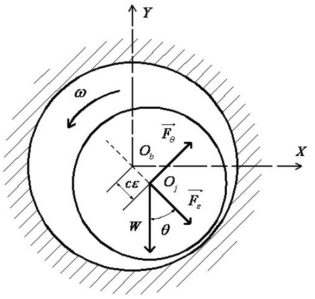
	Boyaci, Lu, and Schweizer [41]- Symmetric elastic and damped Jeffcott rotor, Semi-floating ring bearings. Evaluation of periodic limit cycles using MATCONT.	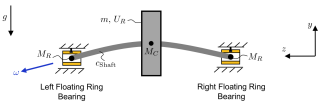
2016	Sghir and Chouchane [46]-Symmetric elastic Jeffcott rotor, Short bearing approximation. Evaluation of periodic limit cycles using MATCONT.	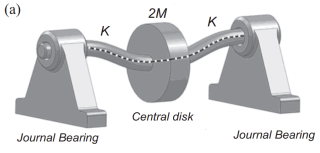

Timeline of application of numerical continuation in rotor bearing systems (Continued)

Year	Author and Details	Illustrations
	Breemen [42]-Symmetric elastic and damped Jeffcott rotor, Short bearing approximation. Evaluation of periodic limit cycles using MATCONT.	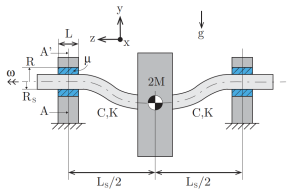 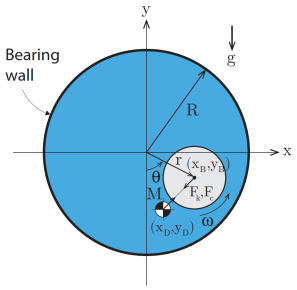
2017	Kim and Palazzolo [49, 50, 51]-Jeffcott and MDOF (Turbocharger,Compressor) systems, Floating ring bearings and TPJBs. Evaluation of periodit limit cycles using shooting method.	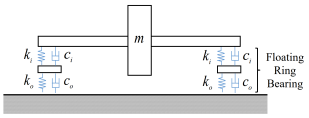 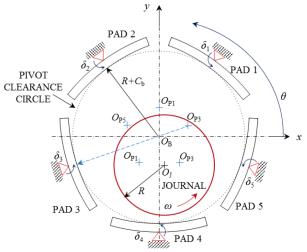 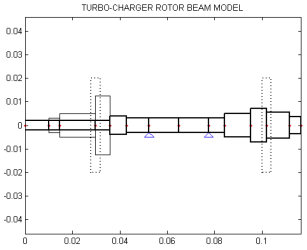 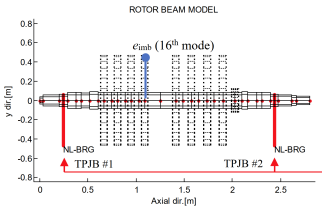
2019	Becker [47]-Jeffcott rotor, Sleeve bearings of variable geometry. Evaluation of periodic and quasiperiodic limit cycles with HBM.	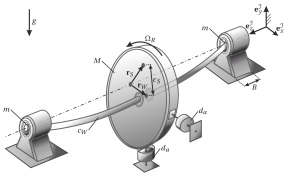 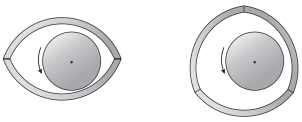
2021	Leister [48]-Jeffcott rotor, Refrigerant-Lubricated Gas Foil Bearings. Evaluation of periodic limit cycles using AUTO2000. Anastasopoulos and Chasalevris [31]-Symmetric elastic and damped Jeffcott rotor with 2DOF pedestals, lemon bore and partial-arc bearings. Evaluation of periodic limit cycles using MATCONT.	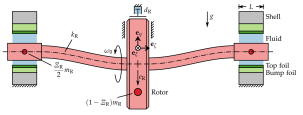 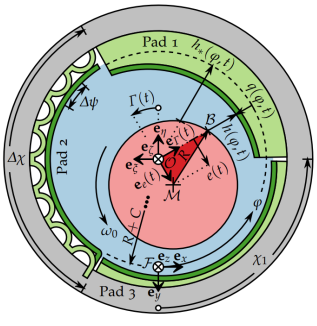 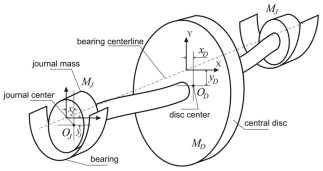 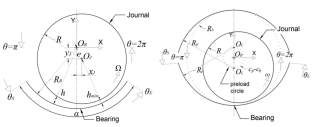

Chapter 2

Model and formulation of the shaft train

In this Chapter the methods used to formulate the shaft train model are presented. These methods and all underlying assumptions form the basis for the rest of the work done during this thesis. The main objective of this chapter is to give the reader a brief overview of the relevant theory concerning modeling rotors, element order reduction methods and modeling of the bearings and pedestals as performed in this work, with references to literature and Appendices, where deemed appropriate.

2.1 Model of Rotor

In practice, rotating machines have complex geometry. In turbomachinery for power generation for example, multiple flexible shafts with variable cross sections with flexible disks, blades and generator windings and connected with flexible or rigid couplings of various stiffness. Such machines cannot be modeled by Jeffcott or Laval rotors as it is important to accurately calculate the eigenfrequencies, vibration modes and unbalance response for the respective rotor design. To this end, the rotor is discretized with continuous beam elements, each element having two nodes and eight total degrees of freedom (lateral bending). The equations of motion for a multi-degree-of-freedom (MDOF) system are represented in matrix form as follows:

$$\mathbf{M}\ddot{\boldsymbol{q}} + (\mathbf{C} + \Omega\mathbf{G})\dot{\boldsymbol{q}} + \mathbf{K}\boldsymbol{q} = \boldsymbol{f} \tag{2.1}$$

where $\mathbf{M}$, $\mathbf{C}$, $\mathbf{G}$, $\mathbf{K}$ are the mass (or inertia) matrix, damping matrix, gyroscopic matrix and stiffness matrix for the complete system (square matrices of size No. of DOFs, asymmetric in general due to bearing linear coefficients and gyroscopic terms) respectively and are assembled from the individual element matrices, and $\boldsymbol{q}$ and $\boldsymbol{f}$ are the displacement vector and force vector (of length No. of DOFs) respectively. An example is given below for a three element matrix. It is reminded that every individual element matrix is of size 8×8 and so if we follow conventional numbering rules (see A) the elements in the cross-hatched area are calculated from the sum of the respective element matrices. The element matrices derivation is based on the Timoshenko beam theory as presented in [52, 53].

For the accurate representation of the rotor using finite elements, the discretization should follow clear changes of diameter, and locations where the evaluation of

[52] Y. Ishida and T. Yamamoto. *Linear and Nonlinear Rotordynamics: A Modern Treatment with Applications, Second Edition*. Wiley-VCH Verlag GmbH & Co. KGaA, 2012

[53] J. M. McVaugh H. D. Nelson. "The Dynamics of Rotor-Bearing Systems Using Finite Elements." In: *ASME Journal of Engineering for Industry* 98 (1976), pp. 593–600

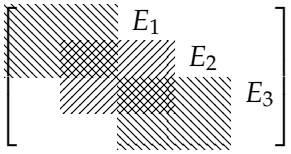

FIGURE 2.1: Example of global matrix assembly from three finite elements

response if of crucial importance (e.g. bearings, steam path, gland sealing, unbalance nodes).

It should be noted that for a rotor made from fully linear-elastic material, the damping matrix $\mathbf{C}$ is given by the classical Rayleigh damping $\mathbf{C} = \alpha\mathbf{M} + \beta\mathbf{K}$, where α, β are real scalars. A small numerical damping value is applied to the rotor ($\mathbf{C} = 10^{-5}\mathbf{K}$) in order to make the ODE[1] system less numerically stiff without affecting the dynamic behavior.

The geometric and physical properties must be supplied for all segments defined in the discretized shaft train. These are defined in Table 2.1. A brief description of the properties will first be given.

The outer and inner mass diameters $M_{OM,i}, M_{IM,i}$ define the geometrical outline of the material of the shaft. The outer and inner stiffness diameters $M_{OS,i}, M_{IS,i}$ define the volume of the segment that would receive load due to bending. The effective stiffness of the shaft is influenced from the stiffness diameters. The mass diameters influence the mass and the inertia of each segment and therefore the total mass and inertia of the rotor.

It is advisable that a segment should not have a length to stiffness diameter ratio $L_{S,i}/D_{OS,i}$ less than 0.05 or greater than 0.8. Furthermore, comparing the length to stiffness diameter ratio of two sequential segments, these should not differ more than a factor of 4. The discretization of Fig. 2.5 is according to such considerations, however there are many alternative mesh configurations that may be acceptable.

In Fig. 2.2 it is shown that the stiffness diameter line (dashed line) should define two triangles of equal area (hatched) in each segment. Stiffness diameter equals mass diameter when the entire segment's cross section participates in bending, as it happens for instance in the winding portion of the GEN rotor. It is very common that shafts also include cavities (hollow shaft). A cavity may be designed where two shafts are welded together, or for other reasons like lowering thermal stresses and shaft elongation. In the case of hollow shaft, the diameters of interest are similarly defined.

Additional mass may exist in a rotor segment, such as rotating blades (in a turbine rotor) or wiring (in a generator rotor). In Fig. 2.3 the additional masses represent the rotating blades of the turbine rotor or other components (e.g. gears, fans etc.).

Additional mass is implemented by two parameters, the first being the diameter of gyration D_{AM}, as defined in Fig. 2.3, and the second being the total mass that is added in the shaft segment, M_{AM}. For instance, in segment 13, see Fig. 2.3, the additional mass M_{AM} is the mass of one blade multiplied by the number of blades existing in segment 13. The center of gravity of one blade is defined also in Fig. 2.3, for all blades at all stages.

[1]ODE: Ordinary Differential Equation

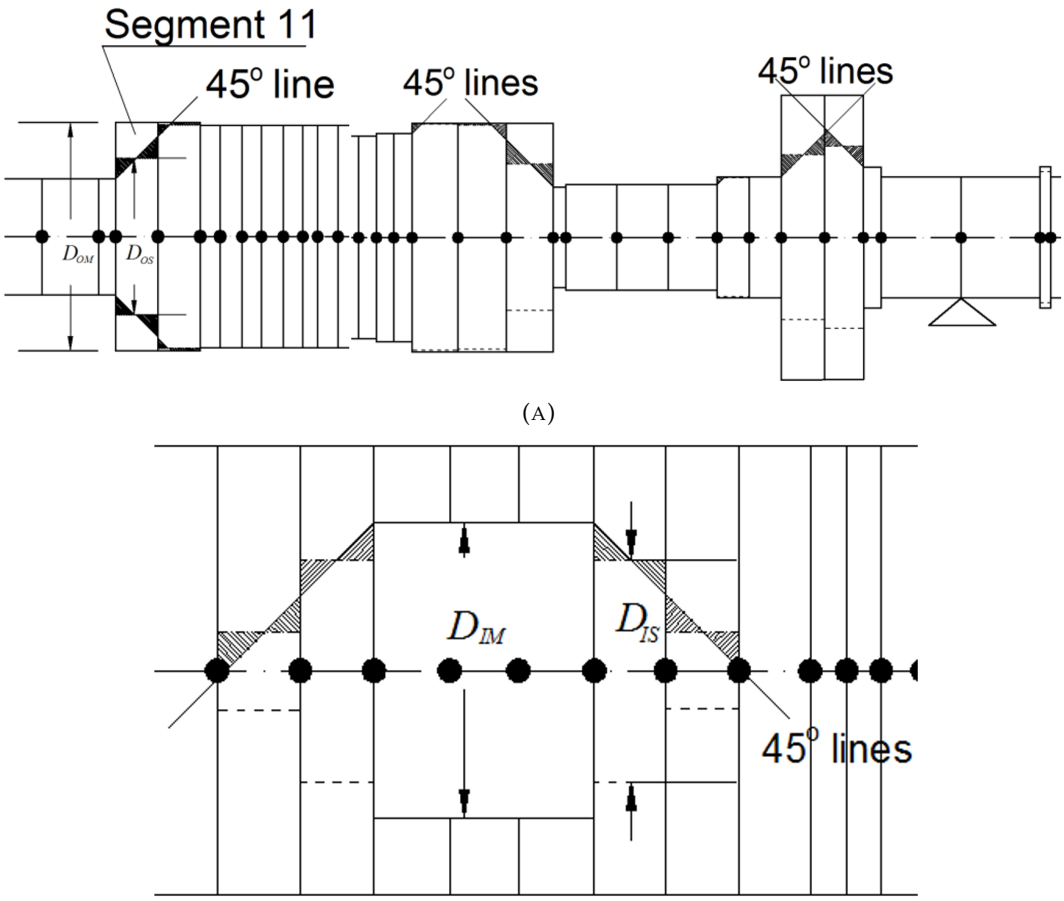

FIGURE 2.2: Definition of outside (A) and inside (B) stiffness diameters using the 45° rule in segments where change in mass diameter is notified.

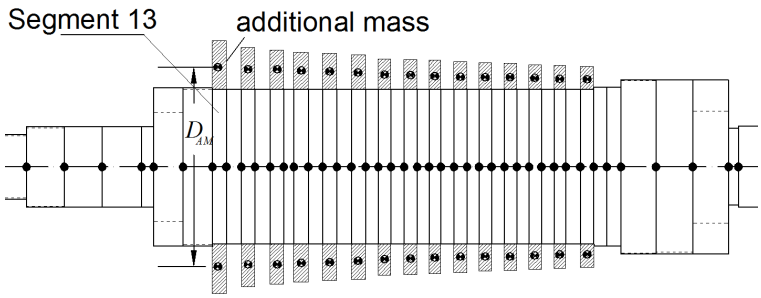

FIGURE 2.3: Representation of additional mass in a segment and definition of additional mass diameter D_{AM}

A very important parameter that should be implemented in the simulation is the temperature at each shaft segment. Steam turbine rotors experience temperatures above $500^{\circ}C$ in some segments. A typical temperature distribution in a steam turbine rotor is presented in Fig. 2.5b. Such temperatures degrade the modulus of elasticity of the material of shaft segment. The considerable degradation of modulus of elasticity due to temperature is shown in Fig. 2.4

TABLE 2.1: Definition of the geometric and physical properties of the rotor segment $i = 1, 2, \ldots, N$

Symbol	Description	Definition
$L_{S,i}$	Length of segment	
$D_{OM,i}$	Outer mass diameter of segment	$D_{OM,i} = 2R_{OM,i}$
$D_{IM,i}$	Inner mass diameter of segment	$D_{IM,i} = 2R_{IM,i}$
$D_{OS,i}$	Outer stiffness diameter of segment	$D_{OS,i} = 2R_{OS,i}$
$D_{IS,i}$	Inner stiffness diameter of segment	$D_{IS,i} = 2R_{IS,i}$
$D_{AMI,i}$	Inner diameter of additional mass in segment	$D_{AMI,i} = 2R_{AMI,i} = D_{OM,i} = 2R_{OM,i}$
$D_{AMO,i}$	Outer diameter of additional mass in segment	$D_{AMO,i} = 2R_{AMO,i}$
$D_{AM,i}$	Diameter of gyration of additional mass in segment	$D_{AM,i} = 2R_{AM,i} = \sqrt{D_{AMI,i}^2 + D_{AMO,i}^2}$
T_i	Temperature of segment	
E_i	Young's modulus of shaft segment	
G_i	Shear modulus of segment	$G_i = \dfrac{E_i}{2(1+v_i)}$
v_i	Poisson's ratio of shaft segment	
ρ_i	Density of material of shaft segment	
sf_i	Shear factor of shaft segment	$sf_i = \dfrac{7+6v_i}{6+6v_i}$
$A_{S,i}$	Area of cross section of shaft segment, considering stiffness	$A_{S,i} = \pi R_{OS,i}^2 - \pi R_{OS,i}^2$
$A_{M,i}$	Area of cross section of shaft segment, considering mass	$A_{M,i} = \pi R_{OM,i}^2 - \pi R_{IM,i}^2$
$A_{AM,i}$	Area of cross section of additional mass in segment	$A_{AM,i} = \pi R_{AMO,i}^2 - \pi R_{AMI,i}^2$
$M_{S,i}$	Mass of shaft segment	$M_{S,i} = \rho_i A_{M,i} L_{S,i}$
$M_{AM,i}$	Total additional mass in segment	
$I_{S,i}$	Area moment of inertia of the shaft segment (around bending axis)	$I_{S,i} = \pi(R_{OS,i}^4 - R_{IS,i}^4)/4$
$J_{SP,i}$	Mass moment of inertia (polar) of the shaft segment	$J_{SP,i} = M_{S,i}(R_{OM,i}^2 + R_{IM,i}^2)/2$
$J_{SD,i}$	Mass moment of inertia (diametric) of the shaft segment	$J_{SD,i} = J_{SP,i}/2 + M_{S,i}L_{S,i}^2/12$
$J_{AP,i}$	Mass moment of inertia (polar) of the additional mass in segment	$J_{AP,i} = M_{AM,i}(R_{AMO,i}^2 + R_{AMI,i}^2)/2$
$J_{AD,i}$	Mass moment of inertia (diametric) of the additional mass in segment	$J_{AD,i} = J_{AP,i}/2 + M_{AM,i}L_{S,i}^2/12$

The shaft train studied in this thesis is a representative multi-rotor, multi-bearing shaft train of a turbine-generator as shown in Fig. 2.5. The rotors are connected to each other with rigid couplings. Static alignment (see Fig. 2.6) is performed in the shaft train elevating the bearings #1, #4 and #5 by δ_1, δ_4 and δ_5 respectively to minimize the bending moment in the coupling flanges and to ensure loading in bearing #5 (approximately 10 kN). Bearings #2 and #3 are not elevated ($\delta_2 = \delta_3 = 0$).

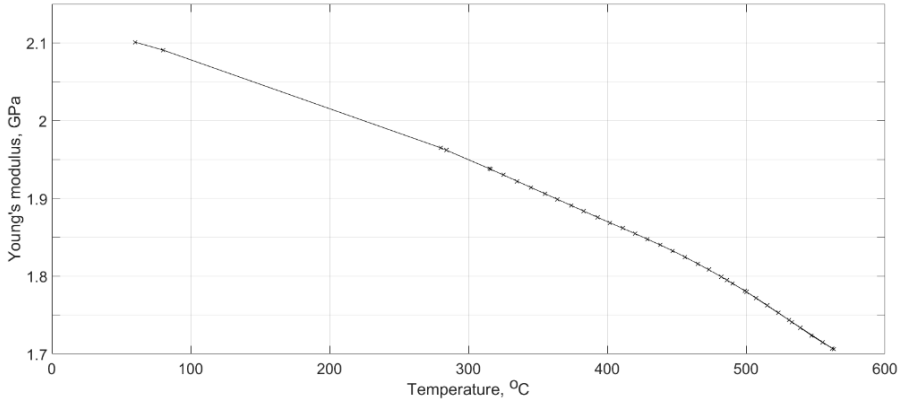

FIGURE 2.4: Modulus of elasticity as a function of temperature for a typical steam turbine shaft steel.

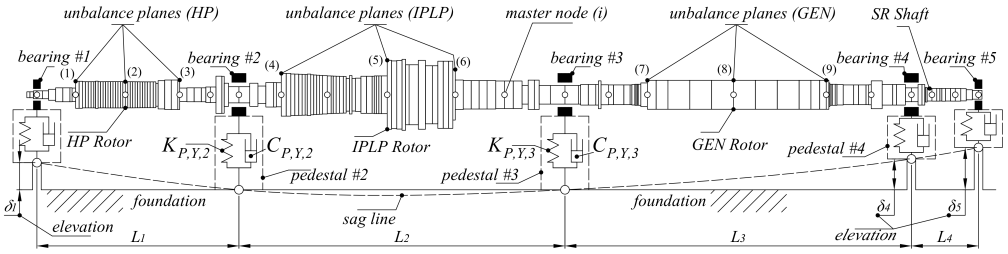

(A)

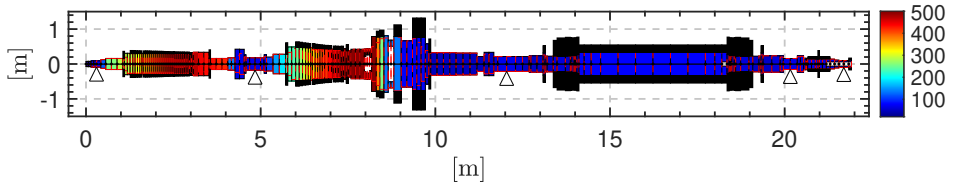

(B)

FIGURE 2.5: Representation of a turbine-generator shaft train consisting of 4 rotors (HP IPLP GEN SR shaft) and 5 bearings/pedestals. Finite element discretization, bearing elevation δ_i , sag line, bearing span L_i , balance planes, and master nodes are also depicted in figure. Temperature distribution and additional masses of blades, gears and fans, and generator wiring are included in the model as shown in 2.5b

The shaft train consists of 184 beam elements with 740 DoFs (184 finite elements, 185 nodes, 4 DoFs per node). The bearing pedestals are modeled by linear springs

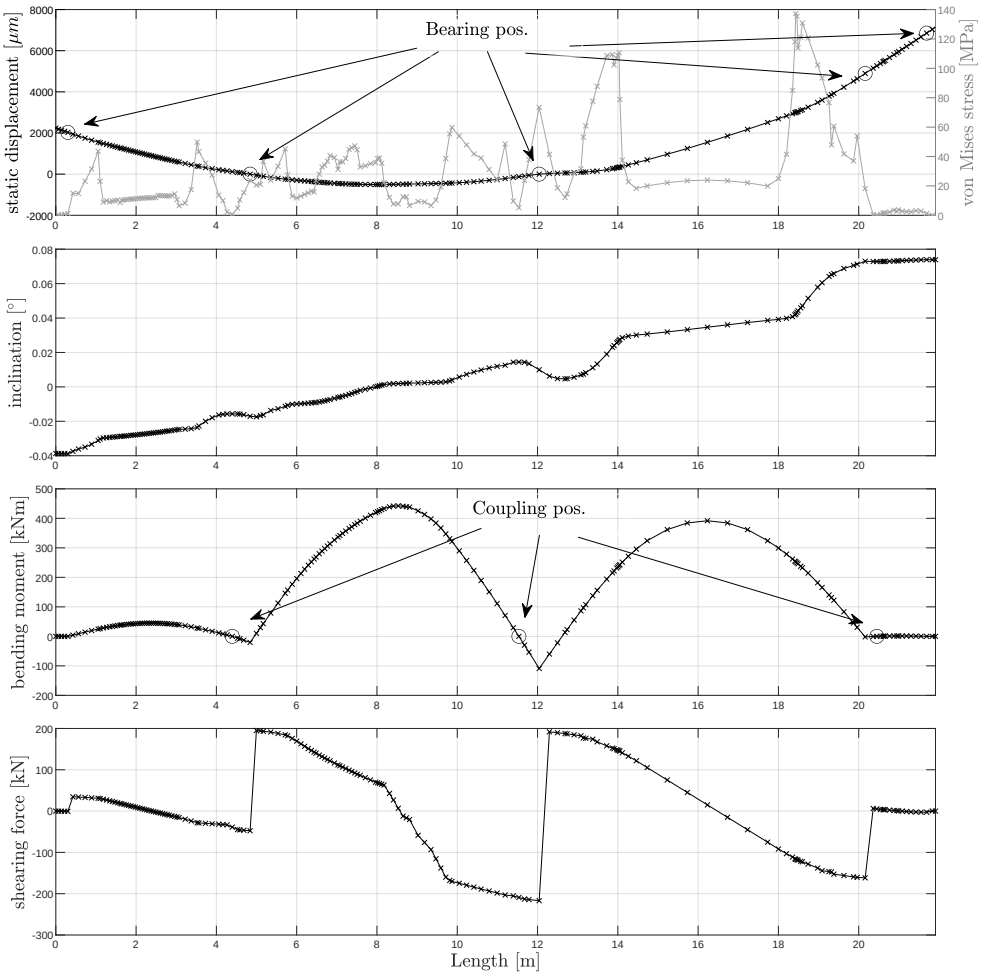

FIGURE 2.6: Static Alignment of Shaft train.

with point mass (1 DoF per translational DoF without cross-coupling of coefficients for an additional 10 DoFs). Since the rotor and pedestals are coupled only through the bearing forces there are no cross-coupling terms between the rotor and pedestal DoFs but for simplicity of notation the pedestal matrices $\mathbf{M}_p, \mathbf{C}_p, \mathbf{G}_p, \mathbf{K}_p$ can be appended to the rotor matrices. The matrices $\mathbf{M}_p, \mathbf{C}_p, \mathbf{K}_p$ are diagonal of size 10×10 and the gyroscopic matrix $\mathbf{G}_p$ is the zero matrix of size 10×10. It follows that the complete system matrices are of size 750×750.

The force vector $\boldsymbol{f}$ consists of the bearing forces ($\boldsymbol{f}_i^B$), the unbalance forces ($\boldsymbol{f}_i^U$) and the gravity forces in rotor and pedestals ($\boldsymbol{f}_i^G$). Unbalance forces are considered for selected nodes and for constant rotating speed Ω, according to the unbalance cases some of them being e.g. single/pair unbalance in IPLP rotor, single/pair/triple unbalance in GEN rotor. M_k is the total mass (shaft mass and additional masses) of the rotor part (k = 1,2,3,4) defined between sequential bearing locations. The unbalance eccentricity e_u follows in this thesis the ISO G-grade definition with service speed of the shaft train at $\Omega = 377 rad/s$. G-grade 2.5 applies in such systems as reference, therefore $e_u = G/\Omega_r = 6.6[\mu m]$ applies for the reference unbalance calculation.

$$\boldsymbol{f}_{i,X}^U = M_k e_u \Omega^2 cos(\Omega t), \quad \boldsymbol{f}_{i,Y}^U = M_k e_u \Omega^2 sin(\Omega t) \tag{2.2}$$

2.2 Linear Harmonic Analysis

The well established Linear Harmonic Analysis consists of calculating the eigenvalues of the system and the calculation of the steady-state synchronous response. The eigenvalues of the linear system can be calculated by setting the force vector to zero (free vibration) and converting Eq. 2.1 to a 1st order ODE by setting

$$\boldsymbol{x} = \begin{Bmatrix} \dot{\boldsymbol{q}} \\ \boldsymbol{q} \end{Bmatrix} \tag{2.3}$$

and then Eq. 2.1 becomes

$$\mathbf{A}\dot{\boldsymbol{x}} + \mathbf{B}\boldsymbol{x} = \boldsymbol{Q} \tag{2.4}$$

where

$$\mathbf{A} = \begin{bmatrix} \mathbf{0} & \mathbf{M} \\ \mathbf{M} & \mathbf{C} + \Omega\mathbf{G} \end{bmatrix}, \quad \mathbf{B} = \begin{bmatrix} -\mathbf{M} & \mathbf{0} \\ \mathbf{0} & \mathbf{K} \end{bmatrix}, \quad \boldsymbol{Q} = \begin{bmatrix} \mathbf{0} \\ \boldsymbol{f} \end{bmatrix}$$

For free vibrations, $\boldsymbol{Q} = 0$ and a solution of Eq. 2.4 is sought of the form $\boldsymbol{x} = \boldsymbol{\phi} e^{\lambda t}$. Substituting in Eq. 2.4 then gives:

$$[\lambda\mathbf{A} + \mathbf{B}]\boldsymbol{\phi} = \mathbf{0}$$

or in the familiar eigenvalue problem form:

$$\mathbf{D}\boldsymbol{\phi} = \frac{1}{\lambda}\boldsymbol{\phi} \tag{2.5}$$

where $\mathbf{D} = -\mathbf{B}^{-1}\mathbf{A}$.

The steady-state synchronous response for synchronous harmonic excitation of the form $f(t) = \boldsymbol{X}_c cos(\Omega t) + \boldsymbol{X}_s sin(\Omega t)$ can be written as $\boldsymbol{q}(t) = \boldsymbol{A}_c cos(\Omega t) + \boldsymbol{A}_s sin(\Omega t)$. Substituting to the equations of motion, the steady-state response can be calculated from the following set of linear algebraic equations:

$$\begin{bmatrix} \mathbf{K} - \Omega^2\mathbf{M} & \Omega\mathbf{C} \\ -\Omega\mathbf{C} & \mathbf{K} - \Omega^2\mathbf{M} \end{bmatrix} \begin{bmatrix} \boldsymbol{A}_c \\ \boldsymbol{A}_s \end{bmatrix} = \begin{bmatrix} \boldsymbol{X}_c \\ \boldsymbol{X}_s \end{bmatrix} \tag{2.6}$$

In Fig. 2.7 the harmonic response of the shaft train at operating speed with *G*2.5 generator pair unbalance is shown.

2.3 Model Order Reduction

The rotor model is reduced applying static (Guyan) reduction [54] retaining 2 Master DoFs (transverse displacement) per Master Node, these depicted in 2.5. The total number of Master Nodes are 21, therefore 42 Master DOFs are included in the vector $\boldsymbol{Q}_{m,i}$ in Eq. 2.7.

$$\mathbf{M}_r\ddot{\boldsymbol{q}}_r + (\mathbf{C}_r + \Omega\mathbf{G}_r)\dot{\boldsymbol{q}}_r + \mathbf{K}_r\boldsymbol{q}_r = \boldsymbol{f}^B_{r,i} + \boldsymbol{f}^U_{r,i} + \boldsymbol{f}^G_{r,i} \tag{2.7}$$

The selection of master nodes has been performed according to the demand for master nodes in bearing locations and in unbalance planes (at least), where dynamic forces act. Further master nodes are added to match the dynamic response of the reduced system to that of the full system in terms of unbalance response, critical

[54] J. Guyan. "Reduction of stiffness and mass matrices". In: *AIAA Journal* 3 (1965), p. 380

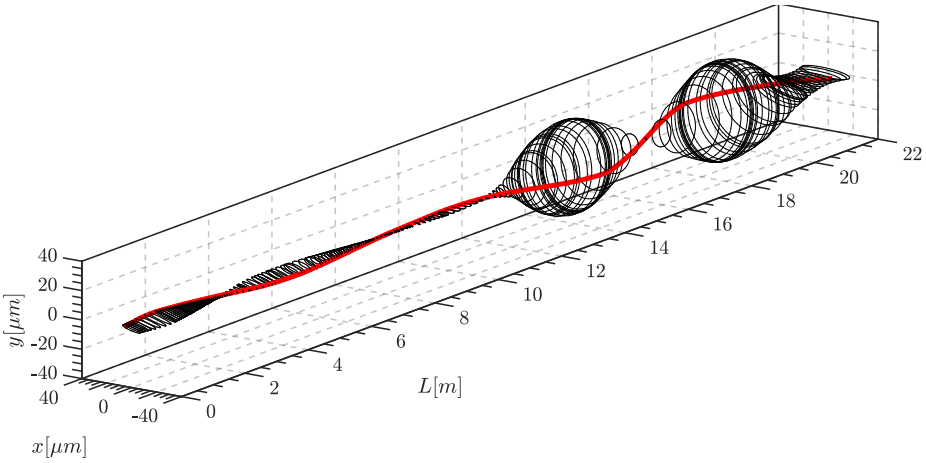

FIGURE 2.7: Harmonic response of the shaft-train at 3600RPM for G2.5 generator pair unbalance.

speeds and modal properties, while static performance (sag line) is absolutely satisfied. The performance of the reduced model is validated in Chapter 4. An overview of the Guyan reduction is given in Appendix B.

2.4 Bearing and Pedestal Modeling

The resulting bearing forces F_X^B, F_Y^B (fluid film forces) produced in each bearing and included in the system of ODEs are evaluated in this section.

The reader should bear in mind that the bearing impedance force nonlinearity (with respect to the journal kinematics) is the sole (and strong) source of nonlinearity in the ODE set. Pedestal properties retain their speed (frequency) dependent linear stiffness and damping characteristics, while the bearing forces are expressed in Equation 2.8 as nonlinear functions of the geometry and operating parameters (radial clearance c_r, journal Radius R, bearing width L, lubricant dynamic viscosity μ and Rotating speed Ω) (further variables such as pad clearance, offset, pad length etc. may be included according to the selected bearing type), pedestal motion (horizontal displacement x_P, vertical displacement y_P, horizontal velocity $\dot{x}_P$ and vertical velocity $\dot{y}_P$) and shaft motion (horizontal displacement x_i, vertical displacement y_i, horizontal velocity $\dot{x}_i$ and vertical velocity $\dot{y}_i$). Bearing forces in journal bearings of actively adjustable geometry (such as TJPBs) include also the independent variable of time t of which they are an explicit function.

$$\begin{Bmatrix} F_X^B \\ F_Y^B \end{Bmatrix} = \begin{bmatrix} f_1(c_r, R, L, \mu, \Omega, x_P, y_P, \dot{x}_P, \dot{y}_P, x_i, y_i, \dot{x}_i, \dot{y}_i) \\ f_2(\underbrace{c_r, R, L, \mu, \Omega}_{\substack{\text{geometry and} \\ \text{operation}}}, \underbrace{x_P, y_P, \dot{x}_P, \dot{y}_P}_{\text{pedestal motion}}, \underbrace{x_i, y_i, \dot{x}_i, \dot{y}_i}_{\text{shaft motion}}) \end{bmatrix} \tag{2.8}$$

Two bearing profiles are included in this study: the cylindrical partial arc bearing (Figure 2.8a) and the elliptical (lemon bore) bearing (Figure 2.8b), both being widely applied in industrial turbomachinery of medium speed, e.g. steam/gas turbines and generators [28].

[28] A. Chasalevris. "Stability and Hopf bifurcations in rotor- bearing-foundation systems of turbines and generators". In: *Tribology International* 145 (2020), p. 106154

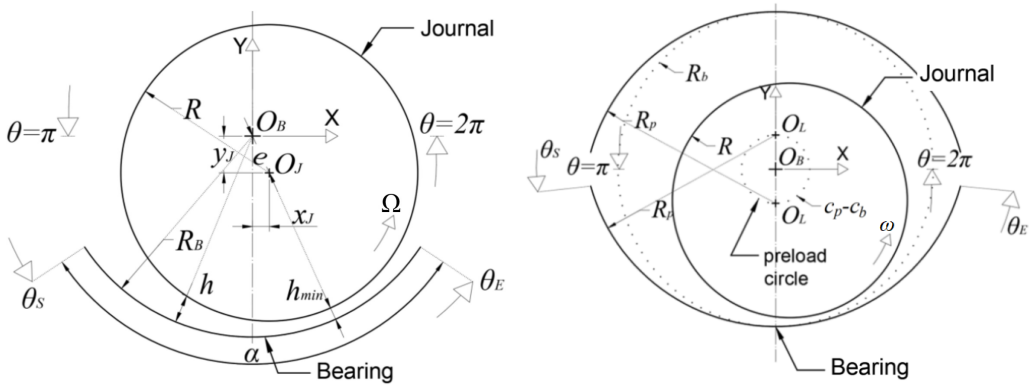

(A) (B)

FIGURE 2.8: Representation of configuration and of key design and operation parameters in 2.8a) a partial arc bearing and 2.8b) a 2-lobe elliptical bearing (lemon-bore bearing).

Key design parameters in both bearings are the starting angle θ_S, ending angle θ_E of the effective lubricating surface (bearing shell) at each bearing, the bearing length L_b and the journal diameter $D = 2R$.

The angle of the arc spanned by the two angle values is α. The arc angle usually receives values at the range of $60^\circ \leq \alpha \leq 140^\circ$ in common applications. Radial clearance is defined as $c_b = R_b - R$ at both types of bearings. At the lemon-bore bearing, a clearance $c_p = R_p - R$ is also defined to describe the curvature at each of the two lobes and the geometric preload $m = 1 - c_b/c_p$ which influences the effective eccentricity of the bearing and as a consequence the threshold speed of instability and the respective bifurcation type.

Geometric preload normally receives values in the range $0.3 \leq m \leq 0.7$. The offset β is an additional design parameter for this type of bearing and describes the horizontal displacement of the two bearing halves relative to each other. This parameter receives values of ca. $0.0 \leq \beta \leq 0.5c_b$ and then the bearing configuration belongs to the so called 'offset halves' bearing. A reference bearing design table for the geometric and physical properties is defined as shown in Table2.2.

TABLE 2.2: Reference Bearing Geometric and Physical parameters

Bearing no.	1	2	3	4	5
Journal Radius $R[mm]$	90	110	200	150	100
Length to Diameter Ratio L/D	0.5	0.9	0.9	0.9	0.5
Radial clearance c_r			0.002R		
Arclength $\alpha[^\circ]$	60	160	160	160	60
Geometric Preload m	-	0.5	0.5	0.5	-
Offset β	-	0	0	0	-
Dynamic viscosity (ISO VG46 @ 90°C) $\mu[Pa \cdot s]$			0.0067		

The calculation of oil film impedance forces generated in the mentioned bearing types relies on numerical solution (finite difference method) of the Reynolds equation for isothermal (isoviscous) flow with Constantinescu's turbulence model [55]

which is defined in Equation 2.9.

$$\frac{1}{\mu R^2}\frac{\partial}{\partial\theta}\left(h^3\frac{1}{k_x}\frac{\partial p}{\partial\theta}\right)+\frac{h^3}{\mu}\frac{\partial}{\partial z}\left(\frac{1}{k_z}\frac{\partial p}{\partial z}\right)=\frac{1}{2}\Omega\frac{\partial h}{\partial\theta}+\frac{\mathrm{d}h}{\mathrm{d}t} \tag{2.9}$$

Pressure distribution is defined as $p = p(\theta, z)$. The fluid film thickness function is defined in Equation 2.10 for the partial arc bearing as h. The lemon bore bearing consists of the upper and lower lobe, where the fluid film thickness is defined as h_u and h_l respectively, see Equation 2.10. The turbulence coefficients k_x, k_z can be calculated as $k_x = 12 + 0.53(k^2 Re_h)^{0.725}$, $k_z = 12 + 0.296(k^2 Re_h)^{0.65}$, $k = 0.125 Re_h$ where $Re_h = \rho\Omega R h/\mu$ is the local Reynolds number.

$$\begin{aligned} h &= c_b - x_J cos(\theta) - y_j sin(\theta), && \theta_S \leq \theta \leq \theta_E \\ h_u &= c_p - x_J cos(\theta) - (y_j - (-c_p + c_b))sin(\theta), && \theta_S - \pi \leq \theta \leq \theta_E - \pi \\ h_l &= c_p - x_J cos(\theta) - (y_j - (-c_p - c_b))sin(\theta), && \theta_S \leq \theta \leq \theta_E \end{aligned} \tag{2.10}$$

The fluid film thickness function $h = h(\theta)$ is defined only for positive values (no impact between rotor and stator is considered) where hydrodynamic lubrication regime (thin film lubrication) is established. This requires that $h > 0.15 c_r$ as the Reynolds equation should be considered valid for relative eccentricity values $0.15 < e/cr < 0.85$. The finite difference method applied for the numerical solution of the Reynolds equation requires the definition of the fluid film thickness function h in a mesh of $N_\theta \times N_z$ in circumferential and axial direction respectively. The fact that journal and bearing are considered aligned (no angular misalignment is considered) does not alter the fluid film function h in axial direction; therefore, h is a function of circumferential coordinate θ only. The sensitivity of the resulting pressure distribution in the mesh size has been studied to confirm that the dynamic characteristics of the system are repeated for different mesh grid sizes. The stability of numerical solution is also confirmed in the various grids checked. The finite difference solution scheme is given in Appendix C.

[55] V. N. Constantinescu. "On Turbulent Lubrication". In: *Proceedings of the Institution of Mechanical Engineers* 173.1 (1959), pp. 881–900

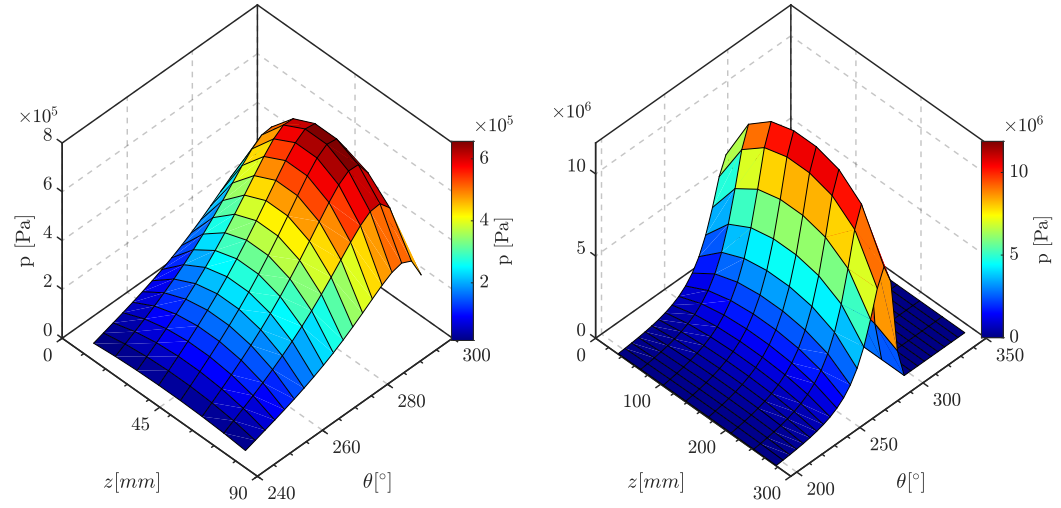

(A) Bearing #1

(B) Bearing #2 (lower half)

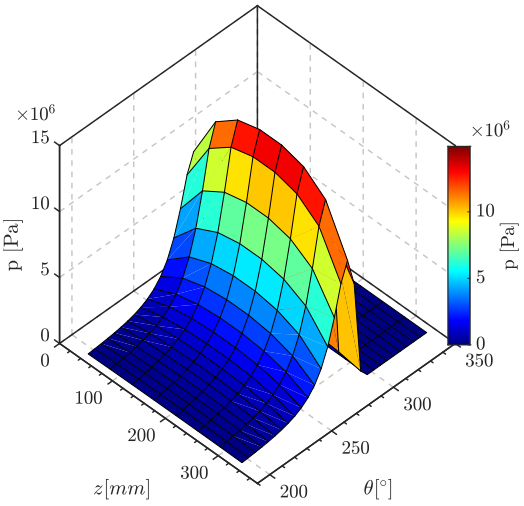

(C) Bearing #3 (lower half)

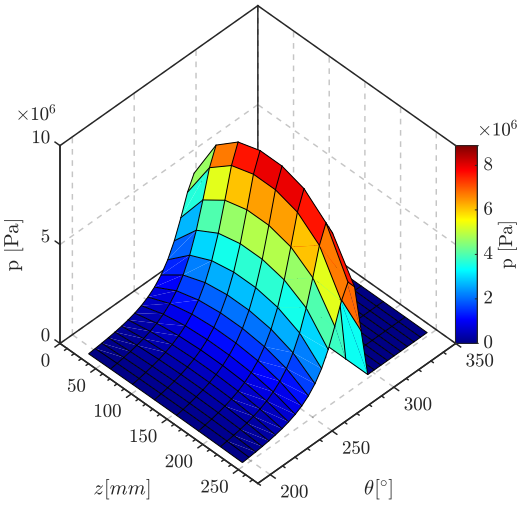

(D) Bearing #4 (lower half)

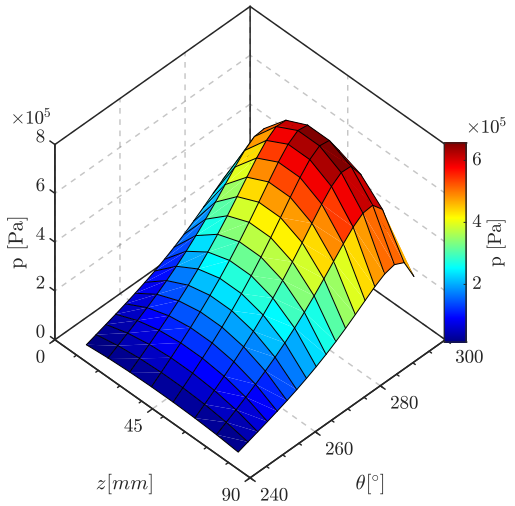

(E) Bearing #5

FIGURE 2.9: Pressure Distribution of Bearings 1-5 at Operating speed $\Omega = 3600$RPM for the balanced (*G*0) system. Finite difference grid $N_\theta \times N_z$ is equal to 20×9 for bearings #1 and #5 (partial-arc) and 30×9 for bearings #2, #3 and #4 (lemon-bore) bearings. For the lemon-bore bearings, only the lower halves are depicted.

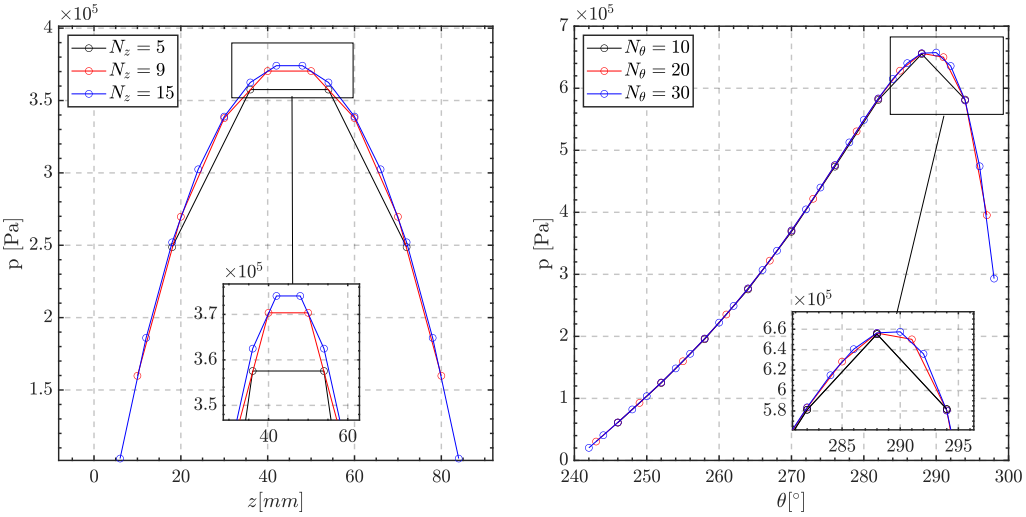

(A) Bearing #1 section of pressure profile at bearing axial centerline

(B) Bearing #1 section of pressure profile at bearing circumferential centerline

FIGURE 2.10: Pressure distribution for various grid sizes in axial (A) and circumferential (B) direction. $N_\theta = 20$ for (A) and $N_z = 9$ for (B). Operating conditions same as Fig. 2.9.

The fluid film impedance forces in horizontal and vertical direction F_X^B, F_Y^B are evaluated numerically in Equation 2.11 for the partial arc bearing and in Equation 2.12 for the lemon-bore bearing, after the pressure distribution $p(\theta, z)$ is defined, and considering only the positive pressure values. In the lemon bore bearing where two bearing pads are considered, $p_u(\theta, z)$ is the pressure distribution for the upper pad and p_l is the pressure distribution for the lower pad. Therefore, the Reynolds equation is solved two times in the case of a lemon bore bearing.

$$\begin{Bmatrix} F_X^B \\ F_Y^B \end{Bmatrix} = \int_{\theta_S}^{\theta_E} \int_{-L_b/2}^{L_b/2} p(\theta, z) R \begin{Bmatrix} cos(\theta) \\ sin(\theta) \end{Bmatrix} dz d\theta \tag{2.11}$$

$$\begin{aligned} \begin{Bmatrix} F_X^B \\ F_Y^B \end{Bmatrix} = & \int_{\theta_S - \pi}^{\theta_E - \pi} \int_{-L_b/2}^{L_b/2} p_u(\theta, z) R \begin{Bmatrix} cos(\theta) \\ sin(\theta) \end{Bmatrix} dz d\theta \\ & + \int_{\theta_S}^{\theta_E} \int_{-L_b/2}^{L_b/2} p_l(\theta, z) R \begin{Bmatrix} cos(\theta) \\ sin(\theta) \end{Bmatrix} dz d\theta \end{aligned} \tag{2.12}$$

When numerical solutions are applied in the Reynolds equation, a variety of different boundary conditions can be implemented in the lubrication problem, with the most applicable being these defined by Elrod [56], Jakobson and Floberg [57] (or JFO for simplicity), Stieber [58] and Gümbel [59] (or half-Sommerfeld). There are cases of operating conditions where the selection of a boundary condition is not critical for the rotor dynamic design of a specific application. In the scope of this work,

[56] H. Elrod. "A Cavitation Algorithm". In: *Journal of Lubrication Technology* 103.3 (1981), pp. 350–354

[57] B. Jakobson and L. Floberg. "The finite journal bearing considering vaporization". In: *Transactions of Chalmers University Technology, Goteborg, Sweden* 190.190 (1957), pp. 1–119

[58] W. Stieber. *Das Schwimmlager: Hydrodynamische Theorie des Gleitlagers*. V.D.I. Verlag GMBH, Berlin 106, 1933

[59] L. Gümbel. *Das Problem der Lagerreibung*. Mon. Berl. Bezirksverein.,V.D.I., 5, 1914, 87104 and 109–120

the Gümbel boundary condition is applied for computational effectiveness (reduced evaluation time). Pressure distribution is considered only in the convergent region of the bearing (the wedge between the journal and the bearing, for static conditions), while the rest area of the bearing pad is considered to experience cavitation (and assumption of oil film rupture).

Each bearing of the shaft train fits in its bearing housing (pedestal) whose model follows a simplistic (but still effective) approach to introduce the influence of foundation flexibility in the dynamics of the shaft train. Bearing pedestal motion is modeled with 1 DoF per direction mass-spring-damper system, see Figure 2.11. The respective mass, stiffness and damping properties ($M_{P,X}, M_{P,Y}, K_{P,X}, K_{P,Y}, C_{P,X}, C_{P,Y}$) are selected such that modal properties of pedestals (natural frequencies and damping ratio) are close to those obtained from real pedestal structures (for a selected natural frequency close to the operating speed). Pedestal properties are included in the case study presented in Chapter 4. The reference pedestal mass, stiffness and damping coefficients are shown below, see Table 2.3.

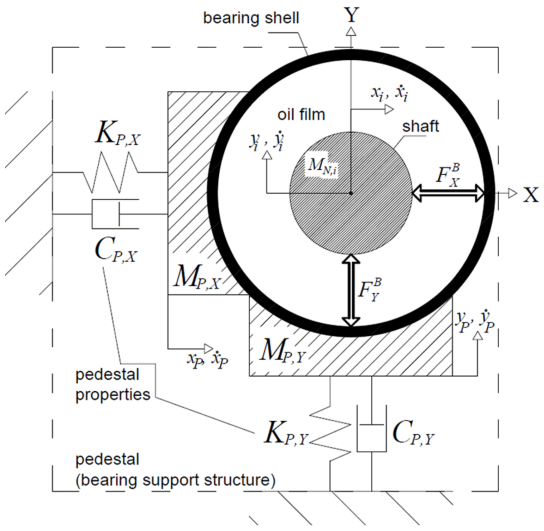

FIGURE 2.11: Representation of the simplified bearing pedestal model with 1 DoF per direction [28][2]

TABLE 2.3: Pedestal properties.

Pedestal no.		1	2	3	4	5
Mass $M_P[kg]$		10^4	10^4	$6 \cdot 10^3$	$3.8 \cdot 10^3$	10^3
Stiffness $K_P[N/m]$	x	$5 \cdot 10^9$	$5 \cdot 10^9$	$5 \cdot 10^9$	$2 \cdot 10^9$	$0.67 \cdot 10^9$
	y	$6.7 \cdot 10^9$	$6.7 \cdot 10^9$	$6.7 \cdot 10^9$	$5 \cdot 10^9$	$2 \cdot 10^9$
Damping $C_P[N \cdot s/m]$	x	$7.1 \cdot 10^5$	$7.1 \cdot 10^5$	$5.9 \cdot 10^5$	$2.8 \cdot 10^5$	$0.82 \cdot 10^5$
	y	$4.9 \cdot 10^5$	$4.9 \cdot 10^5$	$3.8 \cdot 10^5$	$2.6 \cdot 10^5$	$0.85 \cdot 10^5$

2.5 Formulation of the ODE system

The coupled reduced rotor and pedestal motion equations (of 2^{nd} order) are then converted to a 1^{st} order ODE set applying the transformations of Eq. 2.13, known as Duncan method.

$$\boldsymbol{x} = \begin{Bmatrix} \boldsymbol{q} \\ \dot{\boldsymbol{q}} \end{Bmatrix} \tag{2.13}$$

The combined reduced rotor model and the pedestal model are then written in Eq. 2.14 and the force vector appearing are defined in Eq. 2.15.

$$\dot{\boldsymbol{x}} = \begin{bmatrix} \mathbf{0} & \mathbf{I} \\ -\mathbf{M}^{-1}\mathbf{K} & -\mathbf{M}^{-1}(\Omega\mathbf{G} + \mathbf{C}) \end{bmatrix} \boldsymbol{x} + \begin{Bmatrix} \mathbf{0} \\ \mathbf{M}^{-1}\boldsymbol{f}_{r,i} \end{Bmatrix} \tag{2.14}$$

$$\boldsymbol{f}_{r,i} = \boldsymbol{f}^{B}_{r,i} + \boldsymbol{f}^{U}_{r,i} + \boldsymbol{f}^{G}_{r,i} \tag{2.15}$$

The coupled ODE set is a nonlinear autonomous ODE system when unbalance force vectors are zero ($e_u = 0$). Then, time t does not appear explicitly in the motion equations (Eq. 2.14). Unbalance force formulas for $e_u \neq 0$ are the unique reason for time t to appear explicitly in Eq. 2.14 and then the system is characterized non-autonomous. As the methods discussed in Chapter 3 and Appendix D for numerical continuation of periodic solutions cannot handle non-autonomous ODE systems [38], Eq. 2.14 has to be converted to autonomous. This is achieved by coupling the ODE system of Eq. 2.14 with a two DoF oscillator, see Eqs. 2.16a and 2.16b, whose unique solution is a harmonic motion of frequency Ω, see Eq. 2.17 [38].

$$\dot{y}_1 = y_1 + \Omega y_2 - y_1(y_1^2 + y_2^2) \tag{2.16a}$$

$$\dot{y}_2 = -\Omega y_1 + y_2 - y_2 y_1^2 + y_2^2) \tag{2.16b}$$

$$y_1 = cos(\Omega t), \quad y_2 = sin(\Omega t) \tag{2.17}$$

The final autonomous ODE system is of size $n = 2 \times N_r + 10 + 2$ (N_r is the number of the reduced rotor DOFs plus 10 pedestal DOFs (vertical and horizontal for 5 Pedestals) plus the two DoF simple oscillator of Eq. 2.17) and is defined in Eq. 2.18 and the unbalance forces to be defined for constant rotating speed, in Eq. 2.19.

$$\dot{\boldsymbol{x}} = \boldsymbol{f}(\boldsymbol{x}, \Omega) \tag{2.18}$$

$$f^{U}_{i,X} = M_{(k)} e_u \Omega^2 y_1, \quad f^{U}_{i,Y} = M_{(k)} e_u \Omega^2 y_2 \tag{2.19}$$

Chapter 3

Evaluation of Limit Cycles and Bifurcation Sets

In this chapter, the methods for the evaluation of periodic limit cycles with numerical continuation (or path following methods) along the independent parameter of rotating speed, their stability characteristics and detection of local bifurcations of periodic solutions using Floquet Theory are briefly presented. In addition, a brief overview of well established methods for characterizing motions from simulated or experimental time history (signal) data is given, namely Fourier or frequency spectra, Poincaré maps and Lyapunov Exponents.

3.1 Numerical Continuation of Limit Cycles

Numerical continuation refers to a class of methods for computing approximate solutions to a system of parameterized nonlinear equations $\boldsymbol{F}(\boldsymbol{x}, \lambda) = 0$ where one or more scalar parameters appears explicitly in the system of equations. The solution $\boldsymbol{x}$ can be time independent (stationary solution or fixed point or equilibrium or steady state) or time dependent (dynamic solution). A numerical continuation algorithm takes as input a system of parameterized nonlinear equations $\boldsymbol{F}(\boldsymbol{x}, \lambda) = 0$ and an initial solution $(\boldsymbol{x}_0, \lambda_0)$ and produces a set of solutions $[(\boldsymbol{x}_1, \lambda_1), (\boldsymbol{x}_2, \lambda_2), \ldots (\boldsymbol{x}_k, \lambda_k])$ which satisfy the system of nonlinear equations and are continuously connected to the initial solution $(\boldsymbol{x}_0, \lambda_0)$ by a path of solutions $(\boldsymbol{x}(s), \lambda(s))$ (also called solution branch). In the problem studied in this work the sole bifurcation parameter used is the rotating speed Ω and only codimension-1 bifurcations are considered (bifurcations encountered by varying one parameter).

Numerical continuation has been extensively used to study parameterized autonomous nonlinear dynamical systems of the form $\dot{\boldsymbol{x}} = \boldsymbol{f}(\boldsymbol{x}, \lambda)$. Since time is not explicitly included in the system of equations as a variable but the solutions $\boldsymbol{x}$ can be time-dependent $\boldsymbol{x} = \boldsymbol{x}(t)$, it is possible to construct solutions with certain characteristics (e.g. periodicity) without the need of a time transient simulation from an initial (in time) solution, provided there is a good enough guess for the solution (prediction) so that an acceptable approximation can be numerically calculated (correction). In this sense, numerical continuation belongs to a wider class of algorithms (predictor-corrector methods) designed to integrate ordinary differential equations. Numerical continuation algorithms are then classified based on the predictor and corrector steps. The same principles of continuation hold for various types of solutions (fixed point, periodic, quasi-periodic) provided the "zero problem" $\boldsymbol{F}(\boldsymbol{x}, \lambda) = 0$ is well posed. In this work, numerical continuation is performed for fixed point and periodic solutions using pseudo-arclength continuation.

The simplest form of continuation is what is called natural parameter continuation (or sequential continuation) where the solution at one value of λ is used as the initial guess for the solution at $\lambda + \Delta\lambda$. One advantage of this type of continuation is that it does not require an explicit formula for the "zero problem" $\boldsymbol{F}(\boldsymbol{x}, \lambda) = 0$ (equation-free or black box models) and only requires the previous solution $(\boldsymbol{x}_0, \lambda_0)$ and the function evaluation $\boldsymbol{F}(\boldsymbol{x}, \lambda)$. However, natural parameter continuation fails at turning points (fold bifurcation or limit point of cycles), where the sign of $\Delta\lambda$ changes between steps. The sign of $\Delta\lambda$ can be manually changed at the turning point but it is possible that the solution will converge to the previously computed solutions. One method to remedy this is to temporarily swap the continuation parameter λ with one of the states of the solution vector x_i. Another method is to modify the original system using a deflation operator and update it after a new solution is found. If we define the deflation operator as

$$D(\boldsymbol{x}, \lambda) = \prod_{i=1}^{p} ||(\boldsymbol{x}, \lambda) - (\boldsymbol{x}_i, \lambda_i)|| \tag{3.1}$$

where $i = 1, 2, \ldots, p$ are the previously found solutions of $\boldsymbol{F}(\boldsymbol{x}, \lambda) = 0$ then the modified (deflated) function $\hat{\boldsymbol{F}}(\boldsymbol{x}, \lambda) = \boldsymbol{F}(\boldsymbol{x}, \lambda)/D(\boldsymbol{x}, \lambda)$ has all of the same roots as the original function with the exception that roots that have already been located no longer are roots of the deflated function.

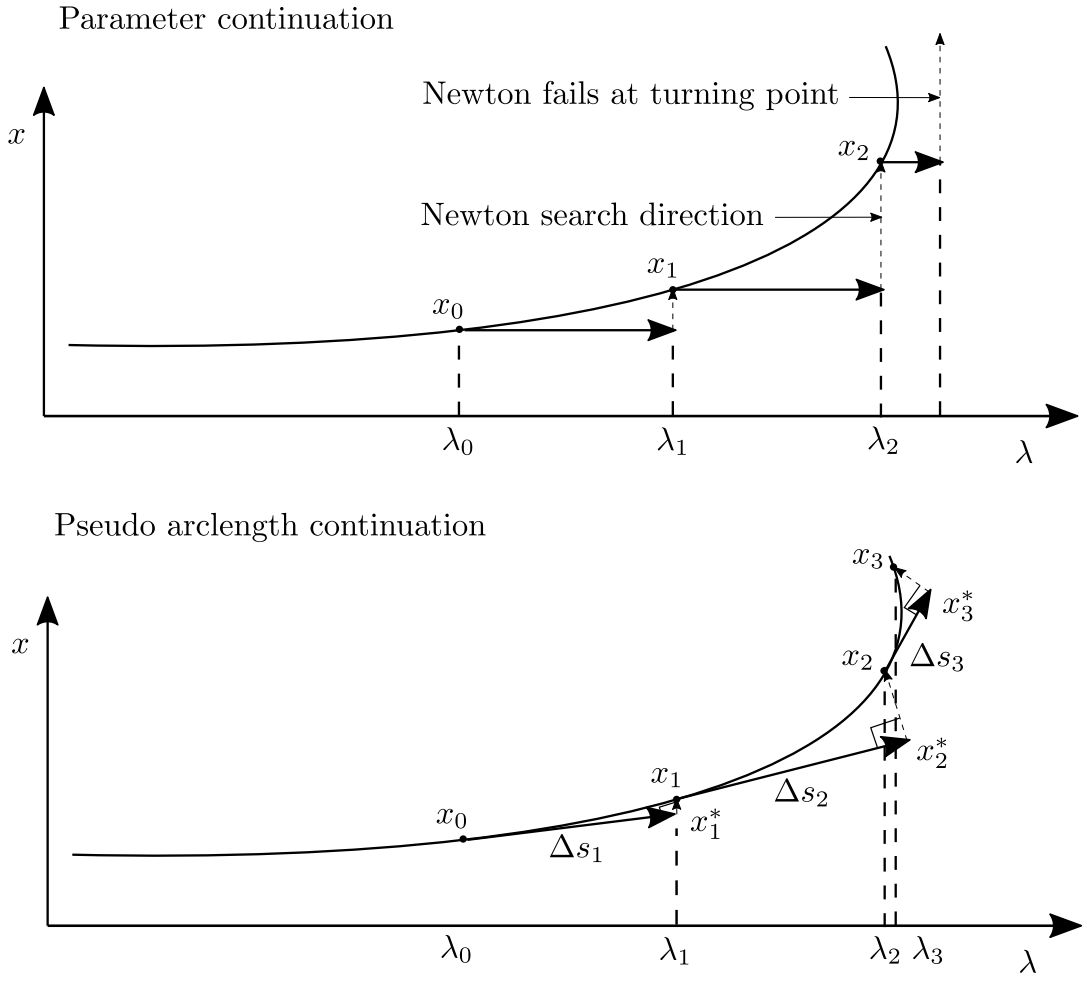

FIGURE 3.1: Parameter and Pseudo arclength continuation.

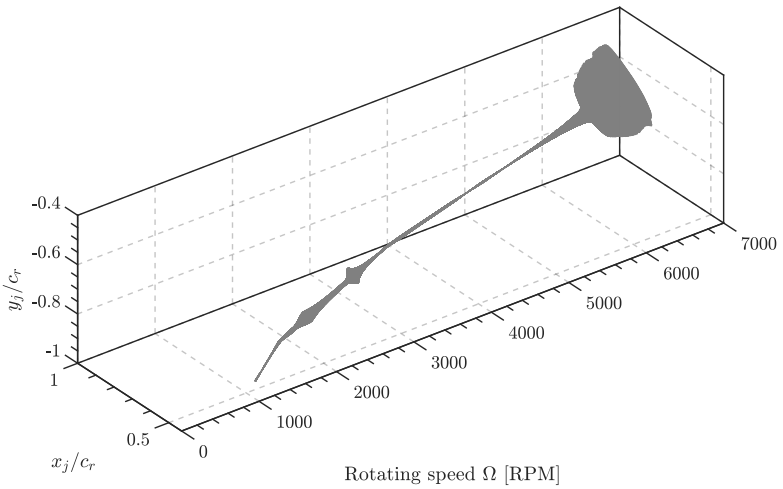

(A) Journal displacement of bearing #3 for time transient simulation of a runup with *G*2.5 pair unbalance in GEN rotor.

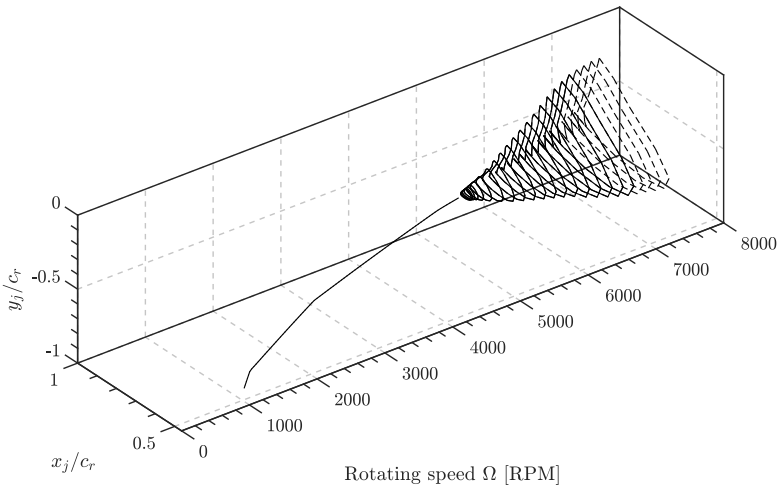

(B) Solution branches of bearing #4 for *G*0 unbalance (autonomous system)

.

FIGURE 3.2: Time transient simulation of runup (A) and continuation of fixed points and limit cycles (B).

Another widely applied method of continuation and the one used in this work is pseudo-arclength continuation. This method introduces a separate independent parameter (the arclength) s and produces an initial guess for the next step in the tangential direction at the current solution step. This enables the method to continue the solution branch at turning points for the parameter λ and can make larger steps at regions of high curvature, resulting in better computational efficiency. Then the parameter λ becomes part of the new solution vector $\boldsymbol{u} = (\boldsymbol{x}, \lambda)$ and an additional equation is required to close the system

$$\begin{aligned} \boldsymbol{F}(\boldsymbol{x},\lambda) &= 0 \\ \boldsymbol{x}_0'(\boldsymbol{x}-\boldsymbol{x}_0)+\lambda_0'(\lambda-\lambda_0) &= \Delta s \end{aligned} \tag{3.2}$$

where $(\boldsymbol{x}_0', \lambda_0')$ is the tangent vector at $(\boldsymbol{x}_0, \lambda_0)$. The prediction $(\boldsymbol{x}^*, \lambda^*)$ to the next solution is tangent to the previous solution so $\boldsymbol{x}^* = \boldsymbol{x}_0 + \boldsymbol{x}_0'\Delta s, \quad \lambda^* = \lambda_0 + \lambda_0'\Delta s$. Using this prediction the corrector step can be used (usually some variant of Newton's method) to solve the nonlinear system.

In the case of periodic solutions, the solution trajectory has to be discretized in time. Various methods to discretize in time can be used such as shooting methods, finite difference methods and orthogonal collocation which is implemented in this work. The scheme for pseudo arclength continuation of periodic solutions with orthogonal collocation is outlined in Appendix D.

3.2 Stability and Bifurcations of Limit Cycles

To assess the stability properties of a periodic solution $\boldsymbol{x} = \boldsymbol{x}(t)$ with $\boldsymbol{x}(t) = \boldsymbol{x}(t+T)$ the fundamental matrix solution $\Phi(t+T, t)$ which satisfies

$$\dot{\Phi}(t+T,t) = T\boldsymbol{f}(\boldsymbol{x},\lambda)\Phi(t+T,t), \quad \Phi(0) = \mathbf{I}, \quad t \in [0,1] \tag{3.3}$$

This matrix $\Phi(t+T, t)$ is called the monodromy matrix and its eigenvalues μ_i are known as Floquet multipliers. The monodromy matrix maps a point $\boldsymbol{x}(t_0)$ on the periodic solution to the response $\boldsymbol{x}(t_0+T)$ at time T (one period) later.

$$\boldsymbol{x}(t_0+T) = \Phi(t_0+T, t_0)\boldsymbol{x}(t_0) \tag{3.4}$$

The Floquet multipliers μ_i indicate the stability and detect the type of bifurcation as shown below.

When $|\mu_i| < 1$ for all i, the periodic solution is asymptotically stable. These types of solutions can also be approximated by integrating the ODE system for a sufficient amount of time but this can be a slow process. By discretizing the periodic orbit, a solution can be computed at least an order of magnitude faster as shown in Chapter 4 at any given parameter value, provided the periodic solution is stable and the initial guess lies in the region of convergence for the Newton scheme of choice. This process can be further accelerated by parallelizing the calculation of the Jacobian. The initial guess can be calculated by integrating the ODEs for a smaller amount of time (this depends heavily on the damping characteristics of the system) or by using analytical approximations for example if a fixed point undergoes a Hopf bifurcation and a periodic solution of small amplitude emanates.

When $|\mu_i| > 1$, the periodic solution is asymptotically unstable. Since these solutions are repelling they can only be calculated by discretizing the orbit and not by numerical integration and with a good enough initial guess which can either be provided analytically or by numerical continuation.

When $|\mu_i| = 1$, the periodic solution is marginally stable and some type of bifurcation occurs. The type of bifurcation depends on the position that one or a pair of complex conjugate floquet multipliers, leave the unit circle as shown in Fig. 3.3.

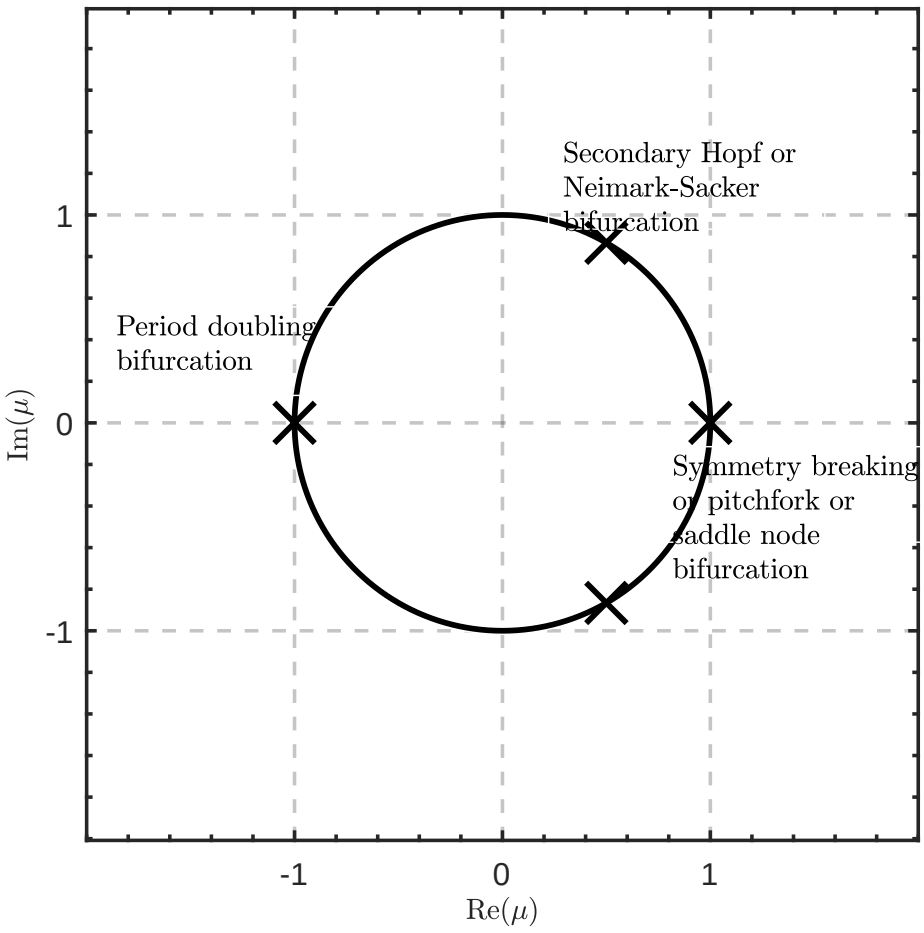

FIGURE 3.3: Floquet multipliers for various types of bifurcations

3.3 Tools for Assessment of Motions

The numerical scheme for numerical continuation of periodic solutions for ODEs can reveal the existence of different types of solutions, e.g. quasiperiodic through a Neimark-Sacker bifurcation which is extensively encountered in Chapter 4. Quasiperiodic and chaotic solutions cannot be evaluated with this process therefore, other tools must be employed to characterize these motions.

3.3.1 Fourier Spectra

The Fourier or frequency spectra can help characterize motions as periodic, quasiperiodic and chaotic. If the frequency spectrum of a stationary signal $\boldsymbol{x}(t)$ contains peaks at one fundamental frequency ω and none, one or more of its harmonics $2\omega, 3\omega, \ldots$. In practice, the period T of the signal may not be known so the time length of the data is not an exact multiple of the period. Then the FFT will consist of large amplitude peaks at the fundamental frequency and its harmonics surrounded by smaller amplitude peaks, also called sidelobes. This phenomenon is called leakage and can be remedied by using weighting functions in the time domain (windows).

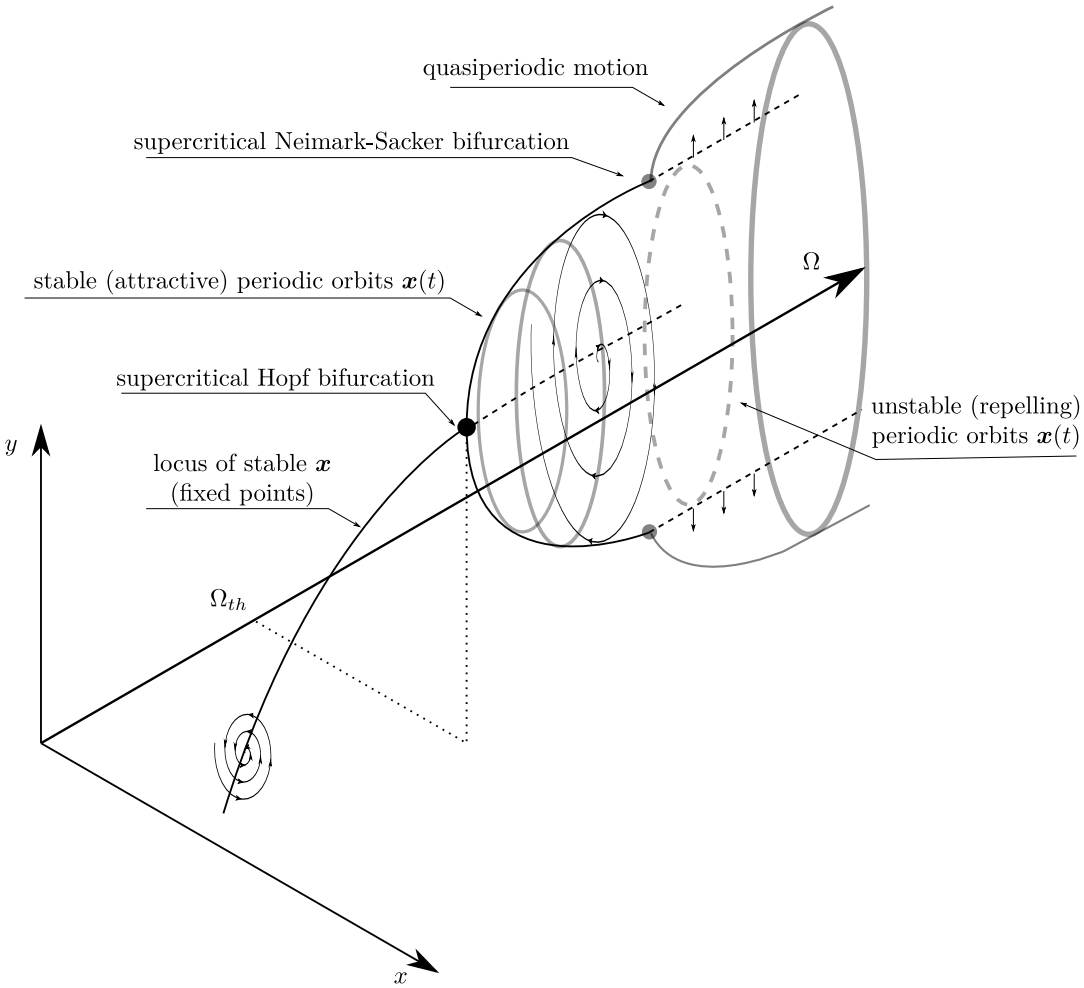

FIGURE 3.4: Representation of supercritical bifurcations in autonomous systems.

If the frequency spectrum contains peaks at two or more incommensurate frequencies $(\omega_1, \omega_2, \ldots, \omega_k$, that is $\omega_i/\omega_j, i, j = 1, 2, \ldots, p, i \neq j$ is irrational, and multiples of them then the motion is called k-period quasiperiodic. When the frequency spectrum is broadband then the motion is chaotic.

3.3.2 Poincare Maps

Another tool to analyze motions is the Poincaré section or map. If the period T of a signal $\boldsymbol{x}(t)$ is known then the Poincaré map is a collection of the points

$$\{\boldsymbol{x}(t_0 + T), \boldsymbol{x}(t_0 + 2T), \ldots, \boldsymbol{x}(t_0 + mT)\}$$

where m is an integer. In this case the Poincaré map of a periodic signal is either a single point or a set of k discrete points, in which case the period is kT. For a 2-period quasiperiodic signal the Poincaré map will form a closed smooth curve however for 3 or higher period quasiperiodic or chaotic motions there is no simple geometric shape that is depicted. The Poincaré map of chaotic motions will appear as a cloud of points with no or some structure depending on the damping characteristics of the system.

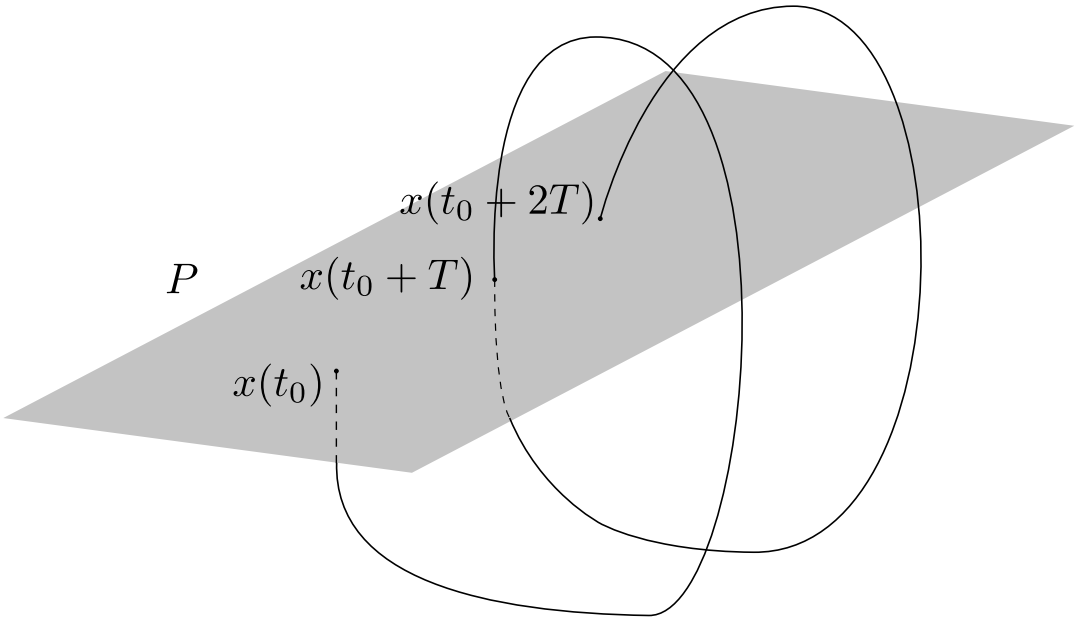

FIGURE 3.5: Representation of a Poincare Map with Period T

3.3.3 Lyapunov Exponents

The Lyapunov exponents describe the exponential rate of separation from an initial state. It can be considered a generalization of the floquet multipliers in that they are characteristic quantities that can characterize any type of motion (fixed point, periodic, quasiperiodic, chaotic). The maximal Lyapunov exponent of a trajectory is defined as

$$\bar{\lambda}_i = \lim_{t \to \infty} \frac{1}{t} \ln \left(\frac{||x(t)||}{||x(0)||} \right) \tag{3.5}$$

For an n-dimensional state space there are n Lyapunov exponents which are independent on the choice of basis. This set of n Lyapunov exponents is called the Lyapunov spectrum and can characterize the motion as follows. If all Lyapunov exponents are negative, the attractor is a stable fixed point. If one of the Lyapunov exponents is zero and all others negative, the attractor is a stable periodic limit cycle. If m Lyapunov exponents are zero and the others are negative, the attractor is m-periodic quasiperiodic. If one or more Lyapunov exponents is positive, the attractor is chaotic.

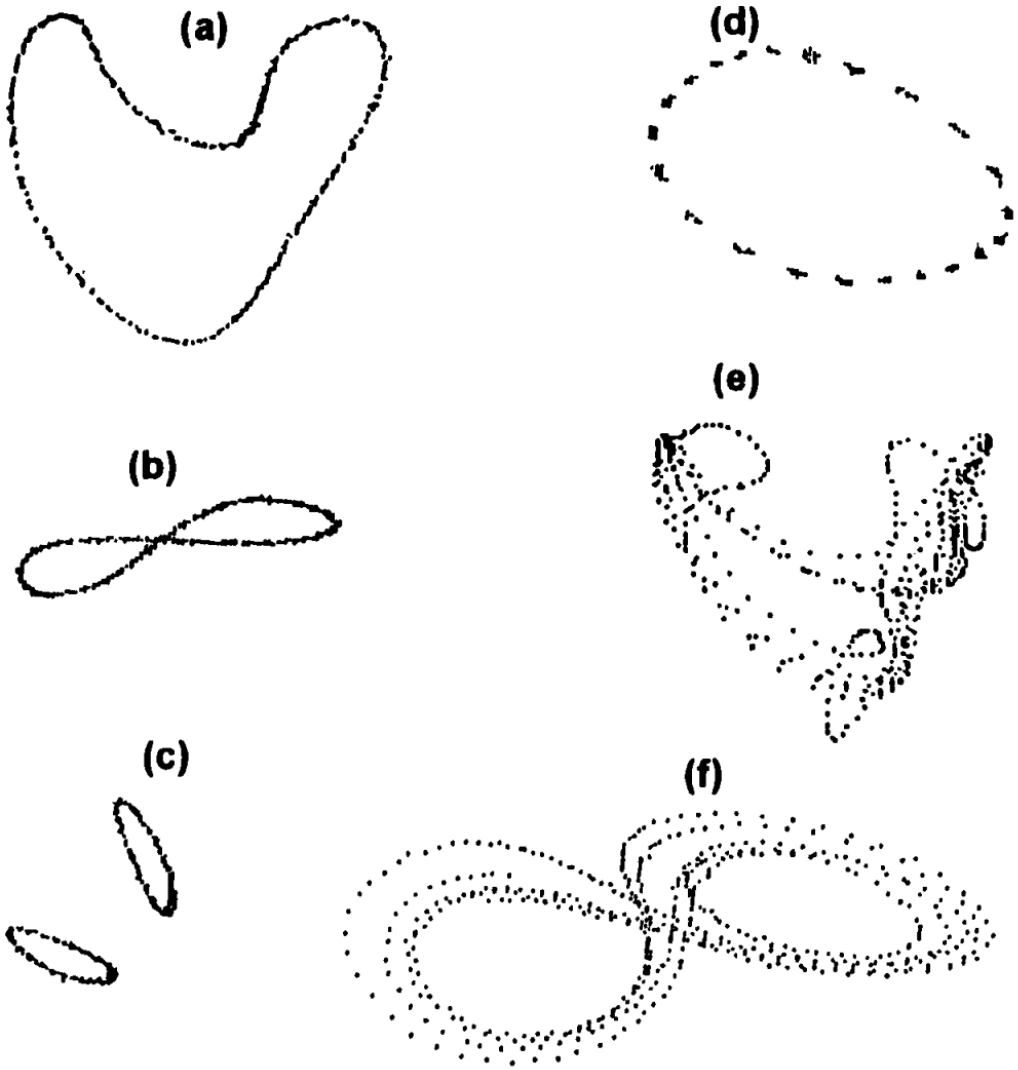

FIGURE 3.6: A collection of experimentally obtained Poincaré sections: (a)-(c) quasiperiodic motions, (d) phase-locked motion, (e), (f) chaotic motions [30].

Chapter 4

Results and Discussion

In this chapter, several results obtained are presented and commented on concerning the bifurcation sets of the reduced turbine-generator shaft train, the limit cycles, their stability and showcasing the existence of quasiperiodic and chaotic motions. Alternative scenarios are considered for the pedestal properties, the geometric and physical characteristics of the bearings and rotor slenderness.

All calculations were performed on a desktop PC with an Intel i7 6700K processor and 16GB of RAM using MATLAB R2021a. For the numerical integration of the ODE system the MATLAB ode15s ODE solver was used. For the solution of linear systems of equations, the MATLAB mldivide function (or $\backslash$ operator) was used. For the solution of eigenvalue problems, the MATLAB function eig was used.

The nonlinear dynamic system of the turbine-generator shaft train is first validated on its dynamic characteristics.

In Fig. 4.1 it is shown that the reduced model depicts very similar (if not identical) modal parameter of stability (stability factor v is directly related to the logarithmic decrement δ). The nonlinear model (still linearized around a fixed point though) depicts similar but not identical at all cases stability factor compared to the full linear system. The complex eigenvalues of the nonlinear reduced system have been evaluated for several perturbations around the fixed point (sensitivity analysis). The small differences in the stability factor appear due to the slightly different bearing coefficients that are effectively taking place in the nonlinear system (when linearized around equilibrium). In Fig. 4.2 the reduced nonlinear model is validated on unbalance response. The unbalance case considers pair unbalance $G2.5$ in generator rotor. Resonance frequencies are identical among the three models, while resonance amplitudes appear very similar. All bearings appear with similar unbalance response comparing the three models, at both horizontal and vertical plane. The unbalance response of the reduced nonlinear system is evaluated with time integration of the motion equations for a run-up of the system with low rotating acceleration.

4.1 Bifurcation set of the reference design

The stability of the whirling motions of the reduced nonlinear system is investigated for the reference design in this section. Applying numerical continuation of limit cycles in the non-autonomous (unbalanced) system, the response envelop of limit cycles is depicted in Fig. 4.2b together with the respective transient response of the system obtained for a run-up with low rotating acceleration (depicted) on its unbalance response, also in Fig. 4.2a. In Fig. 4.2b one may notice the unstable motion of the shaft-train when rotating speed exceeds $\Omega = 6000$RPM, where a Neimark-Sacker bifurcation takes place (see transient response in Fig. 4.2b). The system is not globally unstable as stable quasi periodic limit cycles are produced after the Neimark-Sacker bifurcation (supercritical Neimark-Sacker). However, the motion

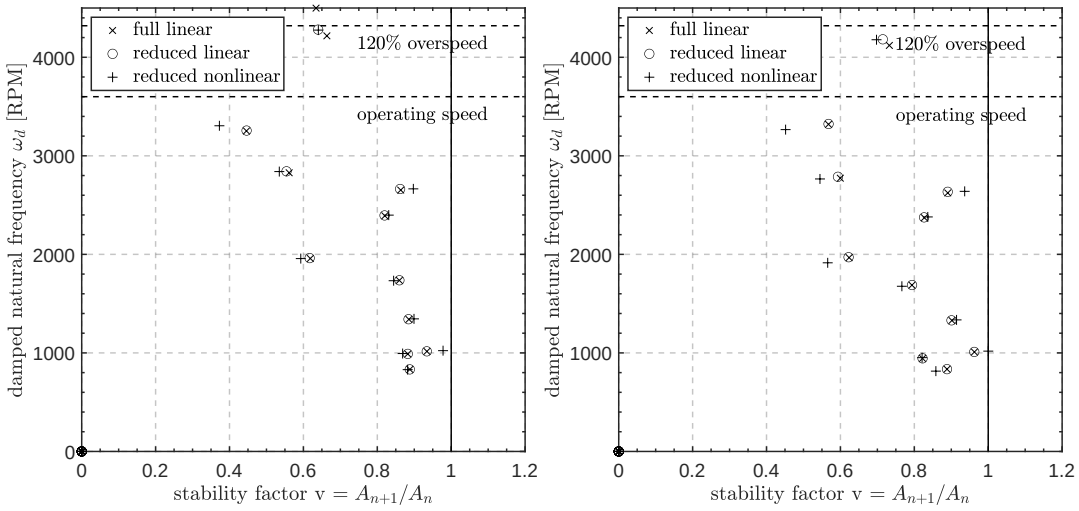

(A) Ω = 3600 RPM (B) Ω = 4500 RPM

FIGURE 4.1: Stability factor $v = 10^{-\delta}$ of the lateral (bending) modes of the system when operating at $\Omega_r = 3600$ RPM and 4500 RPM when the nonlinear reduced system is marginally stable. Modes with damped natural frequency $\omega_d < 10000$ RPM are depicted only. Unstable system when $v > 1$

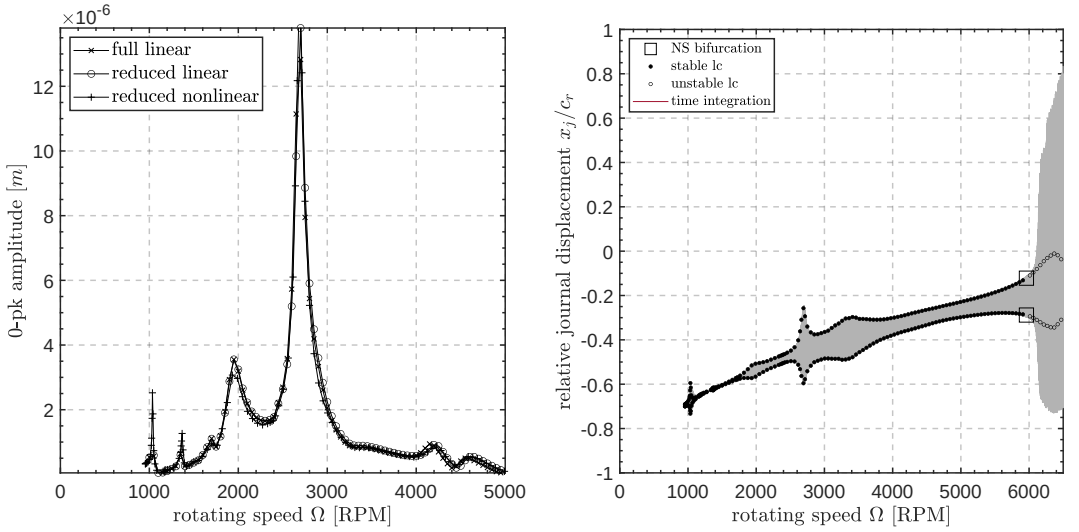

(A) Bearing #3 absolute journal response in vertical direction (B) Bearing #5 relative journal response evelope in vertical direction

FIGURE 4.2: Unbalance response (absolute) with pair unbalance *G*2.5 in generator rotor

is quasi-periodic and collocation method cannot evaluate such limit cycle motions. The evaluation of transient response is interrupted at an indicative rotating speed.

The rotating speed of Ω = 6000RPM is out of the operating range of the system and may sound out of interest. However, there are turbine sets operating at higher speeds (even higher than Ω = 6000) including slender rotors on bearings of lemon bore profile (tilting pad bearings are rather preferred in those cases).

In Fig. 4.3a, the balanced system (*G*0) loses fixed point stability at c.a. Ω = 5000RPM through a supercritical Hopf bifurcation and stable limit cycles (self-excited

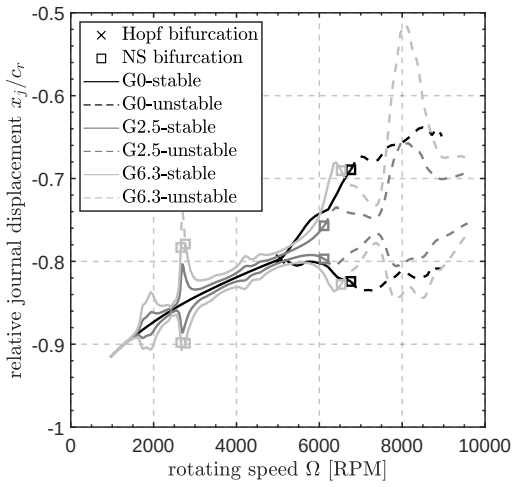

(A) Bearing #3 relative journal response in vertical direction.

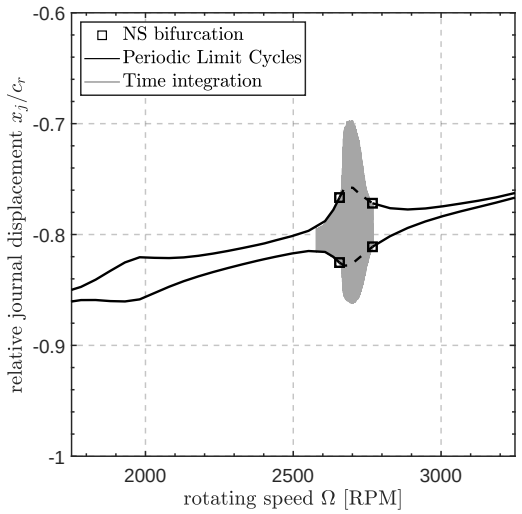

(B) Bearing #3 relative journal response in the region of the major critical speed for *G*6.3 unbalance.

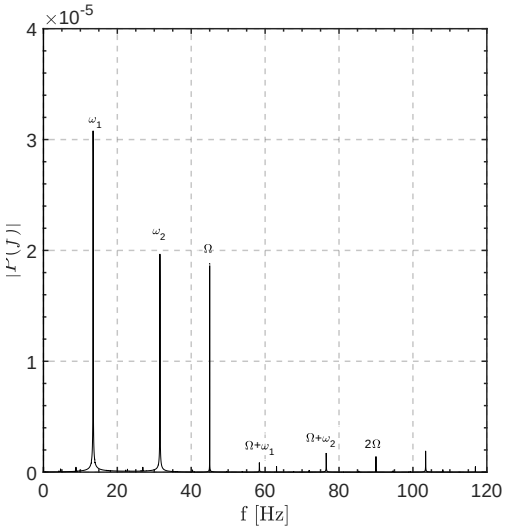

(C) Bearing #3 PSD of the quasi periodic attractor at 2700 RPM.

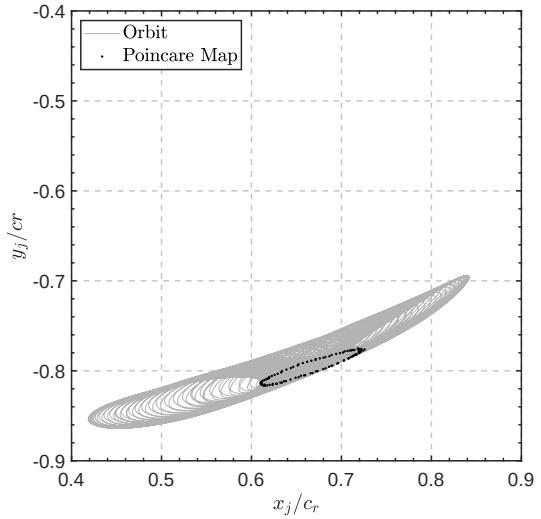

(D) Bearing #3 relative journal orbit and Poincaré Map using the forcing frequency.

FIGURE 4.3: Reference system response for *G*0 (autonomous system) and *G*2.5, *G*6.3 (non-autonomous system) pair unbalance in generator.

motion) are generated. Increasing speed further at $\Omega = 6750$ RPM, the stable limit cycles lose stability through a subcritical Neimark-Sacker bifurcation and unstable limit cycles (depicted with dashed lines) are generated. The instability is not global, as there are no stable manifolds (quasiperiodic or chaotic) on the outside of the repelling periodic limit cycles. In the same graph, the case of *G*2.5 is identical to this already discussed in Fig. 4.2b.

The most interesting case is that of *G*6.3 where stable limit cycles lose stability inside the range of operating speed (c.a. $\Omega = 2700$RPM) where the 2^{nd} critical speed of generator rotor exists. In this case, the instability is not global, still. Stable limit cycles (self-excited vibrations) are generated as the system experiences the first Neimark-Sacker bifurcation, these evaluated only by time integration in Fig. 4.3b. The system experiences another Neimark-Sacker bifurcation at slightly higher speed

(c.a. $\Omega = 2800$RPM) and returns to the former limit cycle motion (that corresponding to the elastic response). In Fig. 4.3c, 4.3d the quasi periodic attractor is validated using frequency spectra and the Poincaré Map.

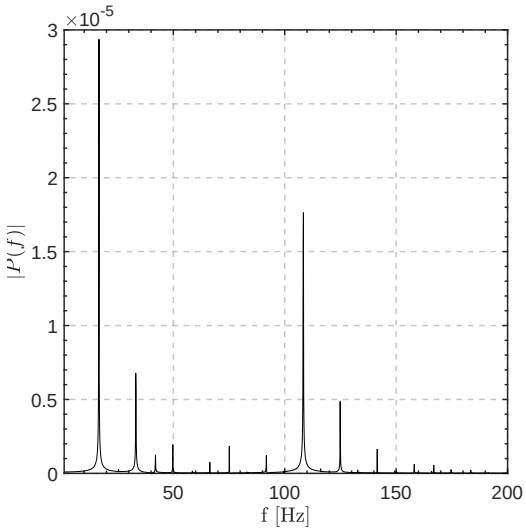

(A) Bearing #3 PSD of the quasi periodic attractor at 6500 RPM.

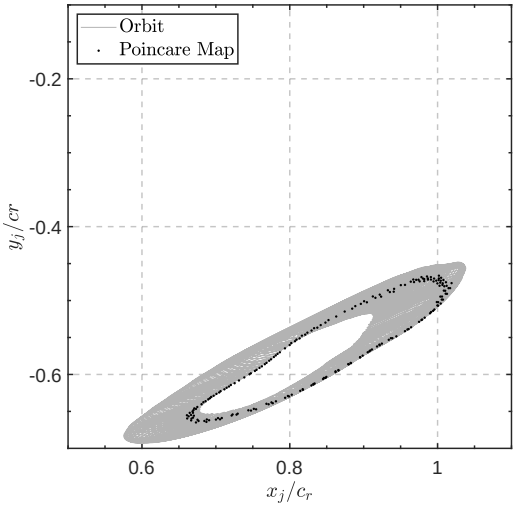

(B) Bearing #3 relative journal orbit and Poincaré Map using the forcing frequency at 6500RPM.

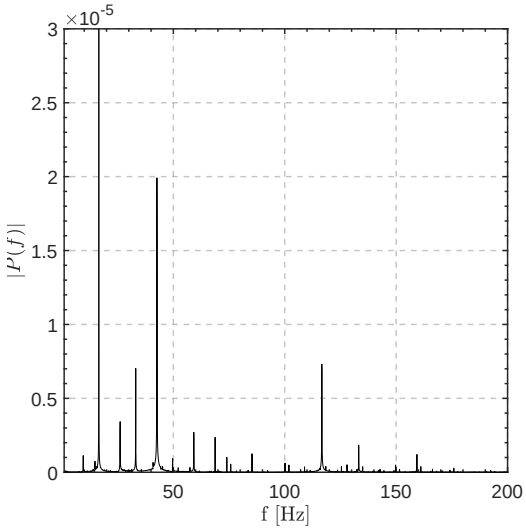

(C) Bearing #3 PSD of the chaotic attractor at 7000 RPM.

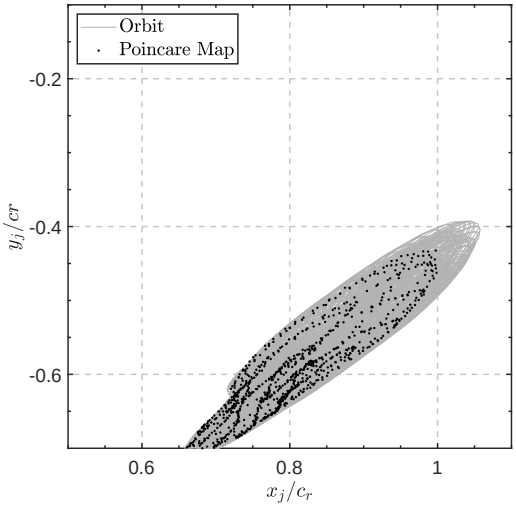

(D) Bearing #3 relative journal orbit and Poincaré Map using the forcing frequency at 7000 RPM.

FIGURE 4.4: Quasiperiodic and chaotic motion in the region between local and global instability. Unbalanced system *G*2.5 (non-autonomous system)

Another interesting observation is that between the speed where a supercritical Neimark-Sacker occurs, c.a. $\Omega = 5000$RPM (for the unbalanced, or non-autonomous systems) and the speed where the subcritical Neimark-Sacker occurs (for the balanced, or autonomous system) and global stability is lost ca. $\Omega = 7000$RPM, there exist a 2-period quasi-periodic attractor which breaks down to a chaotic attractor (torus breakdown) as shown in Fig 4.4. The region between local and global instability gets narrower as the unbalance magnitude increases.

The effectiveness of collocation method to evaluate complex (but still periodic) limit cycle motions is depicted in Fig. 4.5 at Operating speed Ω = 7000 RPM of the balanced reference system (autonomous). The response considers Bearing #5. One

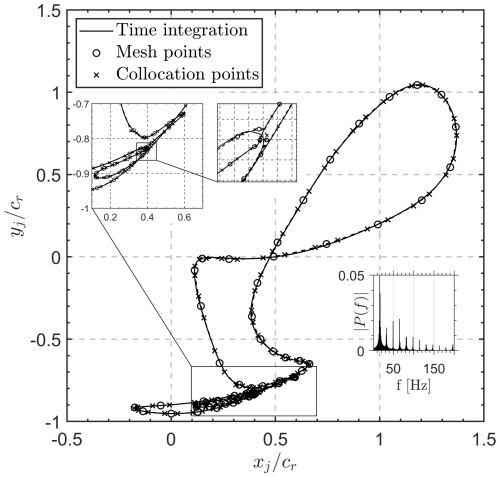

FIGURE 4.5: Indicative complex limit cycles evaluated by collocation method, and respective PSD

may notice the initial limit cycle evaluated by transient response and the respective 60 time mesh points per period, and the 2 collocation points per mesh interval. The reader may refer to Appendix D and [39] among other references for the implementation of the method.

4.2 The influence of pedestal properties in bifurcation set

The influence of pedestal properties in the bifurcation set of the system is studied in this section. The weak pedestal properties consider pedestal stiffness and damping coefficients 10 times lower than the reference, while the strong pedestal properties are 10 times higher than the reference. Only pedestals #2, #3, #4 are considered to change properties (these are large complex structures whose properties are difficult to obtain via measurements). The solution branches of the system are evaluated through numerical continuation and in Fig. 4.6a the vertical response envelop of Bearing #5 is depicted for the three different pedestal properties, when the system is considered balanced. Fixed point continuation ends as the fixed points lose stability through supercritical Hopf bifurcations at all three cases, and afterwards (as rotating speed increases) stable limit cycles are generated losing stability through Neimark-Sacker bifurcations. The weak pedestal properties in this system increase the Hopf bifurcation speed by ca. 500 RPM, while the speed at which Neimark-Sacker bifurcations occur increases significantly by ca. 2000 RPM. Weak pedestals provide also a small extent of stable limit cycles which may translate to operability of the machine even when stability threshold is passed (Hopf bifurcation). This is not the case for the reference and strong pedestal properties. The dissipated energy in the weak pedestal (larger motions are allowed) explains the respective trend on one side. The different pedestal properties allow different static displacement of the pedestals (due to gravity load) and influence the alignment of the shaft train, and therefore the bearing loading (and their properties) at some extent.

The unbalanced generator rotor and the respective bifurcations are depicted in Figs. 4.6b and 4.6c respectively. In Fig. 4.6b, for unbalance $G2.5$, the weak pedestals influence the unbalance response amplitude which is significantly reduced. At all cases Neimark-Sacker bifurcations occur at rotating speed out of the operating range,

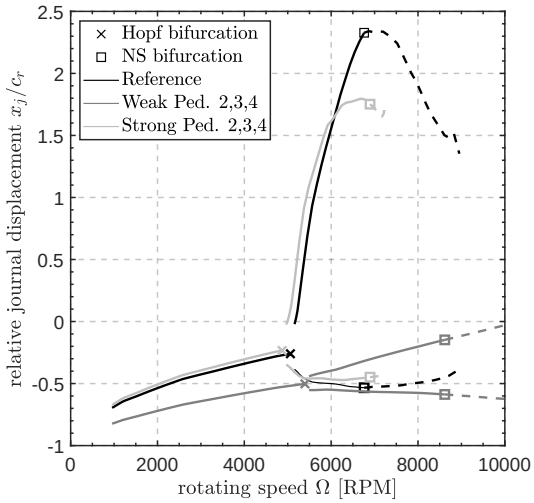

(A) Bearing #5 relative journal response in vertical direction. Balanced system *G*0 (autonomous system).

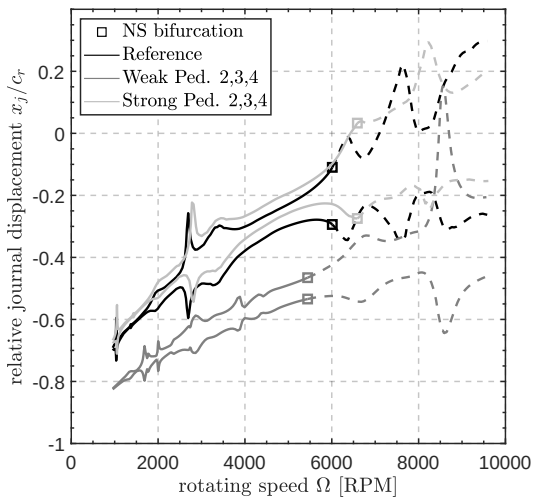

(B) Bearing #5 relative journal response in vertical direction. Unbalanced system *G*2.5 (non-autonomous system).

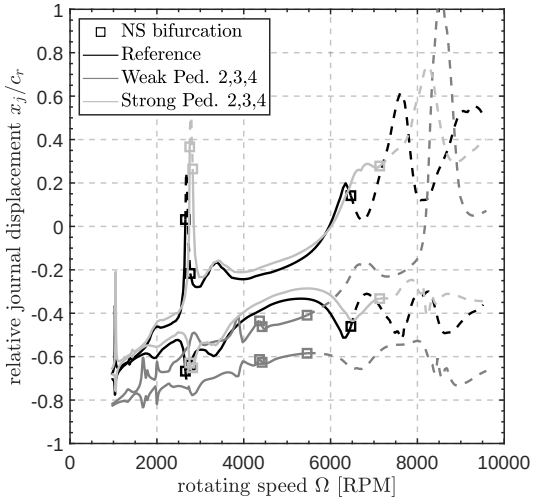

(C) Bearing #5 relative journal response in vertical direction. Unbalanced system *G*6.3 (non-autonomous system).

FIGURE 4.6: Continuation of fixed point and of limit cycles progressed at the vertical plane for three different pedestal properties of stiffness and damping.

these being shifted at lower speed by ca. 500 RPM when weak pedestals are applied, and at higher speed by ca. 500 RPM when strong pedestals are applied, compared to the reference case.

Similar trend is depicted in Fig. 4.6c where unbalance *G*6.3 is applied. The important difference compared to *G*2.5 case is that additional Neimark-Sacker bifurcations occur at speeds in the operating range of the machine, at ca. the 2^{nd} critical speed, when the reference and the strong pedestals apply. The weak pedestals introduce Neimark-Sacker bifurcations out of the operating speed range, but still close to the upper limit.

Lateral and angular misalignment is a common problem in turbine generator shaft trains. Referring to Chapter 2, lateral misalignment is considered the lateral

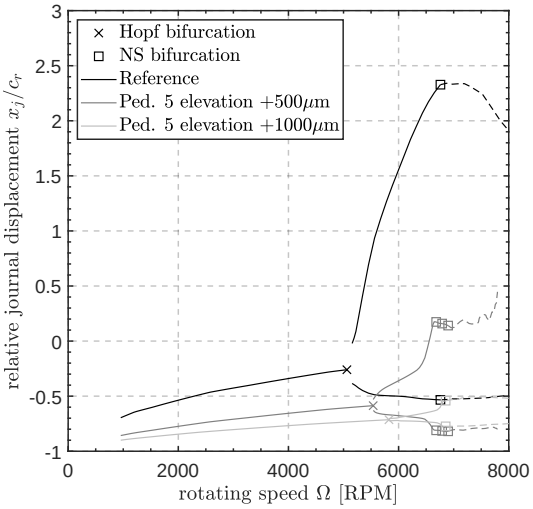

(A) Bearing #5 relative journal response in vertical direction. Balanced system *G*0 (autonomous system).

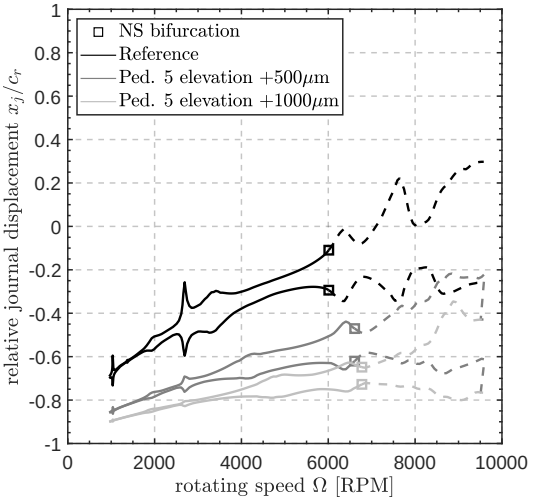

(B) Bearing #5 relative journal response in vertical direction. Unbalanced system *G*2.5 (autonomous system).

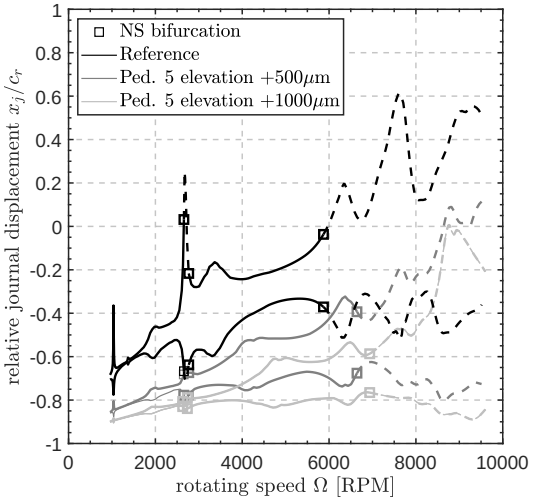

(C) Bearing #5 relative journal response in vertical direction. Unbalanced system *G*6.3 (autonomous system).

FIGURE 4.7: Continuation of fixed point and of limit cycles progressed at the vertical plane for three different elevation values of the Pedestal #5.

(vertical) displacement of any bearing center with respect to the reference center defined on site so as to produce minimal bending moment at the two couplings, and adequate load on SR shaft bearing (Bearing #5). There are two main issues that cause such displacements: non perfect technical work during alignment, and ground retreat due to non-perfect foundation. Pedestal displacements of up to $500\mu m$ are considered in the standard design (especially in double bearing design - not this case hereby), with the respective bearing loads to have major role on the bearing properties and the stability. Such case is considered in Fig. 4.7 where the bifurcation set of the autonomous system (balanced) is depicted for the case that the last bearing is elevated by $500\mu m$. In Fig. 13, it is clear that the instability threshold is shifted to higher speeds when the Bearing #5 load increases (elevation of the bearing increases).

4.3 The influence of bearing design in bifurcation set

In this section, some key design parameters of the bearings are changed and the influence in the bifurcation set is presented. The radial clearance of Bearings #2, #3 and #4 (lemon bore bearings) is increased by 20% and decreased by - 20% with respect to the radial clearance of the reference design which defines radial clearance of approximately 0.002 times the journal radius at all bearings.

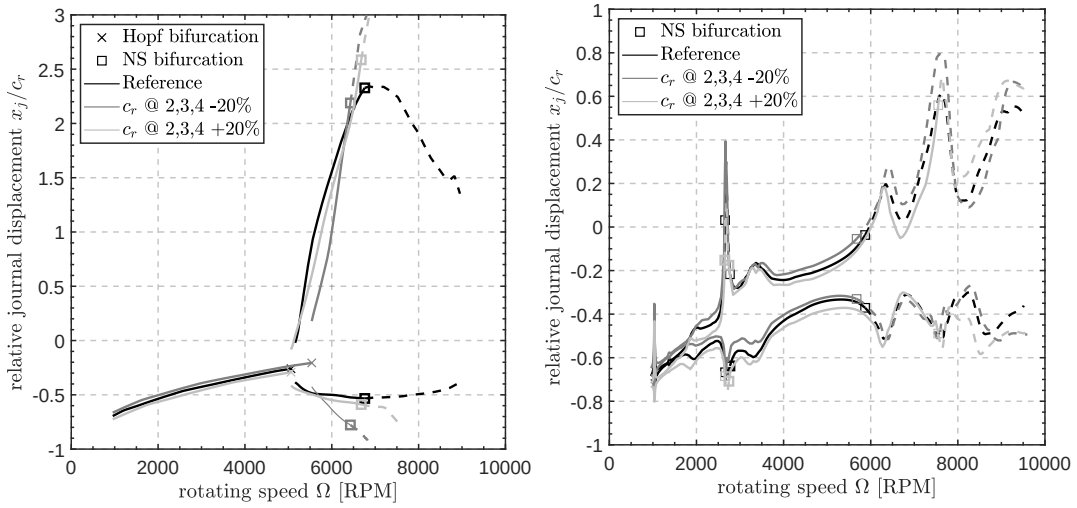

(A) Bearing #5 relative journal response in vertical direction. Balanced system *G*0 (autonomous system).

(B) Bearing #5 relative journal response in vertical direction. Unbalanced system *G*6.3 (non-autonomous system).

FIGURE 4.8: Continuation of fixed point and of limit cycles progressed at the vertical plane for three different radial clearance values of the Bearings #2, #3, #4.

In Fig. 4.8, the response envelop at Bearing #5 is depicted for the respective radial clearance variations. It is clear that the change at radial clearance renders a shift in the threshold speed of instability in the balance system (see Figure 4.8a) by ca. 500RPM higher as the bearing clearance is +20%. The decrement of clearance by -20% does not render any significant shift of the instability threshold speed. This is not always the case for rotating systems as the radial clearance has a sensitive effect to the Sommerfeld number and the respective stiffness and damping properties. Similarly, in Fig. 4.8b the threshold speed of instability of the unbalanced system is increased by ca. 1700RPM as the radial clearance is increased by +20%, while the decrement of radial clearance by -20% does not render significant change in the instability threshold defined here as the speed of the last (at higher speed) Neimark-Sacker bifurcation. It is worth mentioning that in the unbalanced system (see Figure 4.8b), the Neimark-Sacker bifurcation occurring at the 2^{nd} critical speed when the reference and the higher clearance are applied, does not exist in the -20% radial clearance. The last notification emerges the scenario that reference unbalance *G*2.5 may render Neimark-Sacker bifurcations in rotating speeds inside the operating range when certain clearance is applied in the bearings.

The offset is changed in the lemon bore Bearings #2, #3 and #4 and the respective bifurcation set is calculated for the balanced system, and depicted in Fig. **??** at Bearing #3. There is no significant shift of the threshold speed of instability (Hopf point), and the same goes for the unbalanced system. At the same bearings, the preload is changed and the respective bifurcation set is depicted at Bearing #3 response, in

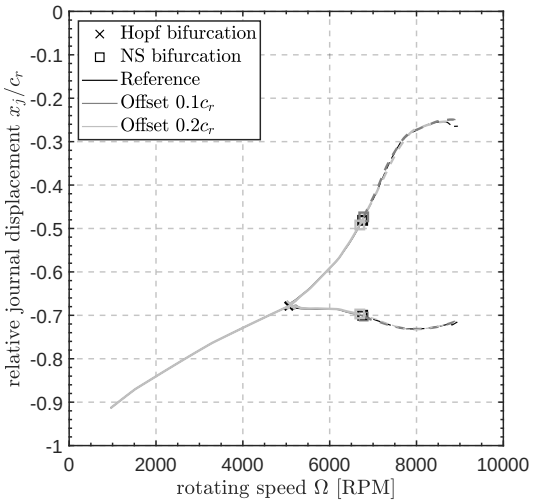

FIGURE 4.9: Bearing #4 relative journal response in vertical direction. Balanced system *G*0 (autonomous system) for three different offset values of Bearings #2, #3, #4.

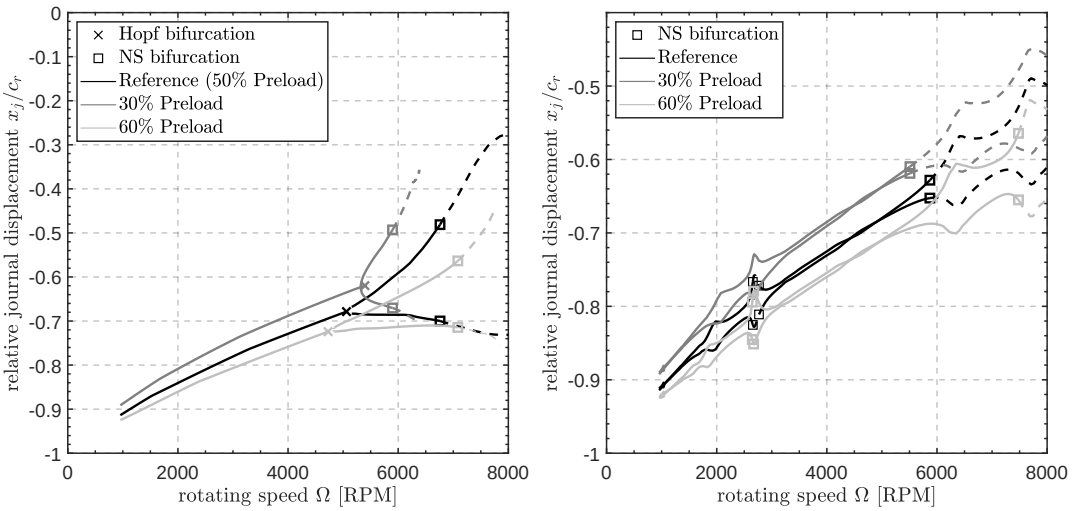

(A) Bearing #3 relative journal response in vertical direction. Balanced system *G*0 (autonomous system).

(B) Bearing #3 relative journal response in vertical direction. Unbalanced system *G*6.3 (non-autonomous system).

FIGURE 4.10: Continuation of fixed point and of limit cycles progressed at the vertical plane for three different preload values of the Bearings #2, #3, #4.

Fig. 4.10 for the balanced and unbalanced system. Minor alterations are presented at both cases (balanced and unbalanced), increasing the Hopf bifurcation speed and the Neimark-Sacker bifurcation speed in the respective two systems. In Fig. 4.10 one may notice that the bifurcation set for 30% bearing preload does not include a Neimark-Sacker bifurcation at the 2^{nd} critical speed of the GEN rotor (rotating speed ca. 2650 RPM), while the case for 60% bearing preload does. However, the 60% bearing preload will render an increment of the rotating speed where the 3^{rd} Neimark-Sacker bifurcations takes place (rotating speed ca. 7500 RPM). The arc length of the lemon bore Bearings #2, #3 and #4 is changed and the bifurcation set is calculated and presented in Fig.4.11. One may notice that fore the arc angle $\alpha = 140^{\circ}$, there is

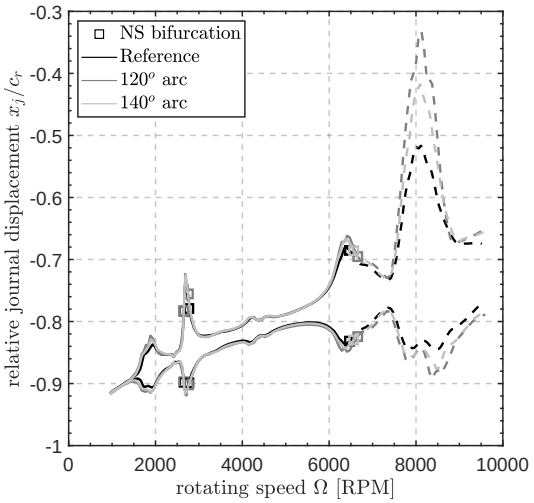

FIGURE 4.11: Continuation of fixed point and of limit cycles progressed at the vertical plane for three different arclength values of the Bearings #2, #3, #4. Unbalanced system *G*6.3 (non-autonomous system).

no Neimark-Sacker bifurcation occurring at the operating speed range (<3600 RPM). This is not the case for $\alpha = 120^\circ$ and for the reference design $\alpha = 160^\circ$.

4.4 The effect of rotor properties in bifurcation set

Alternative GEN rotor designs are studied in this section on their potential to present bifurcations at the operating speed range, which is of major importance. The design parameter selected to be studied is the rotor slenderness ratio which directly related to the rotor's flexibility. The slenderness ratio L of the GEN rotor is defined as the ratio of the bearing span L between Bearing #3 and #4 (where $L = L_3$ in Fig. 2.5a) to an equivalent diameter D_{eq} (not depicted in Fig. 2.5a) which is evaluated directly by the area A_S defined by the stiffness diameters of the GEN rotor segments between Bearing #3 and #4, as $\lambda = L/D_{eq}$. The equivalent diameter is then $D_{eq} = A_s/L$. It is clear that for a uniform rotor of diameter D, $D_{eq} = D$ as $A_S = LD$. The value $\lambda = 13$ is realistic for large GEN rotors. However, turbine rotors hardly exceed $\lambda = 10$. Several GEN rotor designs are available but slenderness ratio is hardly higher than $\lambda = 14$. A flexible GEN rotor of $\lambda = 15$ is included in this case study as a theoretical example, to show that rotor systems of high slenderness may become unstable at relatively low speed of operation [9]. The GEN rotor of $\lambda = 11$ will lose stability for much higher speed than the realistic design of $\lambda = 13$ which depicts a threshold speed of instability at ca. 4400RPM (this being 122% overspeed), see Fig. 4.12. *G*2.5 unbalance is applied in GEN rotors per ISO. It is worth noticing that a design of $\lambda = 11$ will not depict Neimark-Sacker bifurcation in the operating speed range, while designs of $\lambda = 12$ and $\lambda = 13$ will do.

As the existence of Neimark-Sacker bifurcations in the operating speed range is sensitive too the unbalance magnitude, slender rotors should be considered well-balanced on site so as to avoid bifurcations triggered near critical speeds (as appeared in the results of previous sections too).

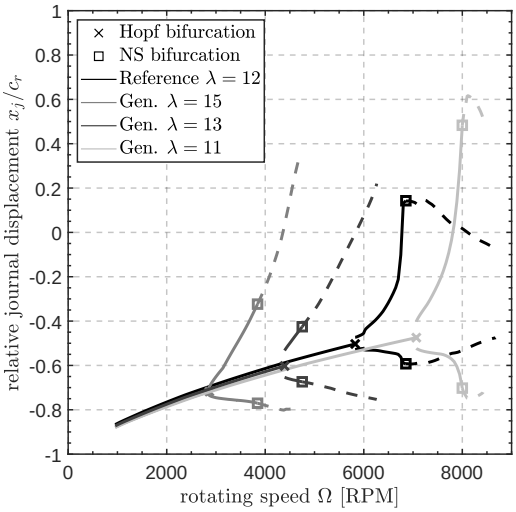

(A) Balanced system *G*0 (autonomous system).

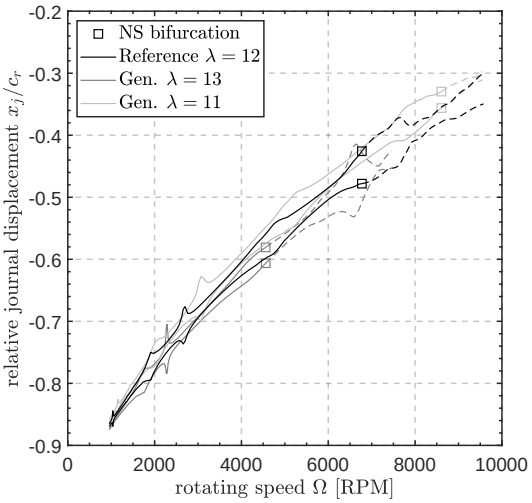

(B) Unbalanced system *G*2.5 (non-autonomous system).

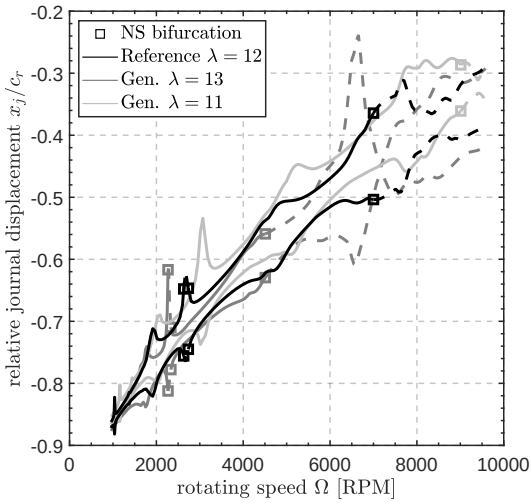

(C) Unbalanced system *G*6.3 (non-autonomous system).

FIGURE 4.12: Continuation of fixed point and of limit cycles progressed at the vertical plane, at Bearing #4 for different values of GEN rotor slenderness.

Chapter 5

Conclusions and recommendations for future work

The present work applies the pseudo arclength continuation method combined with an orthogonal collocation method to evaluate stable and unstable motions (limit cycles) of a realistic multi-rotor multi-bearing turbine-generator shaft train, which is modeled considering nonlinearities of the sliding bearing impedance forces. The standard dynamic design (for the execution engineering) of such systems is still nowadays performed assuming harmonic rotor motions (linear harmonic analysis). Based on the following conclusions, this thesis aims to raise further concerns on the dynamic design of such systems, widely applied in power generation.

The unbalanced shaft train may become locally unstable through Neimark-Sacker bifurcations in speeds lower than the threshold speed of instability Ω_{th}, with Ω_{th} to coincide here to the speed where Hopf bifurcation occurs (for the balanced system). Ω_{th} is very similar to this predicted by linear harmonic analysis (where linearized bearing coefficients are used). The aforementioned Neimark-Sacker bifurcations (and the respective locally unstable motion) may even appear at speeds lower than the service speed, when higher unbalance magnitude applies, and the system passes through a major resonance (critical speed).

Depending on bearing design and pedestal properties, when operating speed exceeds the threshold speed of instability, the system produces limit cycles of higher or lower (depending on the case) extent inside each bearing clearance, prohibiting or allowing operation. This is important to predict as the shaft-train may operate close to threshold speed of instability, especially when slender generator rotors are included in the design.

Bearing offset and partial arc angle where not correlated to significant changes of the bifurcation set, while bearing preload change rendered sensitive changes. Pedestal properties of stiffness and damping are also parameters which alter the bifurcation set of the nonlinear dynamic system.

The evaluation time for the computation of unbalance response applying numerical continuation and embedded collocation method is approximately an order of magnitude faster than time integration for the evaluation of stable limit cycles and an order of magnitude slower from the time required for a linear harmonic analysis of the linearized system. This is feasible after applying model order reduction methods in the rotor models.

Appendix A

Beam Element Matrices

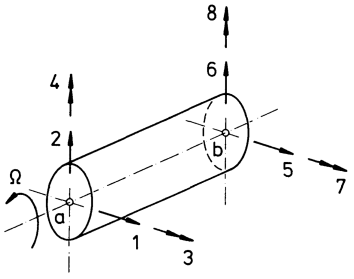

FIGURE A.1: Rotating beam element bending in two dimensions [8]

The stiffness matrix of the beam element is

$$\mathbf{K} = \begin{bmatrix} a_1 & & & -a_2 & -a_1 & & & -a_2 \\ & a_1 & a_2 & & & -a_1 & a_2 & \\ & & a_3 & & & -a_2 & a_4 & \\ & & & a_3 & a_2 & & & a_4 \\ & & & & a_1 & & & a_2 \\ & & & \text{sym.} & & a_1 & -a_2 & \\ & & & & & & a_3 & \\ & & & & & & & a_3 \end{bmatrix} \tag{A.1}$$

where

$$a_1 = \frac{12}{1+e}\frac{EI}{l^3},\ a_2 = \frac{6}{1+e}\frac{EI}{l^2},\ a_3 = \frac{4+e}{1+e}\frac{EI}{l},\ a_4 = \frac{2-e}{1+e}\frac{EI}{l},\ e = \frac{12EI}{G\kappa Al^2} \tag{A.2}$$

and E is the Young's Modulus of the element material, G is the Shear Modulus of the element material, l is the element length, I is the 2nd moment of area of the element cross section and κ is the shear factor which depends on the form of the cross section. $\kappa = 0.89$ for a circle and 0.53 for a thin circular ring.

The mass matrix of the beam element is

$$\mathbf{M} = \begin{bmatrix} c_1 & & & -c_3 & -c_2 & & & c_4 \\ & c_1 & c_3 & & & c_2 & -c_4 & \\ & & c_5 & & & c_4 & -c_6 & \\ & & & c_5 & -c_4 & & & -c_6 \\ & & & & c_1 & & & c_3 \\ & & & \text{sym.} & & c_1 & -c_3 & \\ & & & & & & c_5 & \\ & & & & & & & c_5 \end{bmatrix} \tag{A.3}$$

where

$$
\begin{aligned}
c_1 &= \frac{1}{(1+e)^2}\left(\frac{156}{420}\mu l + \frac{36}{30}\frac{\mu_d}{l} + \frac{84}{120}e\mu l + \frac{40}{120}e^2\mu l\right)\\
c_2 &= \frac{1}{(1+e)^2}\left(\frac{54}{420}\mu l - \frac{36}{30}\frac{\mu_d}{l} + \frac{36}{120}e\mu l + \frac{20}{120}e^2\mu l\right)\\
c_3 &= \frac{l}{(1+e)^2}\left(\frac{22}{420}\mu l + \frac{3}{30}\frac{\mu_d}{l} + \frac{11}{120}e\mu l + \frac{5}{120}e^2\mu l - \frac{3}{6}\frac{e\mu_d}{l}\right)\\
c_4 &= \frac{l}{(1+e)^2}\left(\frac{13}{420}\mu l - \frac{3}{30}\frac{\mu_d}{l} + \frac{9}{120}e\mu l + \frac{5}{120}e^2\mu l + \frac{3}{6}\frac{e\mu_d}{l}\right)\\
c_5 &= \frac{l^2}{(1+e)^2}\left(\frac{4}{420}\mu l + \frac{4}{30}\frac{\mu_d}{l} + \frac{2}{120}e\mu l + \frac{1}{120}e^2\mu l + \frac{1}{6}\frac{e\mu_d}{l} + \frac{2}{6}\frac{e^2\mu_d}{l}\right)\\
c_6 &= \frac{l^2}{(1+e)^2}\left(\frac{3}{420}\mu l + \frac{1}{30}\frac{\mu_d}{l} + \frac{2}{120}e\mu l + \frac{1}{120}e^2\mu l + \frac{1}{6}\frac{e\mu_d}{l} - \frac{1}{6}\frac{e^2\mu_d}{l}\right)
\end{aligned}
\tag{A.4}
$$

and e as stated previously and μ_d is the mass per unit length

$$\mu = \frac{m}{l} = \rho A \tag{A.5}$$

and

$$\mu_d = \rho I. \tag{A.6}$$

The gyroscopic matrix of the beam element is

$$
\mathbf{G} = \begin{bmatrix}
0 & g_1 & g_2 & & & -g_1 & g_2 & \\
 & 0 & & g_2 & g_1 & & & g_2 \\
 & & 0 & g_4 & g_2 & & & g_3 \\
 & & & 0 & & g_2 & g_3 & \\
 & & & & 0 & g_1 & -g_2 & \\
 & & \text{skew-sym.} & & & 0 & & -g_2 \\
 & & & & & & 0 & g_4 \\
 & & & & & & & 0
\end{bmatrix}
\tag{A.7}
$$

where

$$
\begin{aligned}
g_1 &= \frac{6}{5}\frac{1}{l}\mu_p\Omega \qquad g_2 = \frac{1}{10}\mu_p\Omega\\
g_1 &= \frac{6}{5}\frac{1}{l}\mu_p\Omega \qquad g_2 = \frac{1}{10}\mu_p\Omega
\end{aligned}
\tag{A.8}
$$

and

$$\mu_p = 2\mu_d = 2\rho I \tag{A.9}$$

Appendix B

Guyan Reduction

The static equilibrium equation is expressed as:

$$\mathbf{K}\boldsymbol{x} = \boldsymbol{f} \tag{B.1}$$

where $\mathbf{K}$ is the stiffness matrix, $\boldsymbol{f}$ is the force vector and $\boldsymbol{d}$ the displacement vector. By partitioning the above system of linear equations with regards to loaded (master) and unloaded (slave) degrees of freedom, the static equilibrium equation can be written as:

$$\begin{bmatrix} \mathbf{K}_{mm} & \mathbf{K}_{ms} \\ \mathbf{K}_{sm} & \mathbf{K}_{ss} \end{bmatrix} \begin{Bmatrix} \boldsymbol{x}_m \\ \boldsymbol{x}_s \end{Bmatrix} = \begin{Bmatrix} \boldsymbol{f}_m \\ \mathbf{0} \end{Bmatrix} \tag{B.2}$$

where $\mathbf{0}$ represents the zero vector of length equal to the number of slave DoFs. Solving the lower partition of the above system of equations yields:

$$\mathbf{K}_{sm}\boldsymbol{x}_m + \mathbf{K}_{ss}\boldsymbol{x}_s = 0 \tag{B.3}$$

Solving the above equation in terms of the master DoFs leads to:

$$\boldsymbol{x}_s = -\mathbf{K}_{ss}^{-1}\mathbf{K}_{sm}\boldsymbol{x}_m \tag{B.4}$$

Finally substituting to the upper partition of equation B.2 leads to the following reduced system of linear equations.

$$(\mathbf{K}_{mm} - \mathbf{K}_{ms}\mathbf{K}_{ss}^{-1}\mathbf{K}_{sm})\boldsymbol{x}_m = \boldsymbol{f}_m \tag{B.5}$$

The above system of linear equations is equivalent to the original problem but expressed in terms of the master degrees of freedom. Thus, the Guyan reduction results in a reduced system by condensing away the slave degrees of freedom.

The Guyan reduction can also be expressed as a change of basis which produces a low-dimensional representation of the original space, represented by the master degrees of freedom. The linear transformation that maps the reduced space onto the full space is expressed as:

$$\begin{Bmatrix} \boldsymbol{x}_m \\ \boldsymbol{x}_s \end{Bmatrix} = \begin{bmatrix} \mathbf{I} \\ -\mathbf{K}_{ss}^{-1}\mathbf{K}_{sm} \end{bmatrix} \{\boldsymbol{x}_m\} = \{\boldsymbol{T}_G\} \{\boldsymbol{x}_m\} \tag{B.6}$$

where $\boldsymbol{T}_r$ represents the Guyan reduction transformation matrix. Thus, the reduced problem is represented as:

$$\mathbf{K}_r\boldsymbol{x}_m = \boldsymbol{f}_m \tag{B.7}$$

where $\mathbf{K}_r$ represents the reduced system of linear equations that's obtained by applying the Guyan reduction transformation on the full system, which is expressed as:

$$\mathbf{K}_r = \boldsymbol{T}_r^T \mathbf{K} \boldsymbol{T}_r \tag{B.8}$$

The same transformation can be applied to the mass, damping and gyroscopic matrices. However, stiffness coefficients will appear in those matrices. The result is that the eigenvalue-eigenvector problem is closely but not exactly preserved.

Appendix C

Application of Finite Difference method in the solution of Reynolds equation

Consider a numerical solution for the Reynolds equation as defined below for laminar parallel, isothermal, isoviscous and incompressible flow with negligible inertial forces.

$$\frac{1}{\mu R^2}\frac{\partial}{\partial\theta}\left(h^3\frac{\partial p}{\partial\theta}\right)+\frac{h^3}{\mu}\frac{\partial^2 p}{\partial z^2}=6\Omega\frac{\partial h}{\partial\theta}+12\frac{\mathrm{d}h}{\mathrm{d}t} \tag{C.1}$$

Given the fluid thickness $h = h(\theta)$ and a grid of points $N_\theta \times N_z$, discretized by $d\theta$ and dz respectively, then the linearized system of equations are:

$$Ap = Q \tag{C.2}$$

where

$$A=\begin{bmatrix} D_1 & U_1 & & & & \\ L_1 & D_2 & U_2 & & & \\ & L_2 & D_3 & \ddots & & \\ & & \ddots & \ddots & & \\ & & & L_{N_z-2} & D_{N_z-1} & U_{N_z-2} \end{bmatrix} \tag{C.3}$$

$$D_1 = D_2 = \cdots = D_{N_z-1} = \begin{bmatrix} d_1 & d_1^u & & & & \\ d_1^l & d_2 & d_2^u & & & \\ & d_2^l & d_3 & \ddots & & \\ & & \ddots & \ddots & & \\ & & & d^l_{N_\theta-2} & d_{N_\theta-1} & d^l_{N_\theta-2} \end{bmatrix} \tag{C.4}$$

$$\begin{aligned} d_j &= -\frac{2h_j^3}{dz^2\mu}-\frac{2h_j^3}{d\theta\mu R^2} \\ d_j^u &= \frac{h_j^3}{d\theta^2R^2\mu}+\frac{3h_j^2}{2d\theta R^2\mu}\frac{\mathrm{d}h}{\mathrm{d}t}\Big|_{\theta=\theta_j} \\ d_j^l &= \frac{h_{j+1}^3}{d\theta^2\mu R^2}-\frac{3h_{j+1}^2}{2d\theta R^2\mu}\frac{\mathrm{d}h}{\mathrm{d}t}\Big|_{\theta=\theta_{j+1}} \end{aligned}$$

,

$$U_1 = L_1 = U_2 = L_2 = \cdots = U_{N_z-2} = L_{N_z-2} = \frac{1}{dz^2\mu} \begin{bmatrix} h_1^3 & & & \\ & h_2^3 & & \\ & & \ddots & \\ & & & h_{N_\theta-1}^3 \end{bmatrix} \tag{C.5}$$

and

$$Q = \begin{Bmatrix} R_1 \\ R_2 \\ \vdots \\ R_{N_z-1} \end{Bmatrix} \tag{C.6}$$

where

$$R_1 = R_2 = \cdots = R_{N_z-1} = 6\Omega \begin{Bmatrix} \left.\frac{\partial h}{\partial \theta}\right|_{\theta=\theta_1} \\ \left.\frac{\partial h}{\partial \theta}\right|_{\theta=\theta_2} \\ \vdots \\ \left.\frac{\partial h}{\partial \theta}\right|_{\theta=\theta_{N_\theta-1}} \end{Bmatrix} + 12 \begin{Bmatrix} \left.\frac{\partial h}{\partial t}\right|_{\theta=\theta_1} \\ \left.\frac{\partial h}{\partial t}\right|_{\theta=\theta_2} \\ \vdots \\ \left.\frac{\partial h}{\partial t}\right|_{\theta=\theta_{N_\theta-1}} \end{Bmatrix} \tag{C.7}$$

Then the discretized pressure distrubution is computed by solving the linear system:

$$p = A^{-1}Q \tag{C.8}$$

Appendix D

Pseudo-arclength continuation with orthogonal collocation

The problem is to find periodic solutions $\boldsymbol{x}(\boldsymbol{\xi_0}, t, \Omega)$ for the following Boundary Value Problem:

$$\dot{\boldsymbol{x}} = \boldsymbol{f}(\boldsymbol{x}, \Omega), \quad \boldsymbol{x}(\boldsymbol{\xi_0}, 0, \Omega) = \boldsymbol{x}(\boldsymbol{\xi_0}, T, \Omega) \tag{D.1}$$

Rotating speed Ω is the continuation parameter (bifurcation parameter), $\boldsymbol{\xi_0}$ is an initial state vector that belongs to the solution curve $\boldsymbol{x}$ and T is the period of the solution. Since the period T can be unknown, time t is rescaled to $[0, 1]$ and Equation D.1 becomes

$$\dot{\boldsymbol{x}} = T\boldsymbol{f}(\boldsymbol{x}, \Omega), \quad \boldsymbol{x}(\boldsymbol{\xi_0}, 0, \Omega) = \boldsymbol{x}(\boldsymbol{\xi_0}, 1, \Omega) \tag{D.2}$$

The period T is unkwon and an additional equation (phase condition) is required

$$\phi = \int_0^1 \langle \boldsymbol{x}, \dot{\boldsymbol{x}_0} \rangle dt = 0 \tag{D.3}$$

where $\langle \boldsymbol{x}, \boldsymbol{x}_0 \rangle$ denotes the scalar product and $\dot{\boldsymbol{x}_0}$ is the time derivative of the previous solution. If the arc length is used as a continuation parameter then Ω also becomes an unknown and an additional equation is required (pseudo arc length condition),

$$\psi = \int_0^1 \langle \boldsymbol{x} - \boldsymbol{x}_0, \boldsymbol{x}_0' \rangle dt + (T - T_0)T_0' + (\Omega - \Omega_0)\Omega_0' - \Delta s = 0 \tag{D.4}$$

where $()'$ denotes the derivative with respect to arc length $\mathrm{d}\cdot/\mathrm{d}s$. Setting $\boldsymbol{u} = (\boldsymbol{x}, T, \Omega)$ and writing D.2 as $\boldsymbol{F}(\boldsymbol{u}) = \{\boldsymbol{0}\}$, the system to solve becomes

$$\boldsymbol{H}(\boldsymbol{u}) = \begin{Bmatrix} \boldsymbol{F}(\boldsymbol{u}) \\ \phi(\boldsymbol{x}) \\ \psi(\boldsymbol{u}) \end{Bmatrix} = \begin{Bmatrix} 0 \\ 0 \\ 0 \end{Bmatrix} \tag{D.5}$$

and Newton's method for solving D.5 is

$$\boldsymbol{u}^{i+1} = \boldsymbol{u}^i - [\boldsymbol{A}(\boldsymbol{u}^i)]^{-1}\boldsymbol{H}(\boldsymbol{u}^i) \tag{D.6}$$

where

$$\boldsymbol{A}(\boldsymbol{u}) = \begin{bmatrix} \dfrac{\partial \boldsymbol{F}}{\partial \boldsymbol{x}} & \dfrac{\partial \boldsymbol{F}}{\partial T} & \dfrac{\partial \boldsymbol{F}}{\partial \Omega} \\ \dfrac{\partial \phi}{\partial \boldsymbol{x}} & 0 & 0 \\ \boldsymbol{x}_0' & T_0' & \Omega_0' \end{bmatrix} \tag{D.7}$$

The system is iterated until a suitable convergence criterion is satisfied. Quasi-Newton methods like Broyden's "good" and "bad" methods may be used. The arc length derivatives $\mathrm{d}\boldsymbol{u}/\mathrm{d}s$ for subsequent continuation steps can be calculated either by backwards differences or by solving

$$\boldsymbol{A}\frac{\mathrm{d}\boldsymbol{u}}{\mathrm{d}s} = \begin{Bmatrix} 0 & \cdots & 0 & 1 \end{Bmatrix}^T \tag{D.8}$$

The final step is to discretize in time and calculate $\boldsymbol{A}$. To this end the method of orthogonal collocation at Gauss points with piece-wise polynomials is used. An overview of the method applied to nonlinear BVPs with periodicity boundary conditions with unknwon period is given below.

The time interval $[0, 1]$ is discretized into N sub-intervals. For the i^{th} sub interval the collocation equations must be assembled at the required time nodes

$$t_{ij} = t_i + h_i\rho_j, \quad i = 1, 2, \ldots, N, \quad j = 1, 2, \ldots, m \tag{D.9}$$

where $h_i = t_i + 1 - t_i$ the length of the time sub-interval i and ρ_j are chosen as the zeroes of an m^{th} order Legendre polynomial. At the above time nodes, an initial solution $\boldsymbol{x_{ij}}$ must be provided along with the function evaluation $T\boldsymbol{f}(\boldsymbol{x_{ij}})$ abbreviated henceforth as $\boldsymbol{f_{ij}}$, Jacobian $\dfrac{\partial \boldsymbol{f}}{\partial \boldsymbol{x}}(\boldsymbol{x_{ij}}, \Omega)$, and parameter derivative (for the case of pseudo arclength continuation) $\dfrac{\partial \boldsymbol{f}}{\partial \Omega}(\boldsymbol{x_{ij}}, \Omega)$. Equivalently, the values $\boldsymbol{x_{ij}}$ can be extracted from the solutions at the global time nodes t_i as

$$\boldsymbol{x}_{ij} = \boldsymbol{x_i} + h_i \sum_{l=1}^{m} \alpha_{jl}\boldsymbol{f}_{il}, \quad \boldsymbol{x}_{i+1} = \boldsymbol{x}_i + h_i \sum_{l=1}^{m} \beta_i \boldsymbol{f}_{il} \tag{D.10}$$

where $\alpha_{j1}, \alpha_{j2}, \ldots, \alpha_{jk}$ are the quadrature weights. Then the quasi linearized two point BVP (equivlanent to Newton's method) can be written as shown below

$$\begin{aligned} \Delta\dot{\boldsymbol{x}}_{ij} = T\frac{\partial \boldsymbol{f}}{\partial \boldsymbol{x}}\left(\boldsymbol{x}_{ij}, \Omega\right)\Delta\boldsymbol{x}_{ij} + \boldsymbol{f}\left(\boldsymbol{x}_{ij}, \Omega\right)\Delta T + T\frac{\partial \boldsymbol{f}}{\partial \Omega}\left(\boldsymbol{x}_{ij}, \Omega\right)\Delta\Omega + \boldsymbol{r_{ij}} \\ \boldsymbol{x}_{N+1} - \boldsymbol{x}_1 = \boldsymbol{0} \end{aligned} \tag{D.11}$$

where $\boldsymbol{r}_{ij} = T\boldsymbol{f}(\boldsymbol{x}_{ij}, \Omega) - \dot{\boldsymbol{x}}_{ij}$. Applying parameter condensation to eliminate the local unknowns $\boldsymbol{x}_{ij}$ at every time interval t_i we can write the derivatives

$$\boldsymbol{f}_i = \begin{bmatrix} \boldsymbol{f}_{i1} & \boldsymbol{f}_{i2} & \cdots & \boldsymbol{f}_{im} \end{bmatrix}^T$$

for the local unknowns as a function of the global unknowns $\boldsymbol{x}_i$. Substituting (D.10a) in (D.11) yields

$$\begin{aligned} \boldsymbol{f}_i(\Delta\boldsymbol{x}_{ij}) = \boldsymbol{f}\left(\Delta\boldsymbol{x_i} + h_i\sum_{l=1}^{m}\alpha_{jl}\boldsymbol{f}_{il}\right) = \\ T\frac{\partial \boldsymbol{f}}{\partial \boldsymbol{x}}\left(\boldsymbol{x}_{ij}, \Omega\right)\Delta\boldsymbol{x}_{ij} + T\frac{\partial \boldsymbol{f}}{\partial \boldsymbol{x}}\left(\boldsymbol{x}_{ij}, \Omega\right)\Delta\boldsymbol{x}_{ij}h_i\sum_{l=1}^{m}\alpha_{jl}\boldsymbol{f}_{il} \\ + \boldsymbol{f}\left(\boldsymbol{x}_{ij}, \Omega\right)\Delta T + T\frac{\partial \boldsymbol{f}}{\partial \Omega}\left(\boldsymbol{x}_{ij}, \Omega\right)\Delta\Omega + \boldsymbol{r_{ij}} \end{aligned} \tag{D.12}$$

The above can be rewritten as

$$\boldsymbol{f}_i = \mathbf{W}_i^{-1}\mathbf{V}_i\Delta\boldsymbol{x}_i + \mathbf{W}_i^{-1}\mathbf{U}_i\Delta T + \mathbf{W}_i^{-1}\mathbf{S}_i\Delta\Omega + \mathbf{W}_i^{-1}\boldsymbol{q}_i \tag{D.13}$$

where

$$\mathbf{W}_i = \mathbf{I} - h_i \begin{bmatrix} \alpha_{11} T\dfrac{\partial \boldsymbol{f}}{\partial \boldsymbol{x}}(\boldsymbol{x}_{i1},\Omega) & \cdots & \alpha_{1m} T\dfrac{\partial \boldsymbol{f}}{\partial \boldsymbol{x}}(\boldsymbol{x}_{i1},\Omega) \\ \vdots & \ddots & \vdots \\ \alpha_{1m} T\dfrac{\partial \boldsymbol{f}}{\partial \boldsymbol{x}}(\boldsymbol{x}_{im},\Omega) & \cdots & \alpha_{mm} T\dfrac{\partial \boldsymbol{f}}{\partial \boldsymbol{x}}(\boldsymbol{x}_{im},\Omega) \end{bmatrix}$$

$$\mathbf{V}_i = \begin{Bmatrix} T\dfrac{\partial \boldsymbol{f}}{\partial \boldsymbol{x}}(\boldsymbol{x}_{i1},\Omega) \\ \vdots \\ T\dfrac{\partial \boldsymbol{f}}{\partial \boldsymbol{x}}(\boldsymbol{x}_{im},\Omega) \end{Bmatrix}, \mathbf{U}_i = \begin{Bmatrix} \boldsymbol{f}(\boldsymbol{x}_{i1},\Omega) \\ \vdots \\ \boldsymbol{f}(\boldsymbol{x}_{im},\Omega) \end{Bmatrix}, \mathbf{S}_i = \begin{Bmatrix} T\dfrac{\partial \boldsymbol{f}}{\partial \Omega}(\boldsymbol{x}_{i1},\Omega) \\ \vdots \\ T\dfrac{\partial \boldsymbol{f}}{\partial \Omega}(\boldsymbol{x}_{im},\Omega) \end{Bmatrix},$$

$$\boldsymbol{q}_i = \begin{Bmatrix} T\boldsymbol{f}(\boldsymbol{x}_{i1},\Omega) - \boldsymbol{f}_{i1} \\ \vdots \\ T\boldsymbol{f}(\boldsymbol{x}_{im},\Omega) - \boldsymbol{f}_{im} \end{Bmatrix}$$

Substituting (D.13) to (D.10b) yields a set of $n \times N$ linear equations

$$\begin{aligned} &\Delta\boldsymbol{x}_{i+1} = \Delta\boldsymbol{x}_i + h_i \sum_{l=1}^{m} \beta_i \boldsymbol{f}_{il} \\ =&\Delta\boldsymbol{x}_i + h_i \left[\beta_1\mathbf{I}\cdots\beta_m\mathbf{I}\right]\left[\mathbf{W}_i^{-1}\mathbf{V}_i\Delta\boldsymbol{x}_i + \mathbf{W}_i^{-1}\mathbf{U}_i\Delta T + \mathbf{W}_i^{-1}\mathbf{S}_i\Delta\Omega + \mathbf{W}_i^{-1}\boldsymbol{q}_i\right] \\ =&\boldsymbol{\Gamma}_i\Delta\boldsymbol{x}_i + \boldsymbol{\Lambda}_i\Delta T + \boldsymbol{\Sigma}_i\Delta\Omega_i + \boldsymbol{r}_i \end{aligned} \tag{D.14}$$

where $\mathbf{D} = \left[\beta_1\mathbf{I}\cdots\beta_m\mathbf{I}\right], \boldsymbol{\Gamma}_i = \mathbf{I} + h_i\mathbf{D}\mathbf{W}_i^{-1}\mathbf{V}_i, \boldsymbol{\Lambda}_i = h_i\mathbf{D}\mathbf{W}_i^{-1}\mathbf{U}_i, \boldsymbol{\Sigma}_i = h_i\mathbf{D}\mathbf{W}_i^{-1}\mathbf{S}_i, \boldsymbol{r}_i = h_i\mathbf{D}\mathbf{W}_i^{-1}\boldsymbol{q}_i$

The linear algebraic system for the combined collocation-pseudo arc length continuation method is finally expressed in Eq. (D.15).

$$
\begin{bmatrix}
-\mathbf{\Gamma}_1 & \mathbf{I} & \mathbf{0} & \cdots & \mathbf{0} & -\mathbf{\Lambda}_1 & -\mathbf{\Sigma}_1 \\
\mathbf{0} & -\mathbf{\Gamma}_2 & \mathbf{I} & \mathbf{0} & \cdots & -\mathbf{\Lambda}_2 & -\mathbf{\Sigma}_2 \\
 & & \ddots & \ddots & & \vdots & \vdots \\
\mathbf{0} & \mathbf{0} & \cdots & -\mathbf{\Gamma}_N & \mathbf{I} & -\mathbf{\Lambda}_N & -\mathbf{\Sigma}_N \\
\mathbf{I} & \mathbf{0} & \cdots & \mathbf{0} & -\mathbf{I} & \mathbf{0} & \mathbf{0} \\
h_1\boldsymbol{x}_1 & h_1\boldsymbol{x}_2 & \cdots & h_N\boldsymbol{x}_N & \mathbf{0} & \mathbf{0} & \mathbf{0} \\
h_1\boldsymbol{x}_1'^0 & h_1\boldsymbol{x}_2'^0 & \cdots & h_1\boldsymbol{x}_N'^0 & \mathbf{0} & T'^0 & \Omega'^0
\end{bmatrix}
\begin{bmatrix} \Delta\boldsymbol{x}_1 \\ \Delta\boldsymbol{x}_2 \\ \vdots \\ \Delta\boldsymbol{x}_N \\ \Delta\boldsymbol{x}_{N+1} \\ \Delta T \\ \Delta\Omega \end{bmatrix} =
$$

$$
\begin{bmatrix}
\boldsymbol{r}_1 \\
\boldsymbol{r}_2 \\
\vdots \\
\boldsymbol{r}_N \\
\boldsymbol{x}_{N+1} - \boldsymbol{x}_1 \\
\sum_{i=1}^{N} h_i \langle \boldsymbol{x}_i, \dot{\boldsymbol{x}}_i^0 \rangle \\
\sum_{i=1}^{N} h_i \langle \boldsymbol{x}_i - \boldsymbol{x}_i^0, \boldsymbol{x}'^0 \rangle + (T - T^0)T'^0 + (\Omega - \Omega^0)\Omega'^0 - \Delta s
\end{bmatrix} \tag{D.15}
$$

The solution of the linear system can be achieved by various methods. Iterative methods are applied in this work. Floquet multipliuers are evaluated as the eigenvalues of the matrix $\mathbf{\Gamma}_1\mathbf{\Gamma}_2\cdots\mathbf{\Gamma}_N$ when the iterative solution of the $n \times N$ system is achieved (right hand side less than a maximum). Calculating the Floquet multipluiers in this way severely reduces the evaluation time compared to other methods (e.g. shooting method). The normal form coefficcient is calculated with different methods for the different type of bifurcation occuring. For more detailed information, the reader may refer to [60]

Bibliography

[1] A. Stodola. *Dampf- und Gasturbinen. Mit einem Anhang über die Aussichten der Wärmekraftmaschinen*. Springer-Verlag, 1924 (cit. on p. 1).

[2] Charles A. Parsons. *The Steam Turbine*. Cambridge University Press, 1911 (cit. on p. 1).

[3] US EIA. "Electricity Net Generation". In: (Mar. 2015) (cit. on p. 1).

[4] Precedence Research. "Steam Turbine Market (By Design: Reaction and Impulse; By Exhaust: Condensing and Non-condensing; By Fuel: Fossil Fuel, Biomass, and Geothermal; By End Use: Industrial and Utility; By Technology: Steam Cycle, Combined Cycle, and Cogeneration) - Global Industry Analysis, Size, Share, Growth, Trends, Regional Outlook, and Forecast 2021 2030". In: (Jan. 2022) (cit. on p. 1).

[5] T. Kellner. "Full Steam Ahead: Egypt Picks Worlds Largest Steam Turbines From GE For Its New Nuclear Power Plant". In: (Oct. 2018) (cit. on p. 1).

[6] Qi Luo, Kartik Ariyur, and Anoop Mathur. "Control-Oriented Concentrated Solar Power Plant Model". In: *IEEE Transactions on Control Systems Technology* 24 (June 2015), pp. 1–1. DOI: 10.1109/TCST.2015.2436975 (cit. on pp. 2, 4).

[7] *Special Purpose Steam Turbines For Petroleum, Chemical and Gas Industry Services*. Standard. American Petroleum Institute, June 1995 (cit. on p. 5).

[8] E. Krämer. *Dynamics of Rotors and Foundations*. Springer Berlin Heidelberg, 2013. ISBN: 9783662027981 (cit. on pp. 7, 51).

[9] Y. Hori. *Hydrodynamic Lubrication*. Springer-Verlag, 2006 (cit. on pp. 7, 13, 48).

[10] Tadashi Tanuma. *Advances in Steam Turbines for Modern Power Plants*. Woodhead Publishing seris in Energy, 2017 (cit. on pp. 7, 9).

[11] A. Tondl. *Some Problems of Rotor Dynamics*. Czechoslovak Academy of Sciences, Prague, 1965 (cit. on p. 12).

[12] F.F. Ehrich. *Subharmonic Vibration of Rotors in Bearing Clearance*. American Society of Mechanical Engineers. ASME, 1966 (cit. on p. 12).

[13] F. F. Ehrich. "High Order Subharmonic Response of High Speed Rotors in Bearing Clearance". In: *Journal of Vibration, Acoustics, Stress, and Reliability in Design* 110.1 (Jan. 1988), pp. 9–16 (cit. on p. 12).

[14] F.F. Ehrich. "Some Observations of Chaotic Vibration Phenomena in High-Speed Rotordynamics". In: *Journal of Vibration and Acoustics* 113 (1991), pp. 50–57 (cit. on pp. 12, 13).

[15] R. DiPrima. "A Note on the Stability of Flow in Loaded Journal Bearings". In: *ASLE Transactions* 6 (1963), pp. 249–253 (cit. on p. 12).

[16] C. Mayers. "Bifurcation Theory Applied to Oil Whirl in Plain Cylindrical Journal Bearings". In: *Journal of Applied Mechanics* 51 (1984), pp. 244–250 (cit. on p. 12).

[17] P. Hollis and D. Taylor. "Hopf Bifurcation to Limit Cycles in Fluid Film Bearings". In: *Journal of Tribology* 108 (1986), pp. 184–189 (cit. on p. 12).

[18] A. Muszynska. "Stability of whirl and whip in rotor/bearing systems". In: *Journal of Sound and Vibration* 127.1 (1988), pp. 49–64 (cit. on p. 12).

[19] M. T. M. Crooijmans, H. J. H. Brouwers, and A. de Kraker D. H. van Campen. "Limit cycle predictions of a nonlinear journal-bearing system". In: *Journal of Engineering for Industry* 112.2 (1990), pp. 168–185 (cit. on p. 12).

[20] F. F. Ehrich. "Observations of Subcritical Superharmonic and Chaotic Response in Rotordynamics". In: *ASME Journal of Vibration and Acoustics* 114.1 (1992), pp. 93–100 (cit. on p. 12).

[21] S. Noah and P. Sundararajan. "Significance of Considering Nonlinear Effects in Predicting the Dynamic Behavior of Rotating Machinery". In: *Journal of Vibration and Control* 1 (1995), pp. 431–458 (cit. on p. 12).

[22] C. S. Chen, S. Natsiavas, and H.D. Nelson. "Stability Analysis and Complex Dynamics of a Gear-Pair System Supported by a squeeze Film Damper". In: *ASME Journal of Vibration and Acoustics* 119 (1997), pp. 85–88 (cit. on p. 12).

[23] S. Theodossiades and S. Natsiavas. "Stability Analysis and Complex Dynamics of a Gear-Pair System Supported by a squeeze Film Damper". In: *ASME Journal of Sound and Vibration* 243.4 (2001), pp. 721–745 (cit. on p. 12).

[24] J. Wang and M. Khonsari. "Bifurcation Analysis of a Flexible Rotor Supported by Two Fluid-Film Journal Bearings". In: *Journal of Tribology* 128 (2006), pp. 594–603 (cit. on p. 12).

[25] J. Wang and M. Khonsari. "Prediction of Stability Envelope of Rotor-Bearing Systems". In: *Journal of Vibration and Acoustics* 128 (2006), pp. 197–202 (cit. on p. 12).

[26] M. Miraskari, F. Hemmati, and M. Gadala. "Nonlinear Dynamics of Flexible Rotors Supported on Journal Bearings - Part II: Numerical Bearing Model". In: *Journal of Tribology* 140 (2018), p. 021705 (cit. on p. 12).

[27] T. Shoyama. "Nonlinear Vibration of Saturated Water Journal Bearing and Bifurcation Analysis". In: *Journal of Vibration and Acoustics* 141.2 (2019), p. 021016 (cit. on p. 12).

[28] A. Chasalevris. "Stability and Hopf bifurcations in rotor- bearing-foundation systems of turbines and generators". In: *Tribology International* 145 (2020), p. 106154 (cit. on pp. 12, 24, 29).

[29] Z. Runeng et al. "Nonlinear dynamic analysis of supercritical and subcritical Hopf bifurcations in gas foil bearing-rotor systems". In: *Nonlinear Dynamics* 103 (2021), pp. 2241–2256 (cit. on p. 12).

[30] A. H. Nayfeh and D. Mook. *Nonlinear Oscillations*. John Wiley & Sons, 1979 (cit. on pp. 12, 38).

[31] L. Anastasopoulos and A. Chasalevris. "Bifurcations of limit cycles in rotating shafts mounted on partial arc and lemon bore journal bearings in elastic pedestals". In: *ASME Journal of Computational and Nonlinear Dynamics* (2021). Accepted (cit. on pp. 12, 14, 16).

[32] M. Khonsari and E.Booser. *Applied Tribology: Bearing Design and Lubrication, 3rd Edition*. Wiley online Library, 2010 (cit. on p. 13).

[33] D. Childs. *Turbomachinery Rotordynamics - Phenomena, Modeling, and Analysis*. John Wiley & Sons, 1993 (cit. on p. 13).

[34] K. Georg E. L. Allgower. *Introduction to Numerical Continuation Methods*. Society for Industrial and Applied Mathematics, 2003 (cit. on pp. 13, 14).

[35] H. Meijer, F. Dercole, and B. Olderman. *Numerical bifurcation analysis*. Encyclopedia of Complexity and Systems Science, R. A. Meyers Ed. Springer New Yorks, pp. 6329–6352 (cit. on p. 13).

[36] Y. A. Kuznetsov. *Elements of applied bifurcation theory 2nd ed.* Applied mathematical sciences. Springer New York, 1998 (cit. on p. 13).

[37] A. H. Nayfeh and B. Balachandran. *Applied nonlinear dynamics*. Wiley series in nonlinear science. J. Wiley & Sons, 1995 (cit. on pp. 13, 14).

[38] E. J. Doedel, H.B. Keller, and J.P. Kernevez. "Nonlinear dynamic analysis of supercritical and subcritical Hopf bifurcations in gas foil bearing-rotor systems". In: *International Journal of Bifurcation and Chaos* 1.3 (1991), pp. 745–772 (cit. on pp. 14, 30).

[39] E. J. Doedel. "Lecture Notes on Numerical Analysis of Nonlinear Equations". In: *Department of Computer Science, Concordia University, Montreal, Canada* () (cit. on pp. 14, 43).

[40] A. Boyaci et al. "Analytical bifurcation analysis of a rotor supported by floating ring bearings". In: *Nonlinear Dynamics* 57 (2009), pp. 497–507 (cit. on pp. 14, 15).

[41] A. Boyaci, D. Lu, and B. Schweizer. "Stability and bifurcation phenomena of Laval/Jeffcott rotors in semi-floating ring bearings". In: *Nonlinear Dynamics* 79 (2015), pp. 1535–1561 (cit. on pp. 14, 15).

[42] F. C. van Breemen. *Stability analysis of a laval rotor on hydrodynamic bearings by numerical continuation: Investigating the influence of rotor flexibility, rotor damping and external oil pressure on the rotordynamic behaviour*. M.Sc. Thesis. Delft University of Technology, 2016 (cit. on pp. 14, 16).

[43] J. Rubel. "Vibrations in nonlinear rotordynamics". PhD thesis. Ruprecht-Karls-Universität Heidelberg, 2009 (cit. on pp. 14, 15).

[44] A. Amamou and M. Chouchane. "Bifurcation of limit cycles in fluid film bearings". In: *International Journal of Non-Linear Mechanics* 46 (2011), pp. 1258–1264 (cit. on pp. 14, 15).

[45] R. Sghir and M. Chouchane. "Prediction of the nonlinear hysteresis loop for fluid-film bearings by numerical continuation". In: *Proc. IMechE Part C: J Mechanical Engineering Science* 229.4 (2015), pp. 651–662 (cit. on pp. 14, 15).

[46] R. Sghir and M. Chouchane. "Nonlinear stability analysis of a flexible rotor-bearing system by numerical continuation". In: *Journal of Vibration and Control* 22.13 (2016), pp. 3079–3089 (cit. on pp. 14, 15).

[47] K. Becker. "Dynamisches Verhalten hydrodynamisch gelagerter Rotoren unter berücksichtigung veranderlicher Lagergeometrienm". PhD thesis. Karlsruhe Institute of Technology, Germany, 2019 (cit. on pp. 14, 16).

[48] T. Leister. "Dynamics of Rotors on Refrigerant Lubricated Gas Foil Bearings". PhD thesis. Karlsruhe Institute of Technology, Germany, 2021 (cit. on pp. 14, 16).

[49] S. Kim and A. Palazzolo. "Bifurcation Analysis of a Rotor Supported by Five-Pad Tilting Pad Journal Bearings Using Numerical Continuation". In: *International Journal of Non-Linear Mechanics* 95 (2017), pp. 30–41 (cit. on pp. 14, 16).

[50] S. Kim and A. Palazzolo. "Shooting with Deflation Algorithm- Based Nonlinear Response and Neimark-Sacker Bifurcation and Chaos in Floating Ring Bearing Systems". In: *ASME Journal of Computational and Nonlinear Dynamics* 12 (2017), p. 031003 (cit. on pp. 14, 16).

[51] S. Kim and A. Palazzolo. "Shooting/continuation based bifurcation analysis of large order nonlinear rotordynamic systems". In: *ATEC Web of Conferences VETOMAC XIV* 211 (2018), p. 18003 (cit. on pp. 14, 16).

[52] Y. Ishida and T. Yamamoto. *Linear and Nonlinear Rotordynamics: A Modern Treatment with Applications, Second Edition*. Wiley-VCH Verlag GmbH & Co. KGaA, 2012 (cit. on p. 17).

[53] J. M. McVaugh H. D. Nelson. "The Dynamics of Rotor-Bearing Systems Using Finite Elements." In: *ASME Journal of Engineering for Industry* 98 (1976), pp. 593–600 (cit. on p. 17).

[54] J. Guyan. "Reduction of stiffness and mass matrices". In: *AIAA Journal* 3 (1965), p. 380 (cit. on p. 23).

[55] V. N. Constantinescu. "On Turbulent Lubrication". In: *Proceedings of the Institution of Mechanical Engineers* 173.1 (1959), pp. 881–900 (cit. on pp. 25, 26).

[56] H. Elrod. "A Cavitation Algorithm". In: *Journal of Lubrication Technology* 103.3 (1981), pp. 350–354 (cit. on p. 28).

[57] B. Jakobson and L. Floberg. "The finite journal bearing considering vaporization". In: *Transactions of Chalmers University Technology, Goteborg, Sweden* 190.190 (1957), pp. 1–119 (cit. on p. 28).

[58] W. Stieber. *Das Schwimmlager: Hydrodynamische Theorie des Gleitlagers*. V.D.I. Verlag GMBH, Berlin 106, 1933 (cit. on p. 28).

[59] L. Gümbel. *Das Problem der Lagerreibung*. Mon. Berl. Bezirksverein.,V.D.I., 5, 1914, 87104 and 109–120 (cit. on p. 28).

[60] Y. A. Kuznetsov et al. "Numerical periodic normalization for codim 1 bifurcations of limit cycles". In: *SIAM Journal on Numerical Analysis* 43.4 (2005), pp. 1407–1435 (cit. on p. 60).